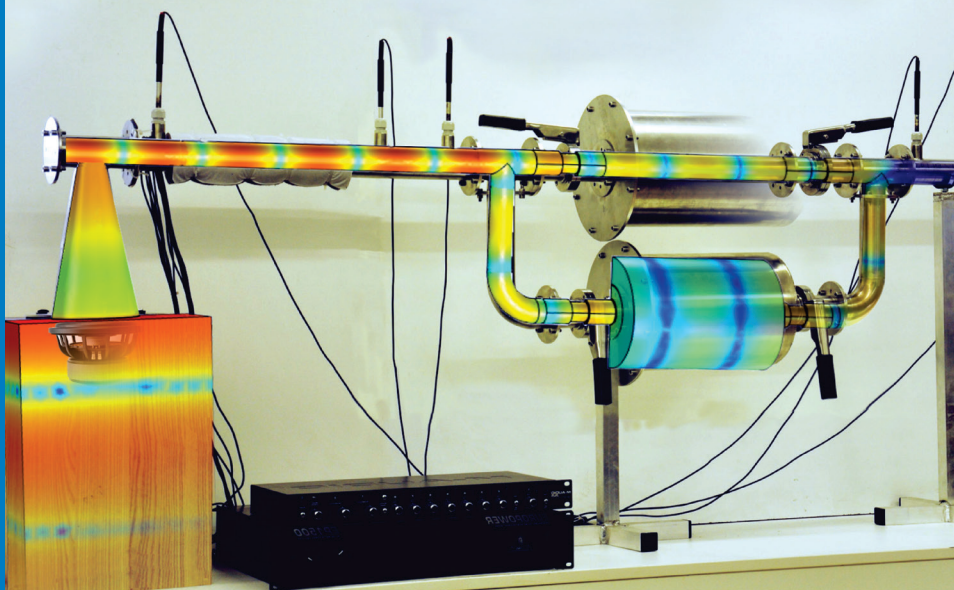
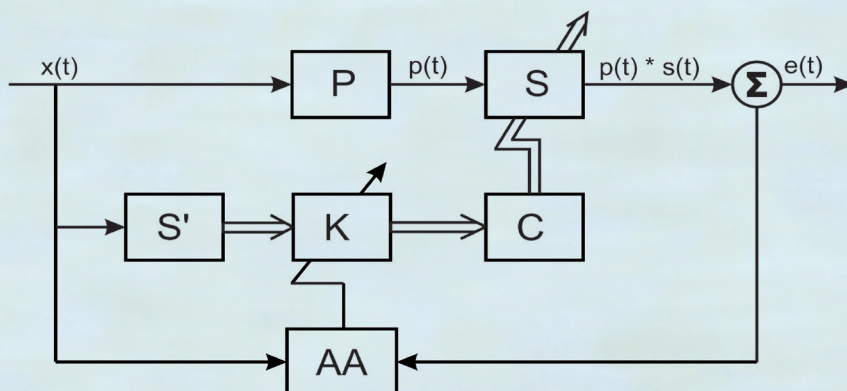




# Strojniški vestnik

## Journal of Mechanical Engineering



no. **10**  
year **2015**  
volume **61**

## Aim and Scope

The international journal publishes original and (mini)review articles covering the concepts of materials science, mechanics, kinematics, thermodynamics, energy and environment, mechatronics and robotics, fluid mechanics, tribology, cybernetics, industrial engineering and structural analysis.

The journal follows new trends and progress proven practice in the mechanical engineering and also in the closely related sciences as are electrical, civil and process engineering, medicine, microbiology, ecology, agriculture, transport systems, aviation, and others, thus creating a unique forum for interdisciplinary or multidisciplinary dialogue.

The international conferences selected papers are welcome for publishing as a special issue of SV-JME with invited co-editor(s).

## Editor in Chief

Vincenc Butala

University of Ljubljana, Faculty of Mechanical Engineering, Slovenia

## Technical Editor

Pika Škraba

University of Ljubljana, Faculty of Mechanical Engineering, Slovenia

## Founding Editor

Bojan Kraut

University of Ljubljana, Faculty of Mechanical Engineering, Slovenia

## Editorial Office

University of Ljubljana, Faculty of Mechanical Engineering

SV-JME, Aškerčeva 6, SI-1000 Ljubljana, Slovenia

Phone: 386 (0)1 4771 137

Fax: 386 (0)1 2518 567

info@sv-jme.eu, <http://www.sv-jme.eu>

**Print:** Grafex, d.o.o., printed in 380 copies

## Founders and Publishers

University of Ljubljana, Faculty of Mechanical Engineering, Slovenia

University of Maribor, Faculty of Mechanical Engineering, Slovenia

Association of Mechanical Engineers of Slovenia

Chamber of Commerce and Industry of Slovenia,

Metal Processing Industry Association

## President of Publishing Council

Branko Širok

University of Ljubljana, Faculty of Mechanical Engineering, Slovenia

## Vice-President of Publishing Council

Jože Balič

University of Maribor, Faculty of Mechanical Engineering, Slovenia



### Cover:

Experimental setup for validation of numerical simulation is presented. Experimental setup was designed for testing a new approach in adaptive control of reactive silencers. Instead of controlling one single propertie of reactive silencer, this approach controls the physical operational principle of reactive silencers. The new approach enables faster adaptation and consequently higher transmission losses. System was developed in the laboratory for machinery and technical acoustics (LDSTA) at Faculty of Mechanical Engineering.

Courtesy: LDSTA, Faculty of Mechanical Engineering, University of Ljubljana.

## International Editorial Board

Kamil Arslan, Karabuk University, Turkey

Josep M. Bergada, Politechnical University of Catalonia, Spain

Anton Bergant, Litostroj Power, Slovenia

Miha Boltežar, UL, Faculty of Mechanical Engineering, Slovenia

Franci Čuš, UM, Faculty of Mechanical Engineering, Slovenia

Anselmo Eduardo Diniz, State University of Campinas, Brazil

Igor Emri, UL, Faculty of Mechanical Engineering, Slovenia

Imre Felde, Obuda University, Faculty of Informatics, Hungary

Janez Grum, UL, Faculty of Mechanical Engineering, Slovenia

Imre Horvath, Delft University of Technology, The Netherlands

Aleš Hribernik, UM, Faculty of Mechanical Engineering, Slovenia

Soichi Ibaraki, Kyoto University, Department of Micro Eng., Japan

Julius Kaplunov, Brunel University, West London, UK

Iyas Khader, Fraunhofer Institute for Mechanics of Materials, Germany

Jernej Klemenc, UL, Faculty of Mechanical Engineering, Slovenia

Milan Kljajin, J.J. Strossmayer University of Osijek, Croatia

Janez Kušar, UL, Faculty of Mechanical Engineering, Slovenia

Gorazd Lojen, UM, Faculty of Mechanical Engineering, Slovenia

Thomas Lübben, University of Bremen, Germany

Janez Možina, UL, Faculty of Mechanical Engineering, Slovenia

George K. Nikas, KADMOS Engineering, UK

José L. Ocaña, Technical University of Madrid, Spain

Miroslav Plančak, University of Novi Sad, Serbia

Vladimir Popović, University of Belgrade, Faculty of Mech. Eng., Serbia

Franci Pušavec, UL, Faculty of Mechanical Engineering, Slovenia

Bernd Sauer, University of Kaiserlautern, Germany

Rudolph J. Scavuzzo, University of Akron, USA

Arkady Voloshin, Lehigh University, Bethlehem, USA

## General information

Strojniški vestnik – Journal of Mechanical Engineering is published in 11 issues per year (July and August is a double issue).

Institutional prices include print & online access: institutional subscription price and foreign subscription €100,00 (the price of a single issue is €10,00); general public subscription and student subscription €50,00 (the price of a single issue is €5,00). Prices are exclusive of tax. Delivery is included in the price. The recipient is responsible for paying any import duties or taxes. Legal title passes to the customer on dispatch by our distributor.

Single issues from current and recent volumes are available at the current single-issue price. To order the journal, please complete the form on our website. For submissions, subscriptions and all other information please visit: <http://en.sv-jme.eu/>.

You can advertise on the inner and outer side of the back cover of the journal. The authors of the published papers are invited to send photos or pictures with short explanation for cover content.

We would like to thank the reviewers who have taken part in the peer-review process.

The journal is subsidized by Slovenian Research Agency.

Strojniški vestnik - Journal of Mechanical Engineering is available on <http://www.sv-jme.eu>, where you access also to papers' supplements, such as simulations, etc.

ISSN 0039-2480

© 2015 Strojniški vestnik - Journal of Mechanical Engineering. All rights reserved. SV-JME is indexed / abstracted in: SCI-Expanded, Compendex, Inspec, ProQuest-CSA, SCOPUS, TEMA. The list of the remaining bases, in which SV-JME is indexed, is available on the website.

# Contents

**Strojniški vestnik - Journal of Mechanical Engineering**  
**volume 61, (2015), number 10**  
**Ljubljana, October 2015**  
**ISSN 0039-2480**

**Published monthly**

## **Papers**

Peter Šteblaj, Mirko Čudina, Primož Lipar, Jurij Prezelj: A Muffler with Adaptive Acoustic Properties	553
Om Prakash Singh, Rohit Raut, Mrinmoy Biswas, Ramji Singh: Effect of Dynamic Vents on the Thermal Comfort of a Passenger Car	561
Livia Dana Beju, Paul Dan Brindasu, Silvia Vulc: Grinding Tungsten Carbide Used for Manufacturing Gun Drills	571
Paolo Casoli, Nicola Pompini, Luca Riccò: Simulation of an Excavator Hydraulic System Using Nonlinear Mathematical Models	583
Mohammadreza Saffarian, Moona Mohammadi, Mohammadreza Mohammadi: Non-Newtonian Shear-Thinning Fluid Passing Through a Duct with an Obstacle, Using a Power Law Model	594
Iskender Ozsoy, Askin Demirkol, Abdullah Mimaroglu, Huseyin Unal, Zafer Demir: The Influence of Micro- and Nano-Filler Content on the Mechanical Properties of Epoxy Composites	601
Sedat Bingöl, Wojciech Misiolek: Prediction of the True Stress of ZE20 Magnesium Alloy at Different Temperatures and Strain Rates	610



# A Muffler with Adaptive Acoustic Properties

Peter Šteblaj\* – Mirko Čudina – Primož Lipar – Jurij Prezelj  
University of Ljubljana, Faculty of Mechanical Engineering, Slovenia

*An adaptive muffler upgrades the conventional muffler with a variable geometry to extend its working range. Adaptive muffler systems, described in the available literature, operate on the principle of controlling only a single property of the muffler to tune its working range. During the adaptation process of these systems, the basic principle of operation is not changed. Based on the literature review, the question arises of whether it would be possible to control the principle of operation. At one instant it would work as a Helmholtz resonator, in the other as an expansion chamber or side branch resonator. Analytical calculations provided a positive answer, and a muffler with four active valves was designed and constructed to confirm the theoretical expectations. The properties of proposed muffler were simulated with the Finite Element Method, and the results of simulations were validated with measurements. Finally, simulations of the proposed muffler were performed, working at different operating condition. Simulations have shown that the proposed system allows the tuning of the muffler to a wide working frequency range. Such an approach to muffler design eliminates the need for additional mufflers in IC exhaust systems. Therefore, a smaller volume of the proposed muffler enables the same effect as multiple non-adaptive conventional mufflers.*

**Keywords:** adaptive muffler, hybrid muffler, noise control, exhaust system

## Highlights

- The proposed adaptive muffler can be adjusted to specific noise by changing its operating principle, instead of only changing one of its properties.
- The active algorithm sets discrete values of valves instead of generating a signal for the actuator.
- The adaptation speed of the algorithm is very fast.
- The adaptive muffler can be smaller in comparison to conventional mufflers.

## 0 INTRODUCTION

Engine exhaust is one of the dominant noise sources of vehicles. Different exhaust systems with mufflers are being developed to reduce this noise, in order to meet the required noise levels and sound quality. Their design is simultaneously optimized to minimize the pressure drop in the exhaust system. Muffler design is usually based on the theory of four reactive resonators; the Helmholtz resonator, the expansion chamber, the side branch resonator, and the Herschel-Quincke tube [1] and [2].

The optimization of the conventional reactive muffler with a fixed geometry for acoustic performance and low production costs is a complex task, [3] and [4], the result of which is usually a complicated internal geometrical structure, which increases backpressure. A muffler in the exhaust system of an internal combustion (IC) engine reduces its power and increases fuel consumption [1] and [5]. The engine power loss due to such a conventional passive exhaust muffler system is known to be at least 10% [1] and [6]. Dual mode mufflers [7] and reactive mufflers with various internal configurations [5] have been proposed to reduce the problems caused by the high backpressure of conventional mufflers, but with only limited success. To overcome this problem, active noise control (ANC) systems were

developed. They are an up-to-date alternative for classical reactive resonators. ANC is a method for reducing unwanted noise with its “antinoise”, which is specifically calculated and generated to be a copy of unwanted noise with a reversed phase. ANC can be applied in various situations for suppressing unwanted noise [8], and is widely used in cabins [9] and [10], in ducts [11] and [12] and also in engine exhaust systems [13] and [14]. The ANC method applied to vehicle exhaust noise reduction has some advantages, such as no increase in the exhaust backpressure, improving the performance of the engine, and reducing fuel consumption. Furthermore, it may make the structure of the active muffler compact and facilitate its installation [13]. Such mufflers have been continually improved in recent years. Mufflers with ANC use specially designed loudspeakers to generate “antinoise” to cancel the exhaust noise. Such loudspeakers have to reproduce noise and withstand high temperatures and pressure pulsations. Despite positive results in the laboratory and in actual car-installation, this method has thus far failed to be widely commercialized for applications in exhaust systems.

In recent years, a great deal of effort has been put into the research of adaptive reactive mufflers [6], [11], [15] and [16]. Instead of loudspeakers, adaptive mufflers use non-acoustic actuators to eliminate the

\*Corr. Author's Address: University of Ljubljana, Faculty of Mechanical Engineering, Aškerčeva 6, 1000 Ljubljana, Slovenia, peter.steblaj@fs.uni-lj.si

problems of acoustic feedback, which is one of the prevailing problems in the practical usage of ANC. The main advantage of the adaptive muffler is its ability to control its effects in real time and consequently achieve higher noise reduction for different input noises. Its efficiency in noise reduction can be tuned to desired levels and/or to the welfare of the users' subjective expectations. Different algorithms for adaptive tuning of mufflers by controlling different physical properties are constantly being developed.

In previous literature, Bartlett and Whalley [17] developed the mathematical background for the variable geometry of exhaust systems. Chiu and Chang [4] proposed shape optimization of the muffler within limited space using a simulated annealing (SA) method. Chiu [3] also used the SA method to optimize broadband noise with multiple tones. Hwang et al. [6] proposed a method using actively controlled U-shape bypass pipes. Cherrier et al. [18] created perforated panel resonators with an active control of their openings (so-called necks). Chen and Too [11] combined the principle of the reactive muffler with an actively controlled loudspeaker. Kostek and Franchek [19] proposed a hybrid resonator with an actively controlled cavity of the Helmholtz resonator. Howard and Craig [15] and [20] presented an adaptive quarter-wave resonator to attenuate the exhaust noise of a V6 petrol engine, adapting to changes in engine operating conditions (revolutions per minute (RPM) and load), and exhaust gas temperature.

In the available literature on adaptive mufflers, the main acoustic path is always manipulated in order to increase transmission loss (TL) at different operating conditions. Such systems are able to adapt to the current operating condition and their noise attenuation is increased in the overall frequency range.

In this article, a new idea of adapting the mufflers' acoustic properties is presented. Adaptation is achieved with the redirection of the stream flow by using the actively controlled valves. The idea is to use the valves to change the principle of the noise attenuation mechanism in real time. The system attenuates the sound propagation by using the Helmholtz resonator at one moment; at the next moment, the system can switch to work as an expansion chamber or quarter wavelength resonator. With such an approach, noise reduction can be tuned to various operating conditions without an increase of backpressure or reduction in engine performance. The proposed adaptive muffler with active flow valves (V1-4) is presented in Fig. 1. The configuration in Fig. 1 was used to include four basic theoretical principles of reactive mufflers: Helmholtz resonator, expansion

chamber, side-branch resonator ( $\lambda/4$ ), and Herschel-Quincke tube. Geometry, positions and the number of valves can be optimized according to the demands of the working environment. Control of the reactive noise attenuation principle within one dynamic system is an optimization problem similar to the current approach [3] and [4].

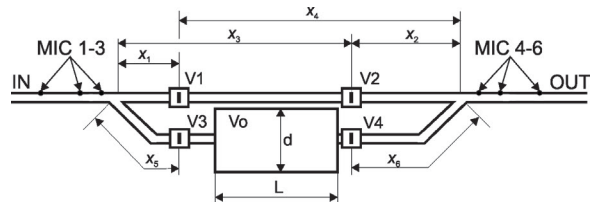


Fig. 1. Proposed adaptive muffler with active flow valves

The confirmation of the hypothesis presented in this paper was confirmed with four individual approaches: 1) analytical calculation, 2) experiment, 3) numerical simulations of steady state operation using the finite element method (FEM), and 4) numerical simulation of transient effects. All four individual approaches provide encouraging results for the implementation of the proposed system into production.

## 1 ANALYTICAL CALCULATION

Reactive mufflers are designed to reduce plane sound wave propagation. Their design is based either on the principle of the Helmholtz resonator, the expansion chamber, the quarter wavelength resonator or, in special cases, the Herschel-Quincke tube. In general, the Helmholtz resonator (HR) is suitable for attenuating the lowest discrete frequencies with high amplitudes [21]. Some designs of HR are composed of several resonators of different sizes to target a broader range of frequencies. Expansion chamber mufflers have an effect in broadband frequency range and have no effect when the product of  $kL$  is equal  $\pi$ ,  $2\pi$ ,  $3\pi$ , etc. Davis et al. [22] reported that their performance can deteriorate at higher frequencies when the cross-section dimension of the muffler reaches 82 % of the acoustic wavelength.

Quarter wavelength resonators are effective in attenuating a discrete noise and its higher odd-harmonics. Herschel-Quincke tubes are also suitable for discrete noise and its higher harmonics [16]. However, these types of non-adaptive resonators have limited application for noise sources with variable discrete frequencies.

The proposed system (Fig. 1) consists of an inlet pipe, three microphones (MIC 1 to 3) for measuring the incident and reflected sound wave propagation at the input, four valves (V1 to V4) for redirecting the main stream flow, an expansion chamber with interconnecting pipes, an outlet pipe, and three microphones (MIC 4 to 6) for measuring the transmitted sound waves at the output.

Sound propagates downstream to the first Y-junction, where it splits into two separate ways. One way is directly downstream, and the other is through the expansion chamber.  $x_1, \dots, x_6$  are the dimensions of individual reactive elements. The dimensionless ratios  $x_1/x_5$ ,  $x_1/x_2$ ,  $x_2/x_5$ , etc. are extremely important. They determine the attenuation of discrete frequencies. The optimization of this ratio depends on noise sources.

To predict the performance of a muffler, the transfer matrix method was used [23]. This method is recommended by various authors [2] to [4], [21], [24] and [25]. The sound pressure and the normal particle velocities upstream and downstream of the muffler can be expressed as a transfer matrix with Eq. (1):

$$\begin{bmatrix} P_u \\ U_u \end{bmatrix} = \begin{bmatrix} T_{11} & T_{12} \\ T_{21} & T_{22} \end{bmatrix} \begin{bmatrix} P_d \\ U_d \end{bmatrix}, \quad (1)$$

where  $P_u$  and  $U_u$  represent the sound pressure and particle velocity in the upstream direction, and  $P_d$  and  $U_d$  represents the sound pressure and velocity in the downstream direction. Matrix  $\mathbf{T}$  is a transfer matrix that is defined by the geometry and dimensions of the muffler.  $TL$  is defined as the difference between the incident power on the muffler and the transmitted power into the downstream direction of the anechoic termination. The  $TL$  of the expansion chamber can be expressed with Eq. (2)

$$TL = 10 \times \log \left( 1 + \frac{1}{4} \left( \frac{S_1}{S_2} - \frac{S_2}{S_1} \right)^2 \sin^2 kL \right), \quad (2)$$

where  $S_1$  and  $S_2$  are the cross-section of the duct before the expansion and cross-section after the expansion, respectively,  $L$  is the length of the expansion chamber and  $k$  is the wave number.  $TL$  for the Helmholtz resonator can be written as:

$$TL = 10 \times \log \left( 1 + \frac{c^2}{4S^2 \left( \frac{\omega L'}{S} - \frac{c^2}{\omega V} \right)^2} \right), \quad (3)$$

where  $\omega$ ,  $c$ ,  $V$ ,  $S$ ,  $L'$  are the resonance frequency, the speed of sound, the volume of the cavity, the cross

section of the neck, and the effective length of the resonator, respectively. The  $TL$  of a quarter-wave resonator is:

$$TL = 10 \times \log \left( \frac{\left( \frac{R_s}{\rho_0 c} + \frac{\pi a^2}{2S} \right)^2 \tan^2(kL') + 1}{\left( \frac{R_s}{\rho_0 c} \right)^2 \tan^2(kL') + 1} \right), \quad (4)$$

where  $R_s$ ,  $S$ ,  $L'$ ,  $a$ ,  $\rho_0 c_0$  are the specific acoustic resistance, the cross section of the main duct, the effective length and radius of the resonator and the specific acoustic impedance, respectively.

The analytical results of  $TL$ , as a function of frequency, are presented in Fig. 2 for four different reactive mufflers (Expansion chamber - solid line, Helmholtz resonator - dotted line,  $\lambda_1/4$  resonator - dashed line, and  $\lambda_2/4$  - dash dotted line).

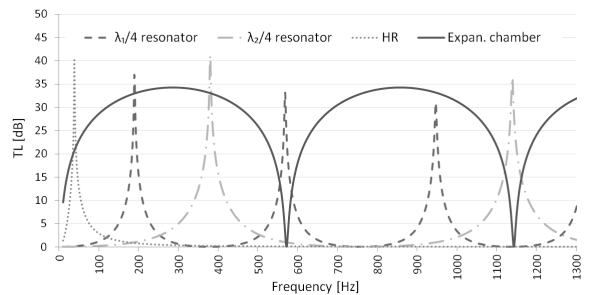


Fig. 2. Results of analytical calculations

The Helmholtz resonator is tuned to a selected frequency at which the system oscillates. More  $\lambda/4$  resonators are tuned to back up the performance of the expansion chamber at its  $TL$  minima.

## 2 EXPERIMENTAL SET-UP

The modular construction of the experimental set-up is presented in Fig. 3. It enables easy changing of the experimental configuration and measurements of different acoustical characteristics.

The dimensions of the muffler system are selected according to the demands of a typical IC exhaust system. The experimental setup was built from stainless steel pipes with a diameter of  $\phi 48$  mm. Its total length was 3400 mm, simulating an average vehicle exhaust system. For input noise simulation, a loudspeaker with a diameter of  $\phi 120$  mm was used. It was mounted in a 20 litre box. Pink noise was used as a test signal to excite the system and to measure  $TL$ ,

which was done in a frequency range from 10 Hz to 1200 Hz.

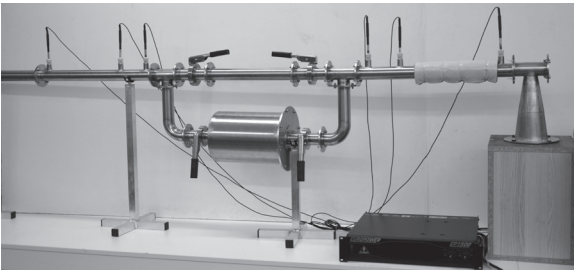


Fig. 3. Experimental set-up

Six microphones were used to measure the sound pressure field; three in the downstream direction and three upstream. Three microphones were used on each side of the muffler to overcome the inherent problems of measurements in the standing wave sound field.

### 3 SIMULATIONS WITH FEM

The boundary element method (BEM) and FEM are usually used to predict the performance of mufflers in frequency and in time domain analysis [26] and [27]. FEM analysis is better suited for our applications. It enables the evaluation of the validity of the results in the upper frequency range. It also enables the observation of the sound pressure standing waves, which are formed in duct systems.

When simulating a complex system, such as the one presented, there are many other influences on acoustic attenuation, such as the impedance of the wall, termination of the pipe, etc. Therefore, a validation of the FEM simulation was performed. FEM simulations were validated for the measurement set-up presented in Fig. 3. Validated FEM analyses were used to perform the frequency domain analysis, to determine the overall TL of the system, and to determine the transient effects of changing the position of the valves. Additional analysis was made to determine the influence of the valve position on overall transmission. The results of validation are presented in Fig. 4 for five different options of valve openings.

During the validation process of FEM simulations, it was shown that the frequency response of the noise source has to be taken into consideration. Therefore, a frequency response of the loudspeaker was included in the FEM model to obtain agreement between the measured and simulated results.

The validation process of FEM simulations also showed that a nonreflecting boundary condition, which

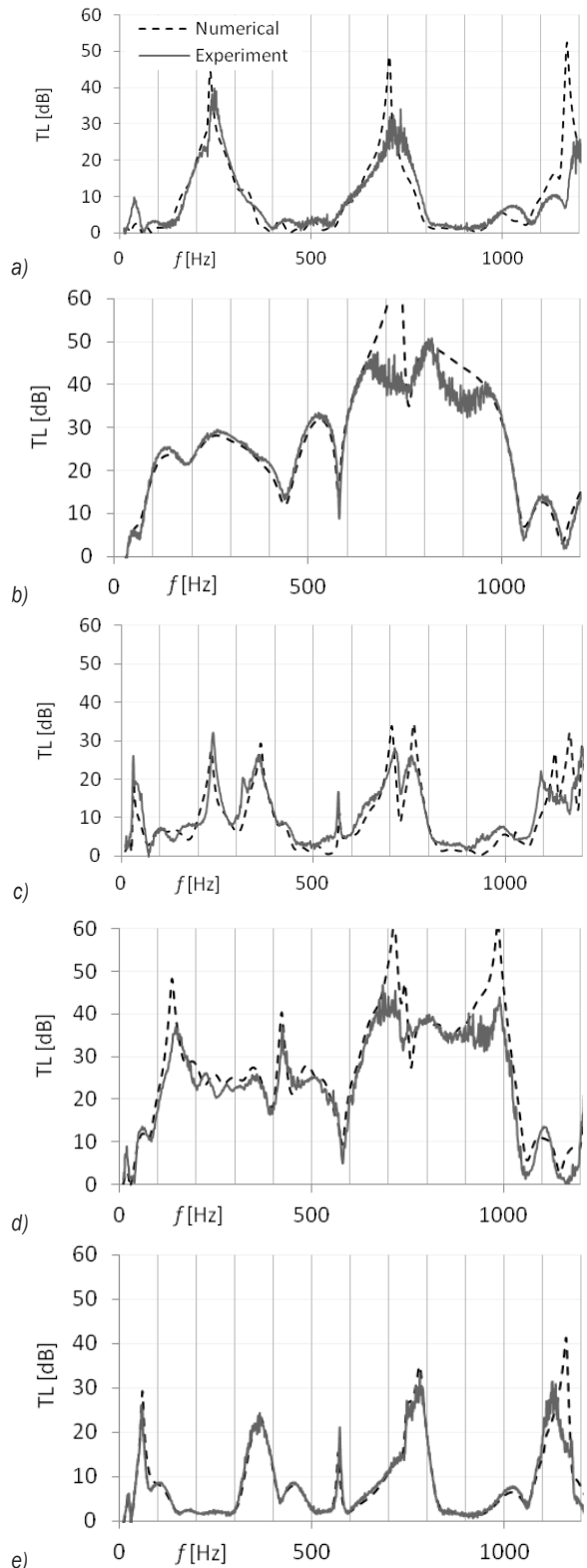


Fig. 4. Comparison between measured results and results of FEM analysis a) double  $\lambda/4$  resonator, b) expansion chamber, c) Helmholtz resonator with  $\lambda/4$  resonator, d) expansion chamber with  $\lambda/2$  resonator, e) all open valves

can be implemented as a perfectly matched layer [28], does not provide suitable results for the prediction of the internal acoustic field in the muffler. Therefore, in this study, anechoic termination was modeled using the sound absorption of porous material obtained with the Delany-Bazley model [29]. During the validation process of the FEM simulations, it was shown that the pipes used in the experimental set-up cannot be modeled with a rigid surface; therefore, an impedance boundary condition was used. The impedance of the pipes' surface was determined empirically. A very good agreement between results of the FEM analysis and measurement results on the experimental setup was thus achieved, as can be seen in Fig. 4.

The results of the analysis showed that opened valves have only a minor effect on the overall TL in the frequency range of interest. Their effect was neglected during the steady state calculations of the muffler TL.

Fig. 5 shows the maximum overall TL of our system. With the presented configuration, up to 50 dB of TL was achieved in the frequency range observed.

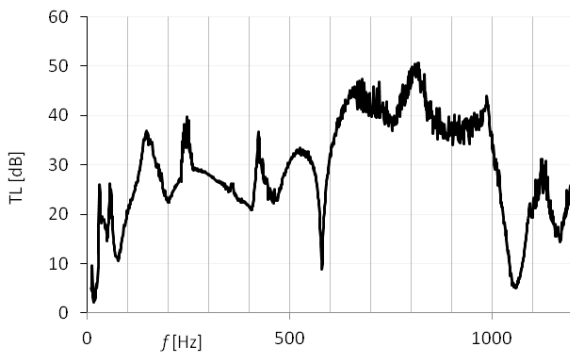


Fig. 5. Maximum overall expected TL based on measurement

#### 4 ADAPTIVE CONTROL OF MUFFLER

For adaptive control of the valves, the active noise control approach (ANC) was used (Fig. 6a). A reference signal  $x(t)$ , which can be obtained from a reference microphone (MIC 1), is used to describe the input sound pressure.

P and S in Fig. 6a represent the transfer function of the primary path, which consists of the acoustic response from the measuring microphones to the error microphone. The primary acoustic path is composed of the fixed part P and variable part S. S is the transfer function of the adaptive muffler. S' is a matrix of estimated TL for each valve configuration. C is the controller for controlling the states of 4 valves.  $e(t)$  is the error or the feedback of the effectiveness of TL detected by MIC 6. AA represents the adaptive

algorithm which is used to track and adapt coefficients to current conditions. It is used in the case of the system property changes due to temperature difference, flow changes, or some other effects that influence the TL of the muffler.

The input signal  $x(t)$  is obtained and processed on the secondary path. K represents the decision matrix in which the decision is made about which combination of valves is used (Fig. 6b). The spectrum is calculated from the input signal and compared to the known TL of each combination of valves. Utilizing the controller and its decision matrix, the system will choose which combination is the best to use. This decision matrix can be calculated using several decision criteria: the RMS of the spectrum, maximum sound pressure level, psychoacoustic criteria, or similar.

In this study, the muffler has five discrete options, depending on five combinations of the flow valves states. Its transmission losses are presented in Fig. 4.

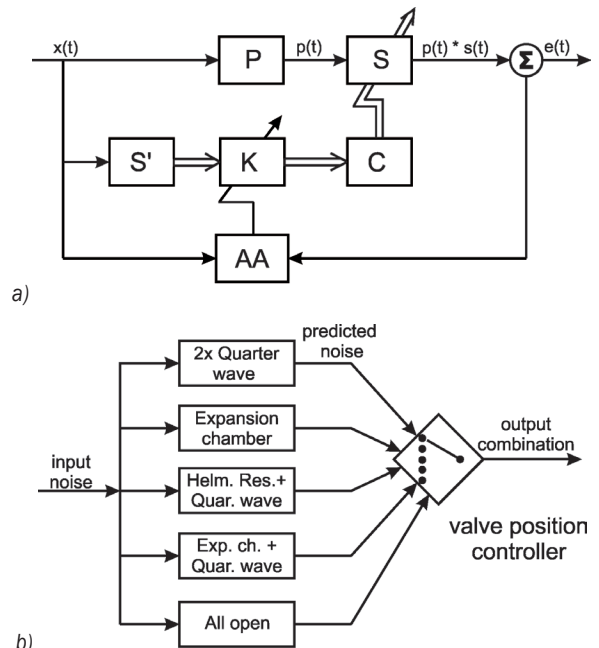


Fig. 6. Adaptive noise control principle: a) adaptive noise control algorithm, b) decision matrix

By adjusting four valves (V1 to V4) in the test setup, five different options of TL can be achieved (Fig. 1). The first option is for opened valves V1 and V3 and closed V2 and V4 (Fig. 4a). The second option is for closed valves V1 and V3 and for opened valves V2 and V4 (Fig. 4b). Stream propagation is altered through the expansion chamber, and results in the noise attenuation of the expansion chamber. An additional quarter-wave resonator can be used, whose length is determined by the position of V1 and V3.

The third option is for closed valves V4 and for all the other valves opened (Fig. 4c). The expansion chamber acts as a cavity and the bent part of the pipe acts as a neck for the Helmholtz resonator. The bent part of the pipe acts as a single quarter wavelength resonator. This option is suitable for the lowest frequencies, such as for the tonal noise and its odd harmonics. The fourth option is for the closed valve V1 and for all the other valves opened (Fig 4d). This combination adds a quarter-wavelength resonator ( $\lambda/4$ ) to the expansion chamber. The length of this quarter wavelength resonator can be altered by the positions of V1 and V3. The last, fifth, option is for all valves opened (Fig. 4e). In this case, the secondary path acts as a Herschel-Quincke tube with an additional expansion chamber in between.

## 5 RESULTS OF TRANSIENT ANALYSIS

Fig. 4 shows the TL of five different valve opening combinations. Valve combinations are selected using a decision matrix. The results of the decision matrix for the RMS of the spectrum are presented in Table 1. The RMS of each option is presented along with the decision matrix  $\mathbf{K}$  selections. In this criterion, the RMS of the input noise spectrum was calculated and compared with the known TL for each option in the selected frequency range. Lower RMS means a smaller difference between the known TL and input spectrum, which are equal to greater overall noise attenuation (written in bold). For the test signal, six different input noises were used.

**Table 1.** Results of decision matrix for discrete input signals

Freq [Hz]	Leq [dB]	Options					K [opt.]
		1 [dB]	2 [dB]	3 [dB]	4 [dB]	5 [dB]	
30	90	96.8	91.3	<b>75.8</b>	90.3	87.9	3
50	90	93.4	84.2	83.4	77.4	<b>73.6</b>	5
150	90	88.0	64.8	82.9	<b>56.7</b>	89.9	4
250	90	<b>57.4</b>	63.6	68.5	71.1	89.8	1
520	90	87.3	<b>58.9</b>	87.5	69.2	90.0	2
PN	90	83.2	<b>70.9</b>	82.3	74.3	81.8	2

Five of them were combined from pink noise with a pronounced discrete frequency tone. One signal contained only pink noise. All of the input noises had the same equivalent level of noise: 90 dB. The results of the RMS of spectra are shown in Table 1 (columns 3 to 7, options 1 to 5). The last column represents the outcome of the decision matrix selection. It is clear that the decision matrix result was always the lowest calculated RMS. For the final test signal, only pink noise was used and compared to the known TL.

To determine the optimal coefficients of the filter used for the specific frequency range, a band pass signal of pink noise with a bandwidth of 20 Hz and sound pressure level of 90 dB was swept through the frequency range of interest. The frequency range of interest was set from 10 Hz to 1200 Hz. Fig. 7 represents the frequency response of the system on the input test signal; Line 1 is input test signal (horizontal line); Line 2 is output SPL (solid line); Line 3 is maximum TL (dash dot line). The output SPL is inversely proportional to maximum TL if the control system is tracking changes in real time. Vertical dashed lines represent the limits of individual option settings for specific frequency ranges. The optimal decisions for used algorithm are presented in Table 2. The performance of the system was tested with slow and fast changes of the input signal. During slow changes, the system had enough time to calculate optimal solutions. During fast changes, a time delay resulted in frequency shifts.

**Table 2.** Optimal K for specific frequency range

$f_{min}$ [Hz]	$f_{max}$ [Hz]	$\Delta f$ [Hz]	$K_{optimal}$
10	30	20	3
30	60	30	5
60	85	25	2
85	190	105	4
190	198	8	2
198	250	52	1
250	378	128	2
378	450	72	4
450	680	230	2
680	685	5	4
685	945	260	2
945	1015	70	4
1015	1045	30	2
1045	1070	25	3
1070	1150	80	5
1150	1156	6	1
1156	1190	34	3
1190	1202	12	1

Fast changes of the input signal were defined by the velocity of the frequency sweep. The velocity of slow changes was defined as  $df/dt = 0$  Hz/s. Fast changes were defined as  $df/dt = 100$  Hz/s to 1000 Hz/s, which gives the system less time to calculate an optimal solution. The system response to fast changes is presented in Figs. 8 and 9. A system working under fast changes of input signals cannot follow the optimal working conditions fast enough. This can be seen as an increase of sound pressure level after each

change of option. The time delay of control system reduces system performance. The velocity of changes in practical systems does not exceed 300 Hz/s. This gives our system enough time to adapt to changes in a real system.

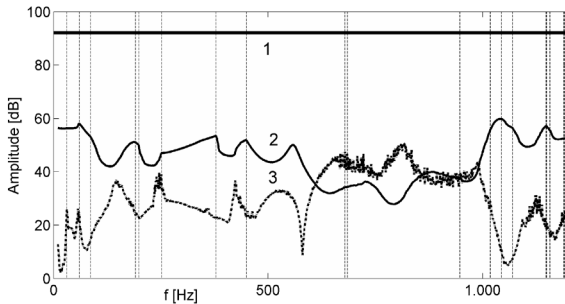


Fig. 7. Frequency response of proposed system on input signal

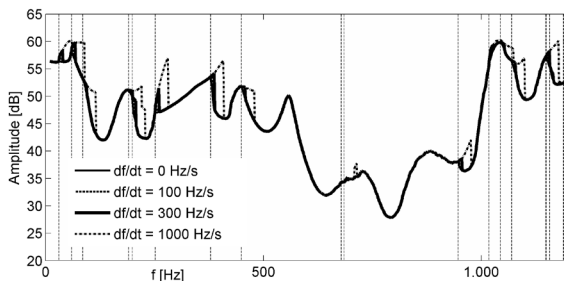


Fig. 8. Time delay of the control system is represented with frequency shift

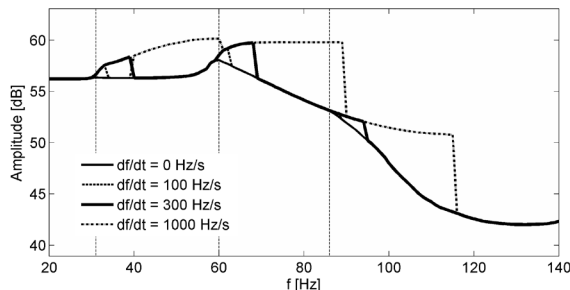


Fig. 9. Detailed time delay from Fig. 8 in frequency range 20 Hz to 140 Hz on performance delay of frequency shift

## 6 CONCLUSIONS

The idea presented in this article is to achieve an adaptive muffler system that is able to adapt to different operating conditions and noise perception. An adaptive muffler was designed to manipulate four different mechanisms of noise control. The dimensions of pipes, position and number of valves and their openings, and changes in the intersection of connecting elements can be optimized for the demands of noise control or for psychoacoustic criteria.

Combinations of multiple individual reactive mufflers can be used and controlled by a single actively controlled valve. The active noise control principle was implemented. The response of the proposed system was tested with different input signals. The performance of the system was also tested with slow and fast changes of the input signal to determine the overall stability. With the newly proposed approach, the multiple noise reduction principle can be used in one system. Therefore, a smaller volume of muffler enables the same effect as multiple non-adaptive reactive mufflers.

The principle of the actively controlled valve system can also be applied in the ducts of air conditioning systems or ventilation units where additional individual units are used for short periods of time or when operating conditions are changed.

## 7 REFERENCES

- [1] Munjal, M. (1987). *Acoustics of Ducts and Mufflers with Application to Exhaust and Ventilation System Design*. John Wiley & Sons, New York.
- [2] Yasuda, T., Wu, C., Nakagawa, N., Nagamura, K. (2013). Studies on an automobile muffler with the acoustic characteristic of low-pass filter and Helmholtz resonator. *Applied Acoustics*, vol. 74, no. 1, p. 49-57, DOI:10.1016/j.apacoust.2012.06.007.
- [3] Chiu, M.C. (2013). Numerical assessment for a broadband and tuned noise using hybrid mufflers and a simulated annealing method. *Journal of Sound and Vibration*, vol. 332, no. 12, p. 2923-2940, DOI:10.1016/j.jsv.2012.12.039.
- [4] Chiu, M.C., Chang, Y.C. (2008). Shape optimization of multi-chamber cross-flow mufflers by SA optimization. *Journal of Sound and Vibration*, vol. 312, no. 3, p. 526-550, DOI:10.1016/j.jsv.2007.11.003.
- [5] Yu, X., Cheng, L. (2015). Duct noise attenuation using reactive silencer with various internal configurations. *Journal of Sound and Vibration*, vol. 335, p. 229-244, DOI:10.1016/j.jsv.2014.08.035.
- [6] Hwang, Y., Lee, J., Min Kim, Seung-Jong (2003). New active muffler system utilizing destructive interference by difference of transmission paths. *Journal of Sound and Vibration*, vol. 262, no. 1, p. 175-186, DOI:10.1016/S0022-460X(02)01378-0.
- [7] Liu, B., Maeno, M., Hase, S., Wakamatsu, S. (2003). A study of a dual mode muffler. *SAE Technical Paper*, p. 1647, DOI:10.4271/2003-01-1647.
- [8] Kuo, S.M., Morgan, D.R. (1996). *Active Noise Control Systems Algorithms and DSP Implementations*. John Wiley & Sons, New York.
- [9] Landaluze, J., Portilla, I., Pagalday, J.M., A. Martínez, A., Reyero, R. (2003). Application of active noise control to an elevator cabin. *Control Engineering Practice*, vol. 11, no. 12, p. 1423-1431, DOI:10.1016/S0967-0661(03)00077-7.

- [10] Tamamura, M., Shibata, E. (1996). Application of active noise control for engine related cabin noise. *JSAE Review*, vol. 17, no. 1, p. 37-43, DOI:10.1016/0389-4304(95)00047-X.
- [11] Chen, S.R., Too, G.P.J. (2009). Simulations and experiments for hybrid noise control systems. *Applied Acoustics*, vol. 70, no. 2, p. 247-255, DOI:10.1016/j.apacoust.2008.04.005.
- [12] Prezelj, J., Čudina, M. (2007). Dipole in orthogonal direction as a secondary source for active noise control in ducts. *Acta Acustica united with Acustica*, vol. 93, no. 1, p. 63-72.
- [13] Li, K., Tanaka, T. (2001). Development of an adaptive control simulation system for vehicle exhaust noise reduction. *JSAE Review*, vol. 22, no. 2, p. 157-162, DOI:10.1016/S0389-4304(00)00104-1.
- [14] Cuesta, M., Cobo, P. (2001). Optimisation of an active control system to reduce the exhaust noise radiated by a small generator. *Applied Acoustics*, vol. 62, no. 5, p. 513-526, DOI:10.1016/S0003-682X(00)00060-8.
- [15] Howard, C.Q., Craig, R.A. (2014). An adaptive quarter-wave tube that uses the sliding-Goertzel algorithm for estimation of phase. *Applied Acoustics*, vol. 78, p. 92-97, DOI:10.1016/j.apacoust.2013.12.002.
- [16] Huang, L. (2009). Attenuation of low frequency duct noise by a flute-like silencer. *Journal of Sound and Vibration*, vol. 326, no. 1-2, p. 161-176, DOI:10.1016/j.jsv.2009.05.004.
- [17] Bartlett, H., Whalley, R. (1998). Modelling and analysis of variable geometry exhaust gas systems. *Applied Mathematical Modelling*, vol. 22, no. 8, p. 545-567, DOI:10.1016/S0307-904X(98)10056-2.
- [18] Cherrier, O., Pommier-Budinger, V., Simon, F. (2012). Panel of resonators with variable resonance frequency for noise control. *Applied Acoustics*, vol. 73, no. 8, p. 781-790, DOI:10.1016/j.apacoust.2012.02.011.
- [19] Kostek, T.M., Franchek, M.A. (2000). Hybrid noise control in ducts. *Journal of Sound and Vibration*, vol. 237, no. 1, p. 81-100, DOI:10.1006/jsvi.2000.3056.
- [20] Howard, C.Q., Craig, R.A. (2014). Noise reduction using a quarter wave tube with different orifice geometries. *Applied Acoustics*, vol. 76, p. 180-186, DOI:10.1016/j.apacoust.2013.08.006.
- [21] Xu, M.B., Selamet, A., Kim, H. (2010). Dual Helmholtz resonator. *Applied Acoustics*, vol. 71, no. 9, p. 822-829, DOI:10.1016/j.apacoust.2010.04.007.
- [22] Davis, D., Stokes, G., Moore, D., Stevens, G. (1954). Theoretical and experimental investigation of mufflers with comments on engine-exhaust muffler design. *NACA Annual Report, Langley Aeronautical Laboratory, Langley Field*.
- [23] Ver, I., Beranek, L. (2006). *Noise and Vibration Control Engineering*. John Wiley & Sons, New Jersey.
- [24] Peat, K.S. (2010). Acoustic impedance at the interface between a plain and a perforated pipe. *Journal of Sound and Vibration*, vol. 329, no. 14, p. 2884-2894, DOI:10.1016/j.jsv.2010.01.037.
- [25] Selamet, A., Lee, I.J., Huff, N.T. (2003). Acoustic attenuation of hybrid silencers. *Journal of Sound and Vibration*, vol. 262, no. 3, p. 509-527, DOI:10.1016/S0022-460X(03)00109-3.
- [26] Barbieri, R., Barbieri, N. (2006). Finite element acoustic simulation based shape optimization of a muffler. *Applied Acoustics*, vol. 67, no. 4, p. 346-357, DOI:10.1016/j.apacoust.2005.06.007.
- [27] Ji, Z.L., Selamet, A. (2000). Boundary element analysis of three-pass perforated duct mufflers. *Noise Control Engineering Journal*, vol. 48, no. 5, p. 151-156, DOI:10.3397/1.2827962.
- [28] Hu, F.Q. (2001). A stable, perfectly matched layer for linearized euler equations in unsplit physical variables. *Journal of Computational Physics*, vol. 173, no. 2, p. 455-480, DOI:10.1006/jcph.2001.6887.
- [29] Oliva, D., Hongisto, V. (2013). Sound absorption of porous materials - Accuracy of prediction methods. *Applied Acoustics*, vol. 74, no. 12, p. 1473-1479, DOI:10.1016/j.apacoust.2013.06.004.

# Effect of Dynamic Vents on the Thermal Comfort of a Passenger Car

Om Prakash Singh<sup>1,\*</sup> – Rohit Raut<sup>1</sup> – Mrinmoy Biswas<sup>1</sup> – Ramji Singh<sup>2</sup>

<sup>1</sup> Indian Institute of Technology Mandi, School of Engineering, India

<sup>2</sup> Aryabhata Knowledge University, India

*When a vehicle is parked under the direct sun, heat flux entering the cabin through the roof top becomes higher and thus, sets up high temperature gradients beneath the roof. Dynamic airvents are provided to cool the cabin when the air-conditioner is switched on. Unfortunately, the car manufacturer does not specify any guidelines for the driver/passengers regarding the use of dynamic airvents in cars. This study aims to investigate the effect of dynamic vents on the cabin temperature when cooling is initiated. Computational fluid dynamics (CFD) analysis was performed in three stages. In the first stage, temperature data were measured experimentally at various locations in the car and at different times of the day. In the second stage, a 3D CAD model of the same car was generated by measuring the design data. In third stage, a CFD model of the car was developed and used to validate the experimental data. Simulations were performed to study the effect of dynamic vents. The results shows that faster cooling of the cabin and maintaining a uniform temperature distribution inside the cabin is possible at a particular vent angle, which the manufacturer does not specify or indicate for the vehicle. These results suggest an energy saving potential without any changes in the air-conditioning unit itself.*

**Keywords:** thermal comfort, dynamic vents, computational fluid dynamics, HVAC, cabin temperature

## Highlights

- Effect of dynamic airvents on car cabin temperatures are reported.
- CFD model is validated against experimentally measured data during the daytime.
- Uniform temperature distribution during the when cooling is initiated is observed for a particular vent angle.
- For the first 3 to 4 minutes the car air-conditioner should be operated at a high flow setting using the dynamic vents.
- Results can be utilized to save energy without any changes in the air-conditioning unit.

## 0 INTRODUCTION

Environment friendliness and energy efficiency are the mantra of today's world in each and every sector of development. The automotive industry is also now switching to zero emission car concepts to be in congruence with this concept. During this transformation, however, consumer satisfaction should not be hampered. The consumer is satisfied if he feels comfortable using a given commodity. Comfort, being a physiological or psychological factor, is basically a subjective term. Thermal comfort is therefore also a subjective term, dependent on heat conduction, convection, radiation and evaporative heat loss. Thermal comfort is the condition of mind that expresses satisfaction with the thermal environment and is assessed by subjective evaluation (ANSI/ASHRAE Standard 55) [1]. The predicted mean vote (PVM) is the most recognized thermal comfort model whose seven point scale varies from -3 (cold) to +3 (hot). Zero is the ideal value, representing thermal neutrality, i.e. a neutral thermal sensation is achieved when the human body is in thermal equilibrium with the surroundings. Heat generated by a human body

depends on the metabolism of the system. Each part of human body has a different metabolism rate. Because of the numerous differences between the physiological and psychological satisfaction of human beings it is very difficult to pinpoint a temperature that would provide the same level of thermal comfort to every passenger of a vehicle. The thermal comfort for the passenger of the car is maintained by the HVAC (Heating, Ventilation and Air-Conditioning) system. Therefore, the number of vents, air-flow temperature and velocity, cabin temperature and relative humidity are the main parameters that control the inner environment of a passenger car. The thermal comfort sensation is optimal when the relative humidity value is about 50 %. Humidity fluctuations play a minor role if the values are in the range of 30 % to 70 % [2]. Thermal comfort in the vehicle is achieved (i) by ensuring temperatures of 20 °C to 22 °C, as a result of air temperature, delimitation areas, humidity and air velocity in accordance with the activity level and clothing insulation of the occupants, (ii) by avoiding situations such as the occupants coming into contact with very cold or very hot surfaces, (iii) by avoiding air

\*Corr. Author's Address: Indian Institute of Technology Mandi, School of Engineering, India, om.prakashh.singh@gmail.com

currents. These requirements must be met throughout the entire year, both in summer and wintertime [2].

Much research has been carried out to enhance the thermal comfort inside the passenger car. Chen et al. [3] in their research suggested an energy efficient way of delivering comfort to an occupant in the car. Their research focused on the design and CFD analysis of an energy efficient HVAC system with spot cooling by strategically placing multiple nozzles in the vehicle directed at specific body parts. In their experiment the nozzle design and nozzle locations were paramount to deliver and achieve energy efficiency. In another research paper on the design of dynamic air vents and airflow analysis in a passenger car cabin by Varad et al. [4] they suggested the concept of dynamic vents. They analyzed the effect of dynamic vents and compared them with the steady air vent model. The results projected a considerable drop in the average cabin temperature. They also noted various effects of dynamic air vents. Walgama et al. [5] in their paper classified the work with respect to the passenger compartment environment or the condition of the passengers and their interaction with the compartment. The effects of factors such as flow field and temperature field were taken into consideration. They proposed computational and empirical models for forecasting thermal comfort in the non-uniform transient environment of the passenger car. Studies of air-flow and temperature fields inside a passenger compartment for improving thermal comfort and saving energy was investigated by Zhang et al. [6]. They investigated the influence of different factors on thermal comfort and energy consumption. Temperature distributions and the flow field inside a passenger car were simulated and analyzed with and without passengers. Their simulation results revealed various factors that ameliorate the thermal comfort and energy consumption such as the significance of air inlet temperature and the external conditions. The results also showed that the number of passengers also affects the conditions. The window materials also influence the thermal insulation of the vehicle. To improve the uniformity of the temperature field around the driver's foot zone a better flow circulation near the compartment bottom is favorable, for example, Ruzic [7].

Ruzic [7] used the method of localized distribution of air to improve thermal comfort. Alexandrov et al. [8] used CFD methods to investigate the flow patterns inside the car cabin. One interesting study by Wan and Kooi [9] was that they investigated the position of supply and exhaust opening on comfort in a passenger car. They showed that optimizing the

location of the exhaust system maximizes thermal comfort. There have been numerous studies in the recent past on thermal comfort using CFD. Recently, Zval et al. [10] presented a three-dimensional adiabatic flow simulation in an air-conditioned vehicle passenger compartment and proposed a combination of turbulence models and near wall treatment that can be used for simulations of thermal comfort and determination of comfort of driver and passengers. They performed CFD modeling using models such as eddy - viscosity standard, RNG k- $\epsilon$  and SST k- $\omega$  models. Although the thermal comfort of vehicles has been studied extensively, Ismail et al. [11] went a step further to investigate the thermal comfort assessment of workers in automotive industries. They reported that most of the workstations in the automotive industry were uncomfortable.

The greenhouse effect in passenger cars happens when the greenhouse gases trapped inside a passenger car absorb the thermal radiation from the sun and re-radiate it inside in all direction, thus increasing the cabin temperature. This effect is prominent when we park the car for few hours in direct sunlight with all the windows closed. There is a considerable difference in the external ambient temperature and the temperature inside the cabin. In order to overcome this issue a precooling system such as a solar powered pre-cooling ventilation system on the roof or remote-activated air-conditioning for pre-cooling the cabin has to be embedded so that the car cabin can be cooled before the passenger enters the car. However, the problem with this system is the high cost. A high additional cost will have to be borne by the customer for installing this system. A completely new system also has to be placed in the car to incorporate the additional unit. In today's world where cars are becoming more and more optimized, incorporating a new technology for cooling is not efficient and increases the weight of the overall system.

The aim of this research is to find a solution to this problem without too many changes to the current air-conditioning system. The car manufacturers do not specify the vane angle and air speed so that faster cooling can be initially achieved. Energy could also be saved since a particular vane angle cools only a certain part of the cabin space, which may or may not be useful. We have investigated the effect of vane direction and inbuilt speed to find the optimal angle and speed to maximize the cooling as quickly as possible. We have also incorporated the system of dynamic vents and analyzed its effect on the rate of cooling and average cabin temperature. The speed of oscillation of the vents has also been investigated.

## 1 CFD MODEL

## 1.1 Computational Domain and Boundary Conditions

The computational domain incorporates the space inside the cabin including the front and back seats. The inner surfaces of the passenger cabin including the top surface, the sidewall and the dashboard region constitute the boundary of the computational domain. The cabin design is of a typical passenger vehicle (in this case a hatchback, Maruti Suzuki Alto 800). The  $z=0$  plane passes through the center of the cabin space dividing the space into two symmetrical halves. Two separate armchairs are there on each side of  $z=0$  plane in the front area, whereas a long bench at the rear sheet serves for the rear passengers.

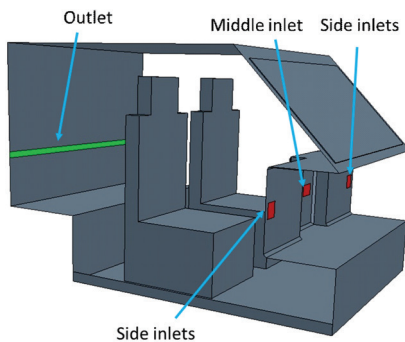


Fig. 1. Airflow inlets and outlets of the cabin space

The air-inlets are present on the dashboard as shown in Fig. 1, two inlets at the center of the dashboard, which will be referred as center inlets and two air-inlets one on each side of the driver and passenger near the front windows. All inlets are horizontally aligned, while air outlet is positioned on the rear wall. This is an assumed exit since the air-conditioning works in outside-circulation mode. The boundaries, i.e. the top surface, sidewalls, back wall, doors and windows, are treated as solid walls. The cabin is assumed to be sealed from the inside thus eliminating additional air flow interaction. The flow condition is assumed to be incompressible with constant thermo-physical properties of air. The gravity is defined in the computational domain in the negative  $Y$  direction i.e. downward direction. The air inlet velocity is different for two different cases, one medium-flow and one high-flow. In the medium flow case, the specification of the air velocity is 4.5 m/s for the center inlets and 2 m/s for the side inlets. While in the high flow case, the air-inlet velocity is set at 6.3 m/s for the center inlets and 3 m/s for the side inlets.

The turbulent intensity was set at 10% everywhere and a flow-split outlet was set as the air-outlet boundary condition. The walls of the cabin also serve as a different type of boundary condition as these are the interface between the interior of the cabin and the outside ambient conditions. Solar heat flux enters the cabin from all the windows, the total radiation entering depends on the angle of incidence  $\alpha$ . To calculate the incident radiation heat flux density, we used the equation:  $P = \varepsilon\sigma AT^4$ , where  $\varepsilon$  is the surface emissivity,  $\sigma$  is the Stefan–Boltzmann constant ( $5.67 \times 10^{-8} \text{ W}/(\text{m}^2 \cdot \text{K}^4)$ ),  $T$  is the surface temperature in Kelvin and  $A$  is the surface area. The car surface was coated with white paint whose emissivity is 0.9, the total projected surface area was 1.92 m<sup>2</sup> and the surface temperature was 318 °K. Using the above equation, the solar irradiation comes out be 1000 W/m<sup>2</sup>. For surfaces like the top bottom surface windows, windscreens and side walls, the following equation based on Newton's law is used to calculate the heat flux due to solar radiation [12],

$$q = h_0(t_0 - t_w) + \alpha G,$$

$$q = h_0 \left[ \left( t_0 + \frac{\alpha G}{h_0} \right) - t_w \right] = h_0(t_z - t_w), \quad (1)$$

$$t_z = t_0 + G/h_0, \quad (2)$$

where  $q$  is a heat flux [W/m<sup>2</sup>];  $h_0$  convective heat transfer coefficient [W/(m<sup>2</sup>·K)];  $t_0$  outside air temperature [°C];  $t_w$  outside surface temperature of the cabin [°C];  $\alpha$  absorptivity of sun radiation;  $G$  incident radiation heat flux density (solar irradiation) [W/m<sup>2</sup>];  $t_z$  synthetic temperature [°C]. The synthetic temperature is derived to ease the process of calculating solar heat flux using Newton's law of cooling as shown in Eq. (1). The convective heat transfer coefficient is calculated as follows:

$$h_0 = 1.163(4 + 12\sqrt{\nu}), \quad (3)$$

where  $\nu$  is the wind speed relative to the vehicle in m/s. The calculated  $h_0$  was 31 W/m<sup>2</sup>K with a standard deviation of 1.51 based on the ambient velocity variation.

The window glass is transparent to most solar radiation. The radiation effect is neglected in the simulation and hence, from the available data of the radiation intensity, the area of the window and the incident angle of solar radiation, the calculated heat flux is assumed to enter from the top surface. The seat boundaries are set to flow obstacles with zero heat flux, i.e. they do not contribute to the heat entering into the cabin.

## 1.2 Grid Generation and Numerical Methods

Unstructured grids with tetrahedron elements have been adopted, with the size of elements given as 1 cm except for the air inlets and outlets and the top surface. The air-inlets and outlets are refined locally with an element size of 1 mm since a larger temperature and velocity gradient is present at these locations. At the top surface the element size is 6 mm since a constant solar heat flux is entering the cabin space from the top surface. The total numbers of control volumes present in the computational domain are 118,000. The results are grid independent.

The governing equation used is unsteady incompressible, staggered flow discretized by the finite volume method. The transient term is discretized using a second-order implicit scheme with a time step of 1 s and inner iteration of 20 between time steps. A second-order upwind differencing scheme was used for the convection term and a central diffusion scheme for the diffusion term. A standard  $\kappa$ - $\epsilon$  turbulent model was used along with the SIMPLE algorithm to deal with the pressure-velocity coupling. Star CCM+ 7.0 commercial software was used for the simulation, while Hypermesh 7.0 student's license for pre-processing and generating the mesh. Star CCM+ software is widely used in the automotive industry [13].

## 2 EXPERIMENTS

### 2.1 Experimental Conditions

For the validation of the results, experiments were conducted inside the cabin of a Maruti Suzuki Alto 800, i.e. a passenger car. The parameters measured were temperature at various sample points and air-inlet temperature. Portable anemometer and thermocouples were used to measure air velocity and temperatures, respectively. The experiments were carried out at noon with an ambient temperature of 38 °C and relative humidity of 15 %. The test was performed after the car had reached a steady state standing in a parking environment with the sun directly overhead ( $\alpha = 0$ ), irradiation = 1 kW/m<sup>2</sup>. The experiments were repeated over a few days to investigate the repeatability and variability in measurement conditions. We observed an approximate 4 % difference in the results due to variation in climatic conditions. The total time of the experiment was 10 minutes. This was to study the fastest mode of cooling a cabin that has reached a steady state while standing idle in a parking area as already discussed in the problem statement. Since

the duration of experimentation was small, the outside conditions can be taken as constant during the test.

### 2.2 Validation with Experimental Data

The collected data from the various sample points are compared to the predicted values obtained using the CFD model. The cabin space is divided into four parts by the planes  $z=0$  m and  $x=1.5$  m and named as driver, passenger and rear passengers. Fig. 2 shows the sampling points for validation for each passenger, 3 for the driver and front passenger, one each at head, knee and foot region. For the back passengers 2 points were under consideration, one each at the head and foot region. The names of these points have been assigned based on the division of space and will be referred by the same names in further discussion. The average wind speed was 13 km/h during the experimentation. The sampling rate was set to 10 seconds.

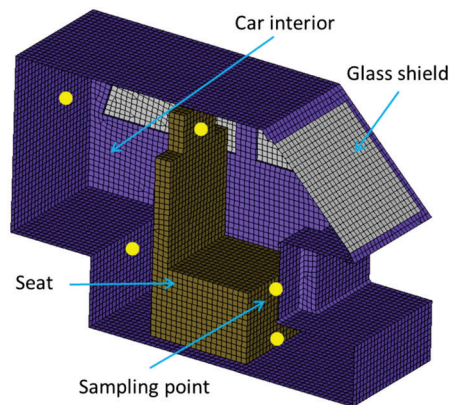


**Fig. 2.** Half-section view of the cabin showing the sampling points marked with yellow dots for validation with experiments

The initial temperature inside the cabin was found to be 43 °C which was mainly due to the greenhouse effect taking place inside the cabin. The air-inlet temperature was 20 °C and the air conditioner was working in external circulation mode with a high flow setting. Fig. 3 shows the comparison between the results predicted from the CFD model and the measured temperature. It can be seen that trends in temperature variation are well captured by the software. Furthermore, the maximum difference between the predicted and measured temperature is less than 10 %, which is acceptable. In order to improve the accuracy of the data, four thermocouples were used at each of the sample point and an average of the input was taken. The air-inlet velocity was measured using a Testo hot-wire anemometer whose

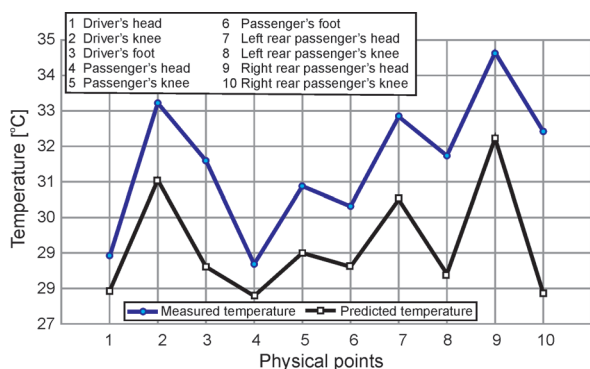


Fig. 3. Comparison with predicted temperature from CFD model and experimental data

range and accuracy were as follows: velocity range: 0 to 20 m/s, air velocity resolution:  $\pm 0.01$  m/s, air velocity accuracy:  $\pm 0.3$  m/s,  $\pm 5\%$  mV, temperature resolution: 0.1 °C, temperature range: -20 °C to 71 °C, temperature accuracy:  $\pm 0.5$  °C. The vents were set at different flow settings such as high, medium and low air velocity. The anemometer was placed directly in front the vents. This multi-direction air velocity measuring anemometer features both timed mean (mean value calculated over a user-specified time) and multipoint mean (mean value calculated over user-entered point measurements) to help track variable flows and cyclical events. We used the timed mean air velocity measured every 5 seconds. There was no velocity fluctuation in the measured inlet vent velocity as engine load and speed were constant. Fig. 4 shows the temperature variation at various locations (see legend) with time. Note that the temperature fluctuates with time and reaches a steady case after 240 s. These temperatures correlate well the measured temperatures to within ten percent accuracy as shown

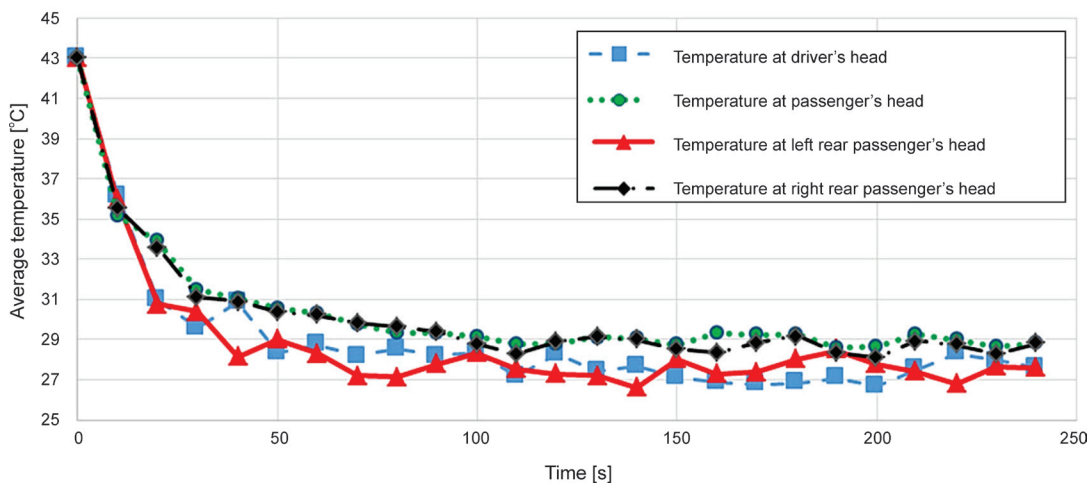


Fig. 4. Temperature variation with time at different locations

in Fig. 3. It is to be mentioned here that the results presented are in terms of cabin temperature and not on a thermal sensation scale as recommended by ASHRE standards [14] and [15]. One reason being that the industry generally relies on direct temperature measurement and later interpret it on a thermal sensation scale. While the thermal index for comfort is useful, a temperature scale serves as an important input for industry to perform various design changes.

### 3 RESULTS AND DISCUSSIONS

#### 3.1 Effect of Different Flow Variables

As discussed earlier, different researchers have attempted to simulate and obtain a homogenous temperature distribution inside the car. Most of them tried to mix and match different variables, some accounting for the car body color, others testing the flow speeds and location of vents. Few took account of the role of passengers as a heat source and also reduced the effect of radiation with reflection coating. In our case we first studied the effect of air-flow positioned at different angles. Based on the results, the best possible angles were then selected and a dynamic flow inlets model was developed where the angles of the inlets were kept periodically oscillating between the chosen angles. The different attempts and their results are discussed below.

##### 3.1.1 Medium Flow at Zero, 30 Degrees, 45 Degrees and 60 Degrees Positive Form the Horizontal

Medium flow means that the center inlets deliver at 4.5 m/s and side inlets at 2 m/s velocity. The

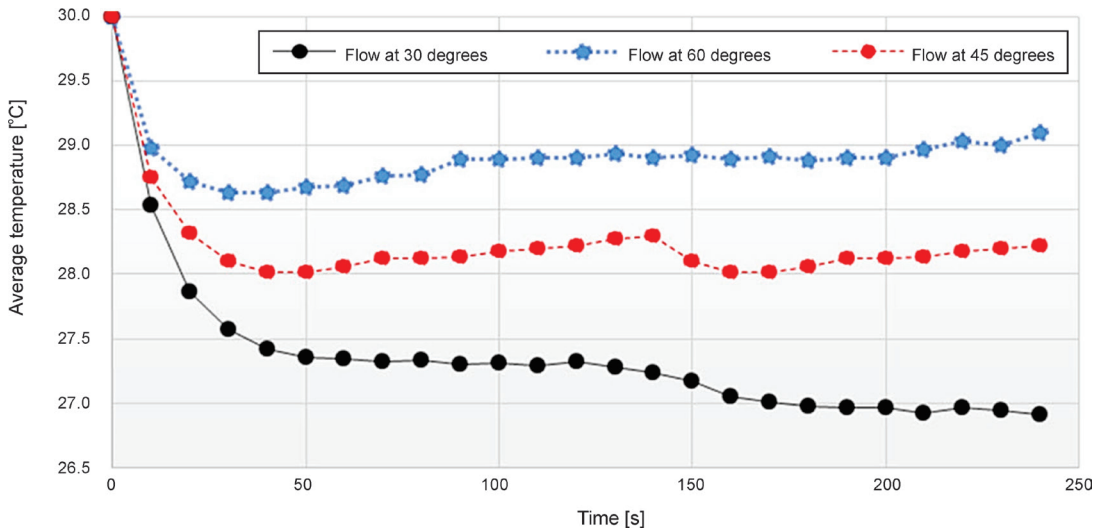


Fig. 5. Plot of average temperature vs. time for flow inlets at 30 degree, 45 degrees and 60 degrees

exterior conditions were measured to be 24 °C ambient temperature, 20 % humidity and an average wind velocity of 13 km/h. The cabin steady state temperature was 30 °C. Here the angles mentioned are measured positively from the horizontal. The simulation time was four minutes with a time step of 10 s. Hence the whole simulation was done in 240 s or 4 min. This is because in order to cool the car one needs to do the maximum work in the initial phase, which will be in the first 3 min to 4 min.

Comparing the plots of volume average temperature inside the computational domain vs. time (Fig. 5), it is observed that the vent flow is able to cool the cabin area when angled at 30 degrees. A drop

of 3 degrees was obtained during the first 4 minutes. Although the results are comparable with the case of zero degrees it was also observed that the flow at 30 degrees seems to cool the front seats better than other three cases. Flow at 60 degrees also affects the cooling but marginally, as temperature drop was only 1 °C.

**3.1.2 High Flow at Zero, 30 Degrees, 45 Degrees and 60 Degrees Positive Form the Horizontal**

All the operating conditions mentioned in Section 3.1.1 remain the same, only the flow speed is varied in this case. High flow means the center inlets deliver cooling airflow at 6.3 m/s and the side inlets at 3 m/s.

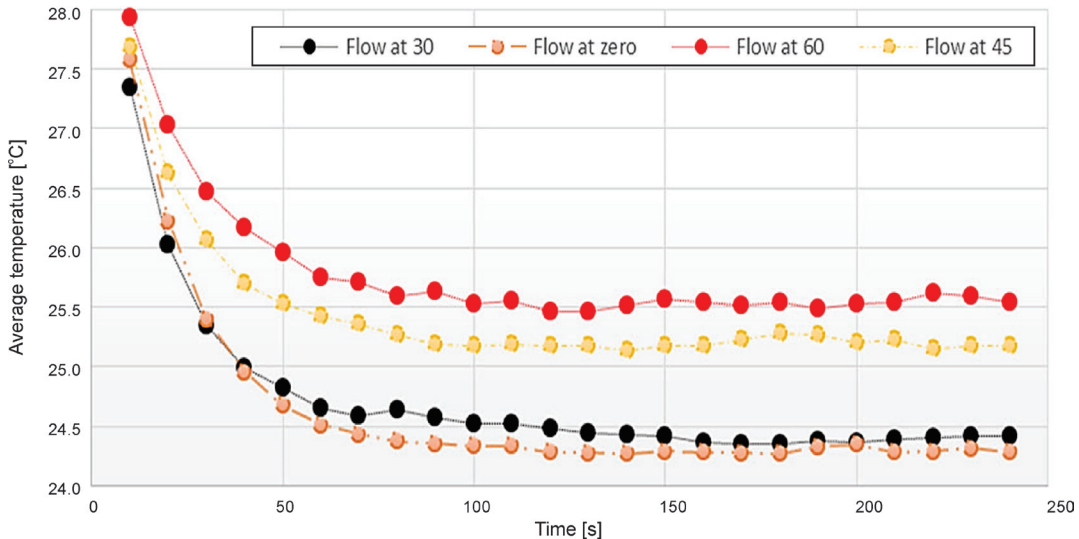


Fig. 6. Plot of Average temperature vs. time for flow inlets at zero degree, 30 degree, 45 degrees and 60

The plots depict similar results as predicted earlier with the airflow at 30 degrees. The only change is that the temperature drops obtained in this case have increased, as shown in Fig. 6.

The velocity vector plot and the temperature scalar plots also suggest the same phenomenon. The air-flow circulation phenomena observed earlier can also be seen in the high flow case (Figs. 7 and 8). When positioned at 30 degrees the air inlets are now able to cool the front region to 23 degrees and the average temperature drops by 6 °C. Although the objective to cool the cabin has been achieved, non-homogeneity of temperature still remains a challenge. Similarly, when vanes angles are at 60 degrees the inlets are not able

to cool the front as effectively as with 30 degrees. However, since the flow rates are higher the average temperature now drops by 5 degrees. Vane angles of 45 degrees performs only slightly better than those at 60.

### 3.2 Effect of Dynamic Air-Inlets

From the earlier discussion in Sections 3.1.1 and 3.1.2 it is clear that each angle is successful in cooling one or the other region at about the  $X = 1.5$  m plane. Flow at 30 degrees cools the front half and achieves the maximum drop in temperature, flow at 60 degrees manages to cool the rear slightly, whereas flow at 45

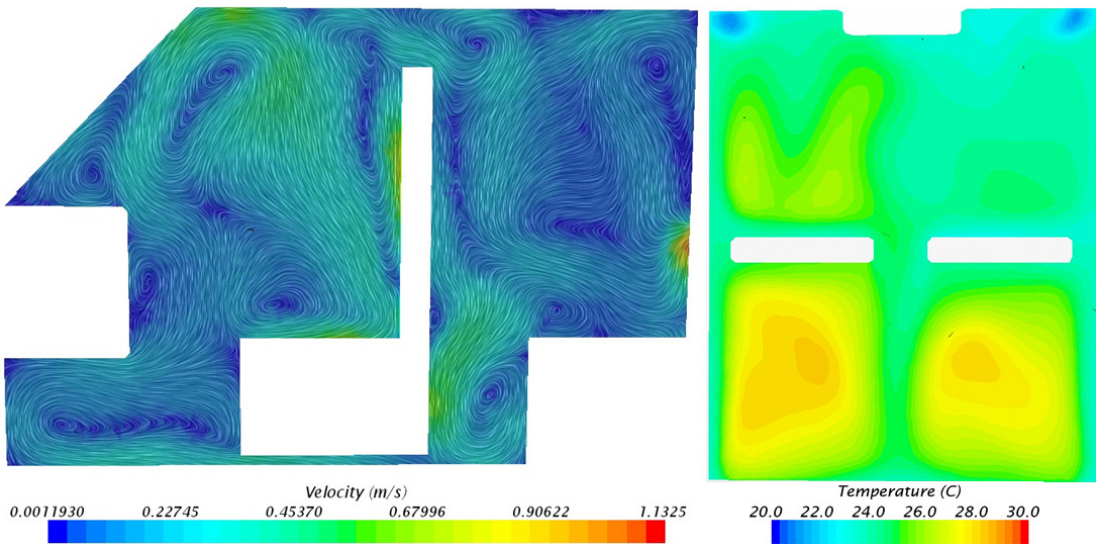


Fig. 7. High flow at a flow angle of 30 degrees. Left: velocity vector and, right: temperature contours

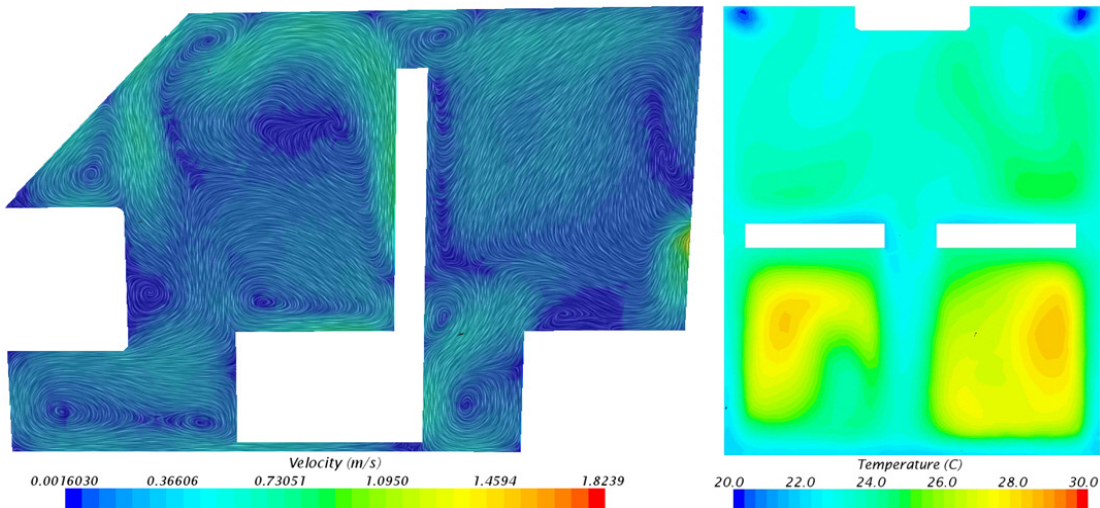


Fig. 8. High flow at a flow angle of 60 degrees

degrees creates a homogenous temperature drop. The circulation keeps the heated air in the same region as in the case of 60 degrees. Thus the heated air has to be continuously replaced and re-circulation should be used wisely.

Thus to study the effect of all these, the concept of dynamic vents was attempted next and simulated in the computational domain. Dynamic vents describe air-inlet vents that swing automatically between the chosen flow angles at some set frequency. This way the vents can cover all the angles from 30 degrees to 45 degrees and then 45 degrees to 60 degrees. Accordingly, changes in angles and frequency for different cases have been made and discussed further.

**3.2.1 Dynamic Vents with Flow Angles Covering Zero to 30 Degrees with Medium Flow Setting**

In this case the vents go from zero to 30 degrees in 8 seconds. The flow rate is set at a medium setting and other conditions remain the same as in Section 3.1. The simulation time is 4 min. It was observed that dynamic vents have been successful in cooling the rear area with a minimum temperature of 24.5 °C. They have also performed better in maintaining a uniform distribution. Nevertheless, the average temperature is still recorded to be 26 °C (Fig. 9 shows temperature at x = 1.5 m). Thus the test with dynamic vents has shown that uniform temperature distribution is possible, which has encouraged us to make further simulations with different variable angles.

**3.2.2 Dynamic Vents with Flow Angles Covering Zero to 30 Degrees with High Flow Setting**

In this case, the high flow cooled the cabin by 6 degrees but the effect cannot be ascribed to the dynamic vents at a medium flow setting. The temperature drop attained is mainly due to the increased flow rate.

The above discussion demonstrates that the use of dynamic vents can achieve the desired uniformity. In Section 3.1 and sub-sections it was concluded that a flow angle of 30 degrees cools the front and 60 degrees cools the back whereas 45 degrees lies in between. Hence, we shall now try to use the results of both stationary and dynamic vents, thereby resulting in further tests where the vents will now traverse 30 degrees to 60 degrees at different frequencies.

**3.3 Dynamic Vents with Flow Angles Covering 30 Degrees to 60 Degrees**

As discussed earlier, the whole cabin should be cooled as the vents will traverse all the angles earlier investigated. It was observed that for both medium and high flow rates the cooling effects are similar. The high flow cools the cabin interiors at a fast rate with a drop of 6.7 °C.

The temperature distribution is also uniform in the high flow case, as seen in the former case. Thus, the results cannot be concretely credited to the dynamic vents. Next we try to vary the frequencies of traversing the angle so as to arrive at more concrete conclusions.

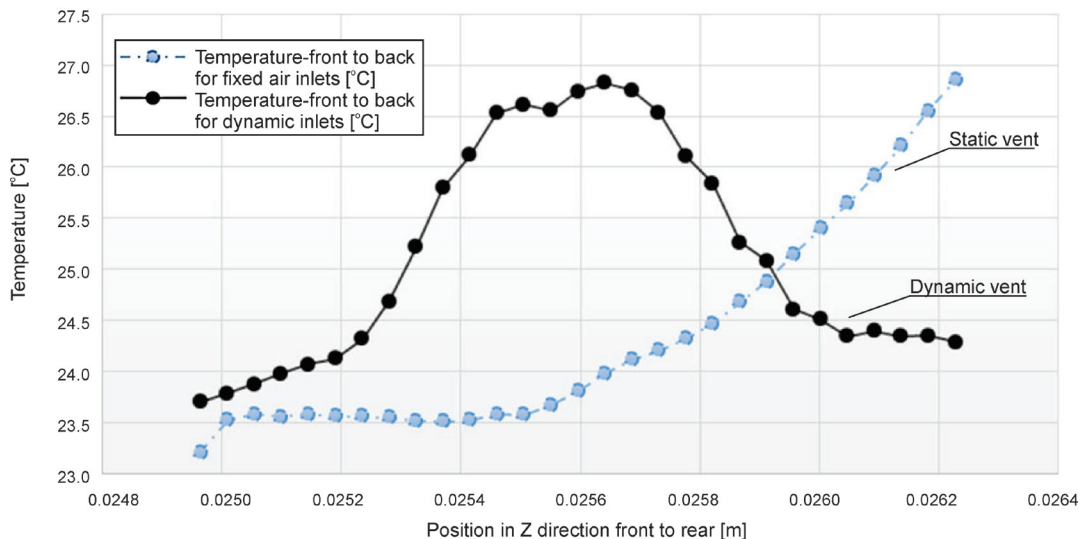


Fig. 9. Comparison of X-Y Plot of average temperature from front to back on a horizontal plane between stationary and dynamic vents

### 3.4 Dynamic Vents with Flow Angles Covering 30 Degrees to 60 Degrees in 6 Seconds

All the external conditions are similar to those in the earlier cases and no changes have been made to the vents, only the frequency at which the vents sweep has been changed. The vents now traverse the angles 30 to 60 periodically in 6 s and back. Comparing the temperature contours (Fig. 10 and 11) for both the medium and high flow settings it is observed that both of these settings are able to provide a uniform temperature distribution. The average temperature for a medium setting is 25.8 °C, whereas for the high flow setting the average temperature drops to 23.6 °C. Thus, changing the frequency has resulted in dropping the temperature inside the cabin as well as maintaining uniformity.

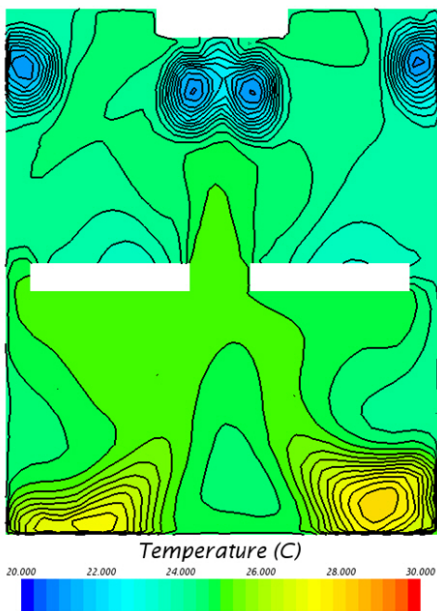


Fig. 10. Top view of temperature contour with dynamic vents traversing 30 degrees to 60 degrees in 6 s at a medium flow setting

By further increasing the frequency, where the half time period is 4 s, no significant change is observed and the results are quite similar. Thus, any frequency whose time period is below 12 s is able to generate the desired effect, but due to constraints on the efficiency of such mechanical systems the optimum frequency would be when the time period is 12 s. Results are summarized in Table 1.

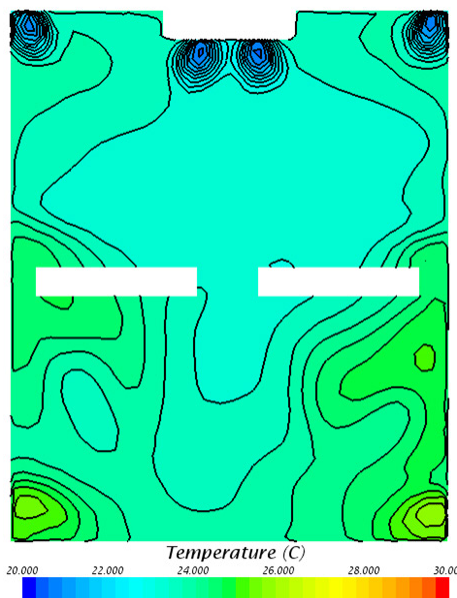


Fig. 11. Top view of temperature contour with dynamic vents traversing 30 degrees to 60 degrees in 6 s using a high flow setting

Table 1. Summary of volume averaged temperature drop at various angles; the highest temperature drop was observed for dynamic vents for 30 degrees to 60 degrees

Cases	Temperature drop (Angles)	Temperature drop (Angle Sweep)
Static vents	5.75(0), 5.52(30), 4.75(45), 4.50(60)	
Dynamic vents		6 (0 to 30), 6.7 (30 to 60)

#### 4 CONCLUSIONS

It is evident that the maximum temperature drop is obtained when the vent angle is 30 degrees. The average temperature in this case was 26.8 °C at a medium setting and 24.45 °C at a high flow setting after 4 min. However, the temperature distribution was not homogenous and the vents were unable to cool the rear area.

A further drop was obtained in the case of dynamic vents sweeping angles from 30 degrees to 60 degrees in 6 s. The average temperature in this case was 25.8 °C at a medium flow setting and 23.6 °C at a high flow setting after 4 minutes from the start and, thus contributing to an extra drop of 1 °C in both high and medium settings as compared to static vent analysis. Additionally the temperature distribution obtained is uniform throughout the cabin space. Hence it is proposed on the basis of the results that for the

first three to four minutes the air-conditioner should be operated at a high flow setting using the dynamic vents as discussed earlier. Then the regular mode of operation can be used. An eccentric rotating shaft can be used to convert static vents into dynamic vents. Home air-conditioners use dynamic vents to achieve quicker cooling.

All these results show the scope for future study where changes can be made to the positions of the vents. Additional air-inlets can be incorporated on the roof top for the rear passengers since this is a difficult area to cool. The effect of changing the flow rate by using a more powerful air-conditional system can also be studied. Studies have already been carried out to provide a particular passenger with a particular temperature setting. This can be achieved through the use of spot-cooling using nozzles, which is an emerging area of research in the field of passenger comfort. Moreover the effect of passengers and their body heat can also be included in the simulations and make the system closer to a real life situation.

However, it should be noted that any modifications to the air-conditioning system would put an additional burden on the engine and thus affect the efficiency of the engine along with increasing the cost of running the car. Hence, a compromise has to be made while selecting the variables for optimum efficiency... and comfort.

## 5 REFERENCES

- [1] ANSI/ASHRAE Standard 55-2013, *Thermal Environmental Conditions for Human Occupancy*. Approved American National Standard, Atlanta.
- [2] Musat, R., Helerea, E. (2009). Parameters and models of the vehicle thermal comfort. *Acta Universitatis Sapientiae, Electrical and Mechanical Engineering*, vol. 1, p. 215-226.
- [3] Chen, K.H., Kaushik, S., Han, T., Ghosh, D., Wang, M. (2012). Thermal comfort prediction and validation in a realistic vehicle thermal environment. *SAE Technical Paper*, 2012-01-0645, DOI:10.4271/2012-01-0645.
- [4] Limaye, V.M., Deshpande M.D., Sivapragasam, M., Kumar, V. (2012). Design of dynamic airvents and airflow analysis in a passenger car cabin. *SASTech – Technical Journal*, vol. 11, no. 1, p. 41-48.
- [5] Walgama, C., Fackrell, S., Karimi, M., Fartaj, A., Rankin, G.W. (2006). Passenger thermal comfort in vehicles—a review. *Proceedings of the Institution of Mechanical Engineers, Part D: Journal of Automobile Engineering*, vol. 220, no. 5, p. 543-562, DOI:10.1243/09544070D00705.
- [6] Zhang, H.-J., Dai, L., Xu, G.-Q., Li, Y., Chen, W., Tao, W.-Q. (2009). Studies of air-flow and temperature fields inside a passenger compartment for improving thermal comfort and saving energy, Part I: Test/numerical model and validation. *Applied Thermal Engineering*, vol. 29, no. 10, p. 2022-2027, DOI:10.1016/j.applthermaleng.2008.10.005.
- [7] Ruzic, D. (2011). Improvement of thermal comfort in a passenger car by localized air distribution. *Acta Technica Corviniensis - Bulletin of Engineering*, vol. 4, no. 1, p. 63-67.
- [8] Alexandrov, A., Kudriavtsev, V., Reggio, M. (2001). Analysis of flow patterns and heat transfer in generic passenger car mini-environment. *9<sup>th</sup> Annual Conference of CFD Society of Canada*, Ontario, p. 27-29.
- [9] Wan, J.W., van der Kooij, J. (1991). Influence of the position of supply and exhaust openings on comfort in a passenger vehicle. *International Journal of Vehicle Design*, vol. 12, no. 5-6, p. 588-597, DOI:10.1504/IJVD.1991.061702.
- [10] Zvar Baskovic, U., Lorenz, M., Butala, V. (2014). Adiabatic flow simulation in an air-conditioned vehicle passenger compartment. *International Journal of Simulation Modelling*, vol. 13, no. 1, p. 42-53, DOI:10.2507/IJSIMM13(1)4.253.
- [11] Ismail, A.R., Karagaratnan, S.K., Kadirgama, K. (2013). Thermal comfort findings: scenario at Malaysian automotive industry. *Thermal Science*, vol. 17, no. 2, p. 387-396, DOI:10.2298/TSCI1111110151.
- [12] Muhammad Iqbal (2012). *An Introduction to Solar Radiation*, 1<sup>st</sup> ed., Elsevier, New York..
- [13] Ahmad, N. E., Abo-Serie, E., Gaylard, A. (2010). Mesh optimization for ground vehicle aerodynamics. *CFD Letters*, vol. 2, no. 1, p. 54-65.
- [14] Attia, A., EL Helw, M., Teamah, H. (2013). Three-dimensional thermal comfort analysis for hospital operating room with the effect of door gradually opened, Part (II) Effect on mean age of the air and predicted mean vote distribution. *CFD Letters*, vol. 5, no. 2, p. 20-31.
- [15] Attia, A., EL Helw, M., Teamah, H. (2013). Three-dimensional thermal comfort analysis for hospital operating room with the effect of door gradually opened, Part (I) Effect on velocity and temperature distributions. *CFD Letters*, vol. 5, no. 1-2, p. 6-19.

# Grinding Tungsten Carbide Used for Manufacturing Gun Drills

Livia Dana Beju\* – Paul Dan Brindasu – Silvia Vulc

“Lucian Blaga” University of Sibiu, Engineering Faculty, Romania

*This paper presents a study of grinding cemented carbide DK460UF (91 % WC and 9 % Co), a material used to produce cutting tools with solid cutting edges. The aim is to establish the manufacturing conditions that lead to high surface quality. A model of the main factors that influence the grinding process is presented first. Following that, grinding wheel wear and surface roughness are analysed. Grinding wheel wear is studied in experimental conditions under which small diameter gun drills were sharpened with two diamond grinding wheels of different grain sizes. Finally, the wear curve can be made. The “G ratio” is used to characterise the performance of the grinding process. Next, the experimental research examines how independent parameters, depth of cut, feed, grit, and speed influence roughness. The influence of the grinding wheel wear on roughness is also studied. The aspect of ground surfaces is examined by using a scanning electron microscope (SEM). The experimental study allowed the determination of the required grinding wheel grit (46  $\mu\text{m}$ ) and the optimum processing parameters (depth of cut  $a_p = 0.01$  mm, feed = 0.005 mm/rev, cutting speed  $v = 55$  m/s) to obtain the imposed surface roughness for cutting tool surfaces ( $R_z = 0.3$   $\mu\text{m}$ ). The maximum allowed radial wear ( $\Delta r$ ) of the grinding wheel is 30  $\mu\text{m}$ .*

**Keywords:** tungsten carbide, grinding, grinding wheel, roughness, grit, wear

## Highlights

- The research is focused on analysing the grinding process of the cemented carbide DK460UF (91 % WC and 9 % Co), a material used to produce cutting tools with solid cutting edges.
- A theoretical study is conducted to detect the main factors that influence the quality of surfaces.
- An experimental analysis of tool wear is done.
- An experimental study of the roughness obtained by grinding under different cutting conditions is done.
- Optimal grinding parameters and maximum admissible wear of the grinding wheel necessary for obtaining the desired roughness are revealed.

## 0 INTRODUCTION

Grinding is a highly complex manufacturing process due to the stochastic nature of the active zone (composed of grains, binder, and pores) and, because of the large numbers of parameters, it influences the surface quality and material removal rate, which are the two main goals of this process.

An important grinding application is the sharpening of cemented carbide cutting tools. Additional features of these processes compared to other types of grinding are the following: the small surfaces to be processed, which have many edges; high surface quality; small production series; different depths of cut; and specific mechanical properties of the cemented carbides used for cutting tools. The application is important because the quality of the clearance and relief surfaces (of the cutting tool) is important for the precision of the manufactured surface and the tool life of the cutting tool.

The research focused on DK460UF tungsten carbide that consists of 91 % WC and 9 % Co. It is the main material used in twist drills, gun drills, end mills, etc.

The aim of this study was to determine the optimum manufacturing parameters that lead to the desired surface quality.

## 1 STATE OF THE ART

Given its importance, the grinding process has been the subject of many investigations. In his book [1], Shaw presents the first grinding models developed in the 1990s.

Currently, a large range of models are being developed. Some of them are physically focused. In this category, we include the fundamental analytical models, the kinematic, finite element method, regression and molecular dynamics. Empirical process models include regression and artificial neural models. The last category comprises the rule base models, which are heuristic [2].

Kinematic models explain the grinding mechanisms, the parameters involved in this process, and their interdependence.

Fig. 1 shows an original cumulative model of the main elements influencing the grinding process and the logical interaction between them.

\*Corr. Author's Address: “Lucian Blaga” University of Sibiu, Engineering Faculty, 4 Cioran, Sibiu, Romania, liviadana\_beju@yahoo.com

Starting from them, force models (which allow the prediction of wheel wear and the estimation of grinding energy) can be developed.

Using the previous models (wheel topography, chip thickness, and forces), the surface roughness can be predicted.

The grinding force model is the starting point for an energy model of the process. The grinding energy model allows the development of the temperature model, which is the starting point for the wear model as well as for the surface integrity model. In Fig. 1, it can be observed that a model of the processed surface quality can be generated starting from the tool wear model (grinding wheel).

The first kinematic models were developed by Law and Wu [3], using two-dimensional grain models. Three-dimensional models were developed by Chen and Rowe [4], Gong et al. [5], Inasaki [6], Koshy et al. [7], and Zhou and Xi [8].

High carbide hardness requires processing with diamond grinding wheels [9]. Increasing material volume and cutting depth causes an increase in grinding wheel wear. To obtain a low rate of grinding wheel wear we can use larger diameter discs. Depreciation is lower if the number of active grains on the wheel circumference is higher [10].

The problem of grinding wheel wear has been the subject of numerous analyses of the factors that accelerate the occurrence of this phenomenon. Knowing the process elements that enhance wear, it is important to monitor the behaviour of the grinding wheel during processing [11]. Some researchers have shown that wear depends on the length of contact between the wheel and the surface to be manufactured,

the pressure in the contact area, and cutting forces [12]. More specific aspects related to wheel wear grinding cemented carbides were presented by Liu et al. [13].

Binder hardness connecting diamond abrasive grains and binder material porosity is relevant in determining the wheel's capacity to grind. Porous grinding wheels demonstrated a greater capacity than conventional abrasives and are easier to balance and recondition. Grinding capacity increases if fine abrasive grains are used [14].

The structure of a complex model that allows predicting the output parameters of the grinding process (roughness, presence of defects and processing accuracy) was shown by Shipulin [15].

Chen et al. [16] studies roughness when specific areas (gears) are ground. Application and development of a highly efficient abrasive process were presented by Wang and Li [17].

The state of the art related to regression grinding models shows that general studies were conducted. More information is needed on the grinding of very hard material, specific application (such as the grinding of carbides for cutting tool manufacturing) and grinding without lubricant [16].

Based on previous research, this paper aims to determine surface roughness for the tungsten carbide gun drills (less frequently studied) in terms of different cutting conditions, using different grinding wheel grit and taking into account the grinding wheel wear.

There is a special case of sharpening small diameter deep hole drilling tools. In this case, grinding wheel wear increases considerably due to the existence of many surfaces and edges on the drilling

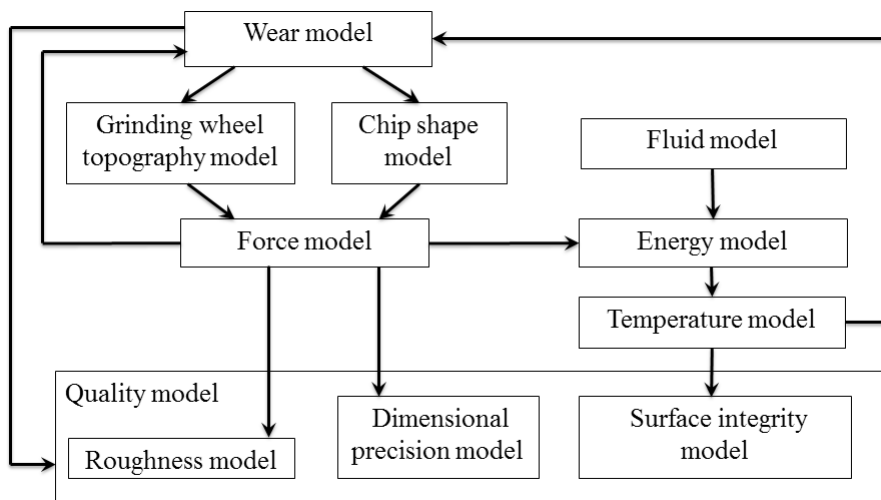


Fig. 1. Grinding kinematic models

tools. These surfaces and edges cause shocks when the cutting edges enter into the chips.

## 2 THE GRINDING MODEL

Grinding is a complex process influenced by many factors, a model of which is presented in Fig. 2.

First, the model establishes the framework in which the manufacturing process will take place. This refers to the work piece, machine tool, cutting tool, and coolant-lubrication.

The work piece material is characterised by size, shape, general mechanical proprieties, and the degree of elastic recovery after the tool crosses. The technological system refers to the machine tool and grinding wheel. The technical characteristics and manufacturing system stiffness are important to be known. The presence and nature of the coolant-lubrication fluid are also of great importance.

The input parameters are the cutting parameters. For grinding, these are feed, depth of cut, and speed. These values depend on the manufacturing material, imposed quality surface, etc.

The optimization of these parameters is the aim of most grinding studies. The grinding optimisation can be done only through the understanding of the physical processes that accompany the grinding. These are chip removal, cutting forces, vibrations, noise, consumed power in the cutting process, energy, the temperature of the wheel and of the manufactured

material, and grinding wheel wear. Most of these phenomena can be modelled kinematically, by the Finite Element method, and/or experimentally.

Grinding is a finishing operation. The most important output parameters are those that describe the surface quality.

The removal rate and the costs associated with the process are also important and must be taken into account. The study refers to the grinding process of the active surfaces of the gun drills made from tungsten carbide DK460U.

The tool life of cutting tools made of cemented carbide is greater when the active surface roughness is low. The machined surfaces are small and have varied geometries (active surfaces of the cutting tools). The production batch number is small. These issues make kinematic modelling more difficult. Therefore, we have chosen to conduct an experimental analysis concerning both grinding wheel wear and the roughness of the cemented carbide surfaces.

## 3 EXPERIMENTAL RESEARCHES

The present study is aimed at optimising the manufacturing parameters of DK460UF tungsten carbide, processed with diamond abrasive grinding wheels to obtain a high quality of the processed surface.

This material is a hard metal (or cemented carbide) with 91 % WC and 9 % Co, which is the

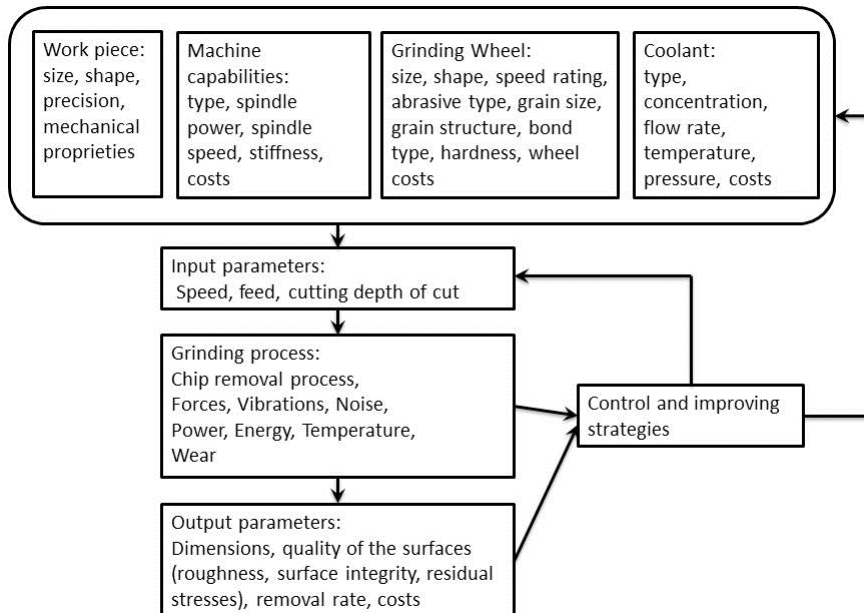


Fig. 2. Grinding model

main material currently used in cutting tool with solid cutting edges (drills, end mills, etc.). Some characteristics of this material are the grain size of  $0.5\ \mu\text{m}$  and the hardness of 1620 HV [18].

To do this, we carried out:

- an experimental analysis of tool wear (diamond grinding wheel);
- an experimental study of the roughness obtained by grinding under different cutting conditions using diamond abrasive grinding wheels that have various grit and wear degrees.

Previous research showed that the processing of these cemented carbides can be done with diamond abrasive wheels. In this study, diamond grinding wheels with  $46\ \mu\text{m}$  and  $54\ \mu\text{m}$  grit have been used (these are the most common grits used for processing hard metal cutting tools). The diameters of the grinding wheels are  $D = 180\ \text{mm}$  and  $D = 150\ \text{mm}$ , and the width  $10\ \text{mm}$ .

### 3.1 Experimental Research on Grinding Wheel Wear

The first study refers to grinding wheel wear. There are three distinct mechanisms relating to this wear: grain breaking, binder breakage and attrition of the grain. Wheel profile wear develops as a result of the friction between abrasive grains and the processed surface. As the worn area increases, the sliding forces increase and, therefore, will develop more heat, affecting the quality of the processed surface.

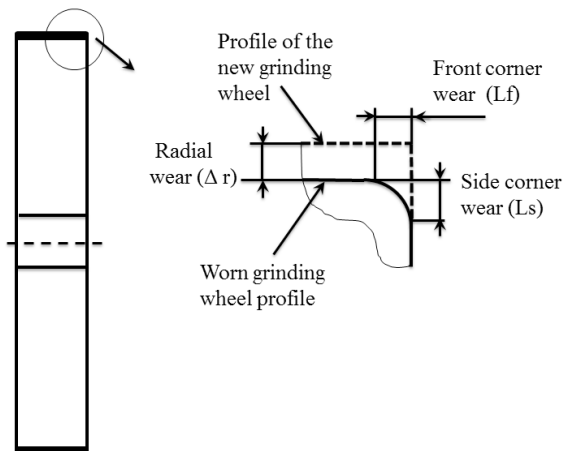


Fig. 3. Grinding wheel wear

The global wear of the grinding wheels is very important for this study and, therefore, we have used an experimental analysis in this case. The main parameters that estimate the grinding wheel wear are shown in Fig. 3:

- radial wear ( $\Delta r$ );
- side corner wear.

The grinding wheel wear was monitored in the process of sharpening the gun drills for small diameters (within the range  $2.025\ \text{mm}$  to  $2.5\ \text{mm}$ ).

Gun drills were sharpened on a Walter Helitronic Minipower Machine grinding tool, shown in Fig. 4. The cutting environment was an emulsion of water and 5 % oil Petrofer superfin at 1 MPa pressure (suitable for grinding high-quality surfaces with diamond grinding wheels).



Fig. 4. Helectronic mini power grinding machine



Fig. 5. Walter Helicheck Basic, optical CNC measuring machine

Every gun drill was processed on five different surfaces to obtain the active tool surfaces.

The grinding parameters were the following: depth of cut:  $0.01\ \text{mm}$ ; feed rate:  $0.005\ \text{mm/rev}$ ; and speed:  $55\ \text{m/s}$ .

The average depth of the removed layer on the active cutting surfaces is  $0.3\ \text{mm}$ . The average volume removed for a gun drill is  $1.02\ \text{mm}^3$ .

The grinding wheel wear was measured after processing each group of 100 work pieces. With a grinding wheel of  $46\ \mu\text{m}$  grit (D46 type), a total of 1058 gun drills were manufactured; 876 gun drills were processed with a grinding wheel type D54. After the sharpening of these gun drills, the corresponding

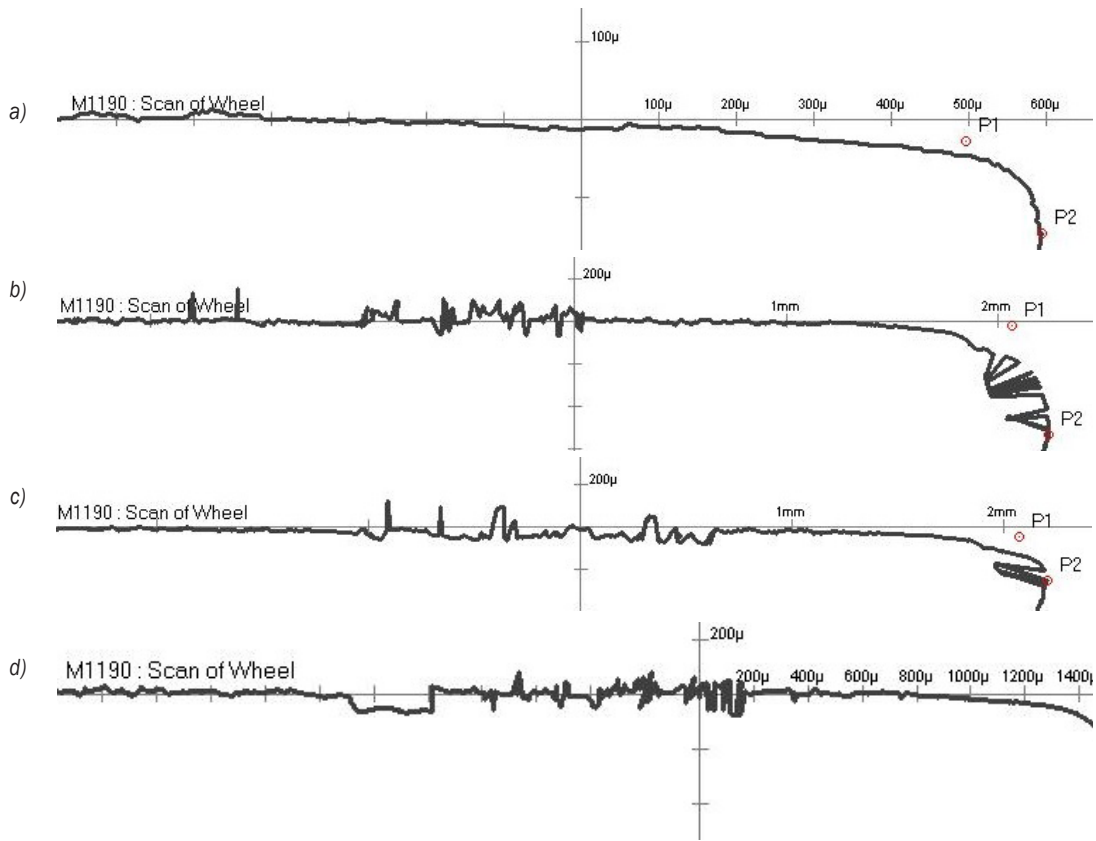


**Fig. 6.** Grinding wheel profiles with 54  $\mu\text{m}$  grit a) unused wheel; b); c) and d) grinding wheel after sharpening of 300, 600, 800 gun drills

**Table 1.** Grinding wheel wear in the sharpening process of gun drills

Number of sharpened gun drills	Material removed volume [mm <sup>3</sup> ]	Grinding wheel with grit of 46 $\mu\text{m}$		Grinding wheel with grit of 54 $\mu\text{m}$	
		radial wear [ $\mu\text{m}$ ]	edge wear [ $\mu\text{m}$ ]	radial wear [ $\mu\text{m}$ ]	edge wear [ $\mu\text{m}$ ]
0		0.00	0	0.00	0
100	102	5.24	27.04	7.75	32.56
200	204	8.30	43.16	11.50	43.52
300	306	16.34	115.23	21.75	92.53
400	408	28.56	167.81	32.20	138.56
500	510	43.12	224.57	48.80	227.82
600	612	54.76	281.32	64.20	337.86
700	714	68.05	351.71	90.30	469.63
800	816	79.37	408.73	115.00	587.79
900	918	93.17	482.52		
1100	1122	112.4	568.34		

grinding wheels reached the catastrophic wear. Catastrophic wear was considered for a radial wear of 0.1 mm.

The grinding wheel wear measurement was performed on a Walter Helicheck Basic Optical CNC measuring machine, shown in Fig. 5.

Fig. 6 presents the wear of the grinding wheel profile for a wheel of D 54 grit, after processing 0,

(the disc is new) 300, 600 and 800 work pieces. Radial wear was measured on the same Walter Helicheck Basic, Optical CNC measuring machine. Table 1 and Fig. 7 show the results of these measurements. By analysing wear curves, we observed that grinding wheels with greater grit wear out faster. Larger granules fracture and pull out more easily than smaller ones because granule density is lower, so the cutting

force is distributed on a smaller number of granules and the force to which granules are subjected is higher. In contrast, due to the size of the largest granules, a higher bending moment develops on each granule, leading to a more probable fracture and pulling out of the granule.

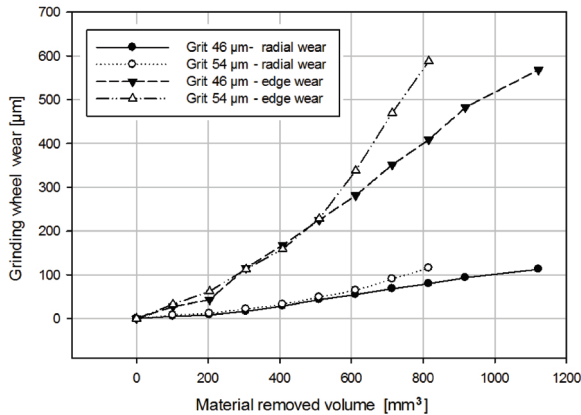


Fig. 7. Grinding wheel wear

An important parameter in the grinding process is the grinding ratio (*G-ratio*), which is simply a ratio comprising the volume of the work piece material removed and the volume of the grinding wheel expanded (volumetric wheel wear).

$$G - ratio = \frac{Material\ removed\ volume}{Volumetric\ wheel\ wear} \quad (1)$$

In the technical literature, there is some information about the *G-ratio* values. For the processing of ferrous materials, the *G-ratio* can vary from 20:1 to 80:1 [19]. In the experiments done by Izumi [20] on heavy grinding of large surfaces, the grinding ratio varied between 6.5 and 10. In difficult-to-grind materials operating under adverse conditions, the *G-ratio* may drop to 1 [21]. High grinding wheel performance is characterized by greater values of the *G-ratio*. Because of the small machined surfaces and numerous edges, one hypothesis for our experimental study is that the *G-ratio* values will be small.

Table 1 indicates the values of the volume of material removed. These have been computed starting from the average removed volume for one gun drill multiplied by the number of processed tools.

The removed volume for one gun drill has been computed with the relation:

$$V_{ri} = S_i \cdot A, \quad (2)$$

where  $V_{ri}$  is the removed volume for one gun drill,  $S_i$  the active surface processed for one gun drill, and  $A$  the average depth of the removed layer.

In our study, the average of the removed volume for one gun drill was 0.034 mm<sup>3</sup>.

Volumetric wheel wear is defined with the relation:

$$V_W = \pi \cdot D \cdot \Delta r \cdot B, \quad (3)$$

where  $V_W$  is the volumetric wheel wear,  $D$  grinding wheel diameter,  $\Delta r$  radial wear, and  $B$  grinding wheel width.

In our study, the size of the grinding wheel was  $D=150$  mm and  $B=10$  mm.

Table 2 and Fig. 8 show the grinding ratio in the grinding process using wheels with two grits.

The study shows that the *G-ratio* decreases as the grinding wheel wear increases. With worn grinding wheels, the number of cutting peaks decreases because part of the granule edges become blunt, some break and others are pulled apart. Because of clogged pores and damaged edges, the friction between the blank and the grinding wheel increases. Both these phenomena decrease the efficiency and the *G-ratio*.

In this study, *G-ratio* values are generally low, which shows that the processing of these cemented carbide tools (with many small surfaces) is more difficult than the grinding of large areas. The grinding wheel that processes small surfaces is subject to more input shocks than large surfaces. This causes a more pronounced wear.

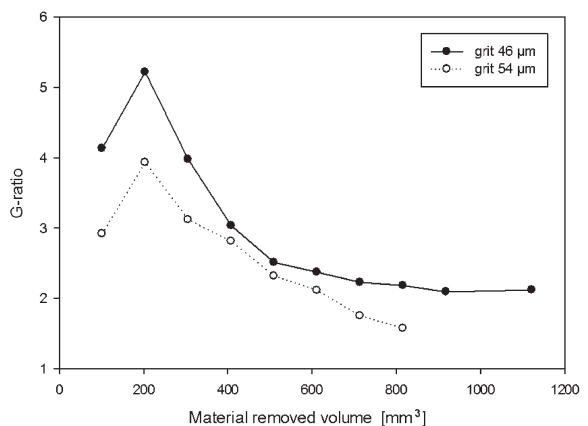


Fig. 8. *G-ratio*

Furthermore, it can be observed that the *G-ratio* is greater for lower grit values because grinding wheels with lower grit wear less than those with higher grit, as described before. That means that the process is more efficient. Therefore, from the point of view of

**Table 2.** Grinding ratio

Material removed volume [mm <sup>3</sup> ]	Grinding wheel with grit of 46 $\mu\text{m}$ - radial wear [ $\mu\text{m}$ ]	Grinding wheel with grit of 54 $\mu\text{m}$ - radial wear [ $\mu\text{m}$ ]	Volumetric wheel wear for grit of 46 $\mu\text{m}$ [mm <sup>3</sup> ]	Volumetric wheel wear for grit of 54 $\mu\text{m}$ [mm <sup>3</sup> ]	G-ratio for grit of 46 $\mu\text{m}$	G-ratio for grit of 54 $\mu\text{m}$
0	0.00	0.00	0	0		
102	5.24	7.75	24.68	34.96	4.13	2.91
204	8.30	11.50	39.09	51.86	5.21	3.93
306	16.34	21.75	76.96	84.56	3.97	3.12
408	28.56	32.20	134.52	122.67	3.03	2.81
510	43.12	48.80	203.09	188.51	2.51	2.70
612	54.76	64.20	257.91	289.54	2.37	2.11
714	68.05	90.30	320.51	407.25	2.22	1.75
816	79.37	115.00	373.83	518.65	2.18	1.57
918	93.17		438.83		2.09	
1122	112.4		529.40		2.11	

sustainability, grinding wheels with smaller grits are more desirable.

### 3.2 Experimental Study of Surface Roughness

Surface roughness, an indicator of surface quality, is one of the most specified requirements in machining parts. Surface roughness influences not only the dimensional accuracy of machined parts but also their properties.

Based on the theoretical research presented at the beginning of this paper, it was found that the main parameters that indirectly influence the roughness are the grinding wheel grit, feed rate, depth of cut, and grinding speed.

In order to analyse the influence of these parameters on roughness, the following experimental studies have been carried out:

- A 2<sup>4</sup> factorial experiment that has grinding wheel grit, speed, feed, and depth of cut as independent parameters when machining with a new disc;
- Using an optimal regime from the point of view of roughness, several samples have been manufactured with grinding wheels with the wear presented in Table 1. As a result, the influence of the grinding wheel wear on the roughness has been outlined.

#### 3.2.1 Experimental Study About the Influence of Grinding Wheel Grit, Speed, Feed, and Depth of Cut on the Surface Roughness

The main factors influencing the roughness are the grinding wheel grit, the depth of cut, the feed, and the speed. In this application, the influence on these four factors on the roughness of the ground surface

was investigated. The “design of experiments” methodology was used. The units and settings on the low and high levels of these factors are presented in Table 3. The experimenter measured the surface roughness (Table 4).

**Table 3.** The four varied factors

Name	Abbr.	Unit	Settings
depth of cut	$a_p$	[mm]	0.01 to 0.03
feed	$f$	[mm/rev]	0.005 to 0.008
speed	$v$	[m/s]	40 to 55
grit	<i>grit</i>	[ $\mu\text{m}$ ]	46 to 54

**Table 4.** The measured response parameters

Name	Abbr.	Unit
Roughness Ra	$R_a$	[ $\mu\text{m}$ ]
Roughness Rz	$R_z$	[ $\mu\text{m}$ ]

**Table 5.** The low and high level of the investigation parameters

Parameter	low	high
Grinding wheel grit	46 $\mu\text{m}$	56 $\mu\text{m}$
Depth of cut	0.01 mm	0.03 mm
Feed	0.05 mm/rev	0.08 mm/rev
Speed	40 m/s	55 m/s

The goal is to establish the values of the input factors that determine the minimum value for the response parameters (roughness).

The manufacturing process has been performed on DK460UF tungsten carbide rectangular blocks samples of 20 mm  $\times$  50 mm  $\times$  100 mm. The independent variables include grinding wheel grit, feed, depth of cut, and speed. The diamond grinding wheels were new (without wear). The grinding

**Table 6.** Roughness obtained by processing tungsten carbide DK460UF with diamond abrasive grinding wheels D46VB4P/A and D54VB4P/A

	Grinding wheel grit [ $\mu\text{m}$ ]	Depth of cut $a_p$ [mm]	Feed $f$ [mm/rev]	Speed $v$ [m/s]	Roughness $R_a$ [ $\mu\text{m}$ ]	Roughness $R_z$ [ $\mu\text{m}$ ]
1	46	0.03	0.005	40	0.126	0.504
2	46	0.03	0.005	55	0.113	0.452
3	46	0.03	0.008	40	0.142	0.568
4	46	0.03	0.008	55	0.132	0.532
5	46	0.01	0.005	40	0.063	0.290
6	46	0.01	0.005	55	0.057	0.228
7	46	0.01	0.008	40	0.084	0.328
8	46	0.01	0.008	55	0.077	0.316
9	54	0.03	0.005	40	0.139	0.572
10	54	0.03	0.005	55	0.128	0.512
11	54	0.03	0.008	40	0.156	0.645
12	54	0.03	0.008	55	0.150	0.597
13	54	0.01	0.005	40	0.072	0.342
14	54	0.01	0.005	55	0.065	0.276
15	54	0.01	0.008	40	0.095	0.381
16	54	0.01	0.008	55	0.087	0.362

process was done on a CNC machine tool Hawemat 3000, with high stiffness.

The roughness study has been performed on rectangular block samples of 20 mm × 50 mm × 100 mm made from the same material. The cutting environment was the same emulsion (Petrofer Superfin) used in the previous research. Surface roughness was measured with a Mitutoyo Roughness Meter.

The low and the high investigation level of the input parameters are presented in Table 5. The plan of the experiments is presented in Table 6. The first varied factor was the grinding wheel grit; the second was the depth of the cut, the third the feed and the fourth the speed.

The mathematical model (that can draw conclusions on the quality of the processed surface, depending on the grinding wheel grit and cutting regime) was obtained by using the Design Expert software. The linear polynomial regression has been chosen as the mathematical model.

The obtained relations for roughness are the following:

$$R_a = -0.0484 + 3.0375 \cdot a_p + 6.6667 \cdot f + 1.5313 \cdot 10^{-3} \cdot \text{grit} - 5.6667 \cdot 10^{-4} \cdot v, \quad (4)$$

$$R_z = -0.2179 + 11.98 \cdot a_p + 20.625 \cdot f + 8.047 \cdot 10^{-3} \cdot \text{grit} - 2.54 \cdot 10^{-3} \cdot v. \quad (5)$$

The adequacy of the roughness models has been based in the ANOVA analysis.

The “F value” is a test for comparing treatment variance with error variance. “Prob > F” is the probability of the observed “F<sub>value</sub>” if the null hypothesis is true. Generally, if “Prob > F” < 0.05, then the model is statistically significant. If “Prob > F” > 0.1, then the model is not significant.

In the  $R_a$  roughness model, the computed “F<sub>value</sub>” is 716.1. “Prob > F” of 0.00012 shows that the model is significant. There is only 0.01 % chance for the  $R_a$  value to be modified due to random noise.

**Table 7.** Testing the significance of roughness factors in the  $R_a$  model and  $R_z$  model

	$R_a$ model		$R_z$ model	
	F <sub>value</sub>	Prob > F*	F <sub>value</sub>	Prob > F*
Factor(depth of cut ap)	2451.10	0.00003 → significant	639.18	0.0002 → significant
Factor(feed f)	265.66	0.00005 → significant	42.62	0.00087 → significant
Factor (grit)	99.66	0.00007 → significant	46.13	0.000160 → significant
Factor (speed v)	47.98	0.000008 → significant	16.18	0.002 → significant

Similarly, the  $R_z$  roughness model is analysed. “Prob > F” is 0.00014 and shows that the  $R_z$  roughness model is also significant.

For the two roughness models, the significance of the factors was tested. The results are shown in Table 7.

The values of “Prob > F” that are less than 0.05 indicate that model factors are significant. Model factors are not significant if “Prob > F” values are greater than 0.1000.

After computing the model coefficients and after carrying out the factor analysis, it has been found that the depth-of-cut factor, feed factor, grit factor, and speed factor (in this order of importance) influence both surface roughness parameters.

Surface roughness values rise as the depth of cut increases. When the depth of cut is large the contact angle between the grinding wheel and blank increases. The granule number increases; the cutting forces and temperature are higher. The growth of the cutting forces determines higher variations of the force, of the depth of cut and vibration, which all increase roughness. Surface roughness can decrease if the depth of cut is reduced when using grinding wheels with small grains.

The feed is a very important parameter that influences surface roughness. When the feed increases, the distances between traces generated by the granules on the blank grow and cause an increase in roughness.

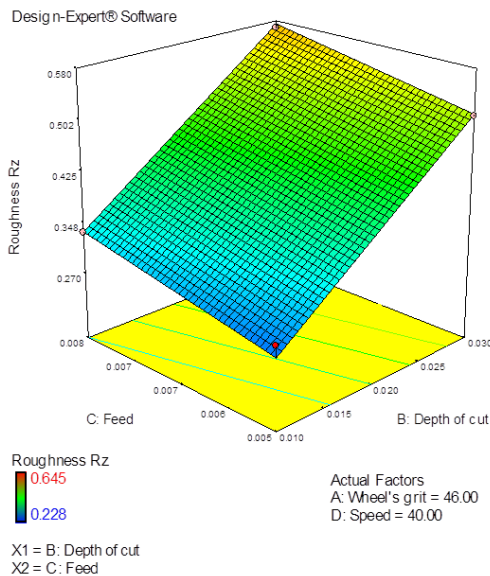


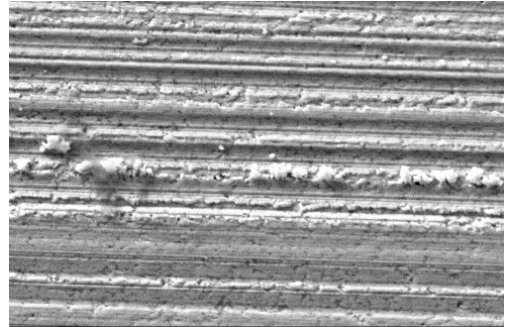
Fig. 9. Roughness  $R_z$  depending on feed and depth of cut

The grinding wheel grit has a significant influence on surface roughness. When the granules of

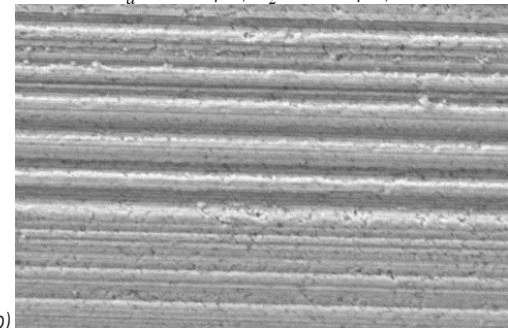
the grinding wheel are bigger, their traces are fewer and larger so that roughness increases.

Grinding speed has little effect. An increase in speed causes a small decrease in roughness because plastic deformation is easier.

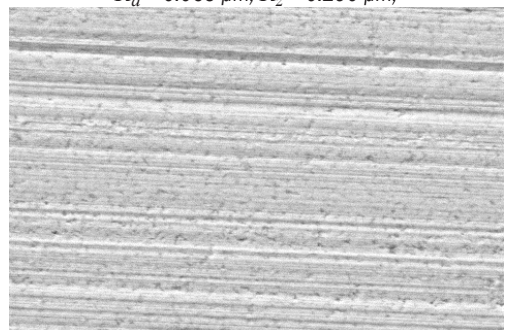
For a better visualization of the influence of feed and depth of cut on the surface roughness  $R_a$  and  $R_z$ , their variation curves have been plotted (Fig. 9).



a)  $a_p = 0.03 \text{ mm}$ ,  $f = 0.008 \text{ mm/rev}$ ,  $v = 40 \text{ m/s}$ ,  
 $R_a = 0.142 \text{ }\mu\text{m}$ ,  $R_z = 0.568 \text{ }\mu\text{m}$ ,



b)  $a_p = 0.01 \text{ mm}$ ,  $f = 0.005 \text{ mm/rev}$ ,  $v = 40 \text{ m/s}$ ,  
 $R_a = 0.063 \text{ }\mu\text{m}$ ,  $R_z = 0.290 \text{ }\mu\text{m}$ ;



c)  $a_p = 0.01 \text{ mm}$ ,  $f = 0.005 \text{ mm/rev}$ ,  $v = 55 \text{ m/s}$ ,  
 $R_a = 0.057 \text{ }\mu\text{m}$ ,  $R_z = 0.228 \text{ }\mu\text{m}$

Fig. 10. Grinding surfaces obtained by processing with a grinding wheel in good condition, with 46  $\mu\text{m}$  grit and with different cutting parameters

The ground samples were examined with the scanning electron microscope (SEM). The surface

images complete the information obtained by measuring the roughness. Some of them are shown in Fig. 10.

Roughness analysis and SEM observations of the machined surface have indicated that a surface with good roughness was achieved for cutting parameters,  $v = 55 \text{ m/s}$ ,  $f = 0.005 \text{ mm/rev}$ ,  $a_p = 0.01 \text{ mm}$ . Grit of  $46 \mu\text{m}$  is indicated to be used in order to obtain a maximum roughness of  $0.3 \mu\text{m}$ .

**3.2.2 The influences of Wheel Wear on Manufactured Surface Roughness**

Surface quality is also influenced by grinding wheel wear. To analyse the influence of grinding wheel wear on roughness, an optimum cutting set of parameters obtained in the case of unused grinding wheels has been considered. This consists of  $a_p = 0.015 \text{ mm}$ ,  $f = 0.005 \text{ mm / rev}$ , and  $v = 55 \text{ m/s}$ .

Processing was performed within this cutting regime with grinding wheels D46 and D54, with successive wears presented in Table 1 and in Fig. 7. It can be seen that the grinding wheel with greater grit wears out more quickly than the one with smaller grit and causes greater roughness of the manufacturing surfaces (Table 8 and Fig. 11). Wear changes the grinding wheels cutting geometry. Granule edges become blunt, some granules break, and pores become clogged. These phenomena cause increased friction, which decreases roughness. Furthermore, because grinding wheels are sharpening various surfaces of complex shapes, the disc loses its cylindricity, which also causes the roughness to increase.

The samples processed by worn grinding wheels were also examined by scanning electron microscope. Fig. 12 shows the some images of the samples

processed with grinding wheels with various wear forms. SEM observations indicate that the surfaces' roughness is improper. Each wear form causes major defects on the processed surfaces.

For the previously established optimum cutting parameters, a grinding wheel with maxim grit of  $46 \mu\text{m}$  can be used to obtain a maximum roughness of  $R_z = 0.3 \mu\text{m}$ . For this grit, the maximum allowed radial wear  $\Delta r$  is  $30 \mu\text{m}$ .

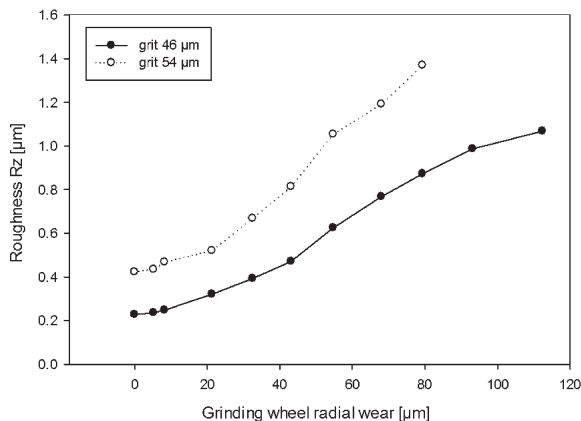


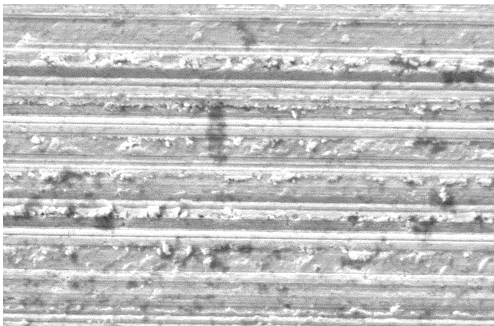
**Fig. 11.** Roughness obtained by processing with grinding wheel having different levels of wear

**4 CONCLUSIONS**

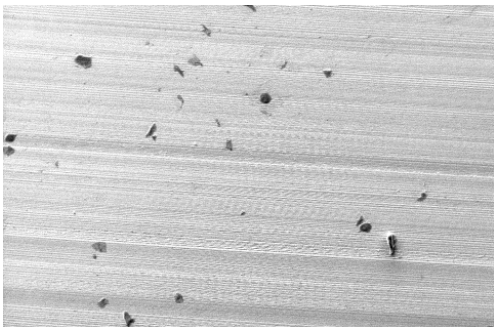
The optimization of the grinding process of tungsten carbides used for cutting tools is important because their active surfaces require certain quality characteristics. The higher surface quality of cemented carbide tools lead to easier chip removal and hence the tool life is greater. The maximum allowable active surface roughness is  $R_z = 0.3 \mu\text{m}$ .

**Table 8.** Roughness depending on grinding wheel wear (manufacturing parameters:  $a_p = 0.015 \text{ mm}$ ,  $f = 0.005 \text{ mm/rev}$ ,  $v = 55 \text{ m/s}$ )

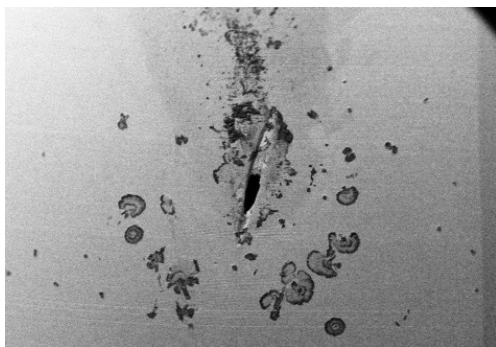
Number of sharpened gun drills	Grinding wheel with grit of $46 \mu\text{m}$		Grinding wheel with grit of $54 \mu\text{m}$	
	Radial wear [µm]	Roughness $R_z$ [µm]	Radial wear [µm]	Roughness $R_z$ [µm]
0	0.00	0.228	0.00	0.423
100	5.24	0.236	7.75	0.435
200	8.30	0.248	11.50	0.468
300	16.34	0.321	21.75	0.520
400	28.56	0.393	32.20	0.668
500	43.12	0.471	48.80	0.814
600	54.76	0.625	64.20	1.054
700	68.05	0.768	90.30	1.192
800	79.37	0.873	115.00	1.370
900	93.17	0.987	-	-
1100	112.4	1.068	-	-



a) Grinding wheel D46VB4P/A with the grit of  $46\ \mu\text{m}$ , worn profile of grinding wheel,  $\Delta r = 34.75\ \mu\text{m}$ ,  $a_p = 0.03\ \text{mm}$ ,  $f = 0.008\ \text{mm/rev}$ ,  $v = 55\ \text{m/s}$ , roughness  $R_z = 1.192\ \mu\text{m}$ . Radial wear of the grinding wheel causes high roughness of the processed surface



b) Grinding wheel D46VB4P/A with the grit of  $46\ \mu\text{m}$ , clogged grinding wheel,  $a_p = 0.01\ \text{mm}$ ,  $f = 0.005\ \text{mm/rev}$ ,  $v = 40\ \text{m/s}$ , roughness  $R_z = 0.972\ \mu\text{m}$ ; the clogging of the grinding wheel causes adhesion of the removed material particles to the machined surface



c) Grinding wheel D54VB4P/A with the grit of  $54\ \mu\text{m}$ , blunt grains,  $a_p = 0.03\ \text{mm}$ ,  $f = 0.008\ \text{mm/rev}$ ,  $v = 55\ \text{m/s}$ , roughness  $R_z = 0.768\ \mu\text{m}$ ; due to the grinding wheel wear, the friction between the work piece surface and the active surface of the grinding wheel is intense, which causes an increasing temperature in the contact area; the layer beneath the machined surface shows changes (oxidation burns)

**Fig. 12.** Grinding surfaces obtained by processing with worn grinding wheels

When sharpening carbide tools, the grinding surfaces are very small and show various geometries

with multiple edges (edges of the active surfaces and of the fluid-cutting channel). For this reason, the grinding wheel is subjected to shocks penetrating that cause accelerated wear the material. The high hardness of carbides also causes accelerated wear of the disc.

The performance of the grinding process is assessed by means of the values of the G-ratio, for which it is better to have high values. There are common values of the G-ratio of 20:1 for the processing ferrous materials. By processing DK460UF tungsten carbide tools with small diameters, we obtained low values of the G-ratio between 2:1 and 5:1. It was noted that the value of the G-ratio depends on the grit of the grinding wheel and on its wearing. For the lower wheel grit (D46), a higher G-ratio is obtained. The grinding wheel wear causes a decrease in the G-ratio.

In the second part of the research, the aim was to identify the optimal values of cutting parameters that lead to the achievement of the active surface roughness required for carbide tools.

The results of the experiments allow us to obtain the optimal parameters for the grinding process from the point of view of surface quality. The optimal parameters resulting from the experimental research of the grinding process were the following: depth of cut  $a_p = 0.01\ \text{mm}$ , feed  $f = 0.005\ \text{mm/rev}$ , cutting speed  $v = 55\ \text{m/s}$ , grit of grinding wheel =  $46\ \mu\text{m}$ . Under these conditions, the value of the  $R_z$  surface roughness was  $0.228\ \mu\text{m}$ .

The study of the roughness variation in relation to the radial wear of the grinding wheel shows that the imposed roughness  $R_z = 0.3\ \mu\text{m}$  can be achieved only by processing with grinding wheels that have the grit smaller than  $46\ \mu\text{m}$ . In this case, for a D46 grinding wheel, the maximum allowed radial wear  $\Delta r$  is  $30\ \mu\text{m}$ .

## 5 ACKNOWLEDGMENT

This research was carried out under the project POSDRU/CPP107/DMI1.5/S/76851, partly financed from the European Social Fund, within the Sectorial Operational Program Human Resource Development 2007–2013 - Romania.

## 6 REFERENCES

- [1] Shaw, C.M. (1996). *Principles of Abrasive Processing*. Clarendon Press, Oxford.
- [2] Brinksmeier, J.C., Aurich, J.C., Govekar, E., Heinzl, C., Hoffmeister, H.-W., Klocke, F., Peters, J., Rentsch, R., Stephenson, D.J., Uhlmann, E., Weinert, K., Wittmann, M.

- (2006). Advances in modelling and simulation of grinding processes. *Annals of the CIRP*, vol. 55, no. 2, p. 667-696, DOI:10.1016/j.cirp.2006.10.003.
- [3] Law, S.-S., Wu, S.-M. (1973). Simulation Study of the Grinding Process. *Transactions of the ASME, Journal of Engineering for Industry*, 95, no. 4, p. 972-978, DOI:10.1115/1.3438277.
- [4] Chen, X., Rowe, W.-B. (1996) Analysis and simulation of the grinding process generation of the grinding wheel surface. *International Journal of Machine Tools and Manufacture*, vol. 36, no. 8, p. 871-882, DOI:10.1016/0890-6955(96)00116-2.
- [5] Gong, Y. D., Wang, B., Wang, W. S. (2002). The simulation of grinding wheels and ground surface roughness based on virtual reality technology. *Journal of Materials Processing Technology*, vol. 129, no. 1-3, p. 123-126, DOI:10.1016/S0924-136(02)00589-7.
- [6] Inasaki, I. (1996). Grinding Process Simulation based on the Wheel Topography Measurement, *Annals of the CIRP*, vol. 45, no. 1, p. 347-350, DOI:10.1016/S0007-8506(07)63077-7.
- [7] Koshy, P., Ives, L.-K., Jahanmir, S. (1999). Simulation of diamond-ground surface. *International Journal of Machine Tools and Manufacture*, vol. 39, no. 9, p. 1451-1470, DOI:10.1016/S0890-6955(99)00002-4.
- [8] Zhou, X., Xi, F. (2002). Modelling and predicting surface roughness of the grinding process. *International Journal of Machine Tools and Manufacture*, vol. 42, no. 8, p. 969-977, DOI:10.1016/S0890-6955(02)00011-1.
- [9] Krar, S.F., Ratterman, E. (1990). *Superabrasives: Grinding and Machining with CBN and Diamond*. McGraw-Hill, New York.
- [10] Yin, L., Spowage, A.C., Ramesh, K., Huang, H., Pickering, J.P., Vancoille, E.Y.J. (2004). Influence of microstructure on ultraprecision grinding of cemented carbides. *International Journal of Machine Tools & Manufacture*, vol. 44, no. 5, p. 533-543, DOI:10.1016/j.ijmachtools.2003.10.022.
- [11] Borkowski, J., Borkowski, P. (2002). The Influence of Elementary Effects on Grinding Wheel Wear. *Archives of Civil and Mechanical Engineering*, vol. II, no. 1-2, p. 21-34.
- [12] Luo, S.Y., Liao, Y.S., Chou, C.C., Chen, J.P. (1997). Analysis of the wear of a resin-bonded diamond wheel in the grinding of tungsten carbide. *Journal of Materials Processing Technology*, vol. 69, no. 1-3, p. 289-296, DOI:10.1016/S0924-0136(97)00032-0.
- [13] Liu, K., Li, X.P., Rahman, M. (2003). Characteristics of High Speed Micro-cutting of Tungsten Carbide. *Journal of Materials Processing Technology*, vol. 140, no. 1-3, p. 352-357, DOI:10.1016/S0924-0136(03)00758-1.
- [14] Zelwer, O., Malkin, S. (2008). Grinding of WC-Co cemented carbides. *Industrial Diamond Review*, no. 4, p. 65-69.
- [15] Shipulin, L.V. (2012). Complex model of surface grinding. *Proceedings of the International Multi-Conference of Engineers and Computers Scientists*, vol. II, from: [http://www.iaeng.org/publication/IMECS2012/IMECS2012\\_pp1325-1327.pdf](http://www.iaeng.org/publication/IMECS2012/IMECS2012_pp1325-1327.pdf), accessed on 2013-05-10.
- [16] Chen, H.F., Tang, J.Y., Zhou W. (2013). Modelling and predicting of surface roughness for generating grinding gear. *Journal of Materials Processing Technology*, vol. 213, no. 5, p. 717-721, DOI:10.1016/j.jmatprotec.2012.11.017.
- [17] Wang, S., Li, C.H. (2012). Application and development of high-efficiency abrasive process. *International Journal of Advanced Science and Technology*, vol. 47, p. 51-64.
- [18] Sadiq, M.I. (2013). *An Introduction to Cutting Tools Material and Applications*. Elanders Press, Mölnlycke.
- [19] Mc Spadden, S., Hughe, S., (1998). A Systematic Method for Grinding Wheel Performance Evaluation, from <http://web.ornl.gov/~webworks/cpr/y2001/pres/116758.pdf>, accessed on 2015-04-5.
- [20] Izumi, M., Ochi, A., (2004). *Sizing Method Based on Grinding Ratio in Heavy Grinding*. American Society for Precision Engineering, from [http://www.aspe.net/publications/Annual\\_2004/POSTERS/5PROC/1GRIND/1573.PDF](http://www.aspe.net/publications/Annual_2004/POSTERS/5PROC/1GRIND/1573.PDF), accessed on 2015-04-05.
- [21] Marinescu, I.D., Hitchiner, M., Uhlmann, E., Rowe B., Inasaki, I., (2006). *Handbook of Machining with Grinding Wheels*. CRC Press, Boca Raton, DOI:10.1201/9781420017649.

# Simulation of an Excavator Hydraulic System Using Nonlinear Mathematical Models

Paolo Casoli\* – Nicola Pompini – Luca Riccò

University of Parma Italy, Industrial Engineering Department, Italy

*This paper describes a mathematical modelling methodology developed for the rapid simulation of an excavator hydraulic system. The modelling approach presented enables a reduction of the control system development time for a complete excavator, while providing accurate system dynamics. A tool for defining an appropriate control strategy is a key point for satisfying the need for systems with better energy-efficiency. Moreover, the model will be a significant support in investigating energy recovery solutions and evaluating the suitability of hybrid solutions (mechanical/hydraulic/electric). The hydraulic model, composed of the pump's grey box model and the valve block white box model, has been validated on the basis of a set of experimental data collected on a test bench. The results of this study are presented in this paper.*

**Keywords:** hydraulic excavator, hydraulic system nonlinear modelling, variable displacement pump, load sensing, flow-sharing valve

## Highlights

- The model of the hydraulic circuit could be used for control-oriented applications.
- The mathematical model is based on grey and white box models.
- Experimental validation of the pump model in both steady and dynamic conditions.
- Experimental and numerical analysis of the pump-valve system interactions.

## 0 INTRODUCTION

There is an increasing demand in the field of construction equipment to simultaneously develop both a construction equipment system and a control strategy, especially when a short commissioning period is desired. Moreover, the manufacturer's engineering teams must satisfy the needs of operators in different geographical locations. Therefore, there is a need for a powerful software development tool, able to reproduce the behaviour of complex mechanical systems, such as large manipulators, mobile cranes and excavators, in transient conditions and with low calculation times, with the ultimate aim of realizing a "control-oriented" model able to perform real time simulations in a hardware in the loop (HiL) or software in the loop (SiL) environment. This approach can lead to great time savings, as it allows testing and debugging the control unit simultaneously with the development of the actual physical system to be controlled. In contrast, the development of a reliable multi-system model can be a valuable instrument in performing full system optimization, given the ability to simulate the interaction between various components (hydraulics, engine, and kinematics) under actual operating conditions. The ultimate aim of this research is to realize a customized control strategy, able to guarantee performance improvements (e.g. fuel consumption reduction) for the specific application. The complexity in modelling these

systems is attributed to the inherently nonlinear hydraulic drive used to achieve precise motion and power control.

The hydraulic systems are characterized by a superior power density in comparison with electrical or mechanical systems, but hydraulic systems are less efficient due to the energy conversions involved. In order to reduce the energy losses, new system layouts are proposed [1] to [3], but typically the systems are designed for satisfying the load requirements controlling the fluid flow generated by the pumps. Variable displacement pumps are essential for controlling the flow; in axial piston pumps, the displacement can be varied by tilting the swash plate, which can be achieved fast enough to meet the dynamic demands due to multiple loads. The swash plate angular position is controlled by means of an actuator working in feedback with the load; these types of pumps are known as load-sensing pumps. The load signals from the actuators are transferred to the pump regulators through the load-sensing line. A load-sensing, flow-sharing valve block was used for the application considered; flow sharing is a useful feature when the global flow rate required by the various elements exceeds the pump's maximum flow rate, especially in excavators where several simultaneous motions are required.

A literature review shows that pump models could be conceived in a number of ways, either for analysing specific aspects in greater detail [4] to [6], or,

on the basis of linear transfer functions, reproducing the pump's dynamic behaviour [7]. The first approach was clearly discarded, as the aim was to create a model suitable for reproducing pump behaviour, not a tool for pump design, while the second approach lacks the flexibility required to examine pumps in different working conditions, as the transfer functions would have to be modified each time. In this research, a grey box modelling approach has been followed, which represents a satisfactory compromise between the very short run time and the accuracy of results [8]. The following sections describe the modelling of the pump, the flow-sharing valve and the excavator kinematics; the validated results of the pump and valve models are also presented.

## 1 PHYSICAL MODELING

### 1.1 Pump and Compensators Model

The pump model described in this paper is that of a variable displacement axial piston pump. The pump is controlled by using two compensators: the pressure compensator (PC), which acts as a relief valve, limiting the maximum pressure of the system, and the flow compensator (FC), which modulates the outlet flow in order to obtain a specific pressure difference between the pump outlet and the load-sensing line. The pump model presented in this paper is an improvement on the grey box model developed by the authors and reported in [8]. The grey box model includes a white box model of the flow and pressure compensators, and a black box model of the pump flow characteristics. Significant improvements on the pump black box model are presented in this paper; specifically, a more detailed stationary correlation between the pump swash plate actuator pressure and pump delivery pressure, swash plate position and pump shaft rotary speed is obtained. Moreover, the calibration of the viscous friction coefficient (Eq. (3)), which greatly affects the swash plate dynamic, was carried out on the basis of experimental dynamic tests. The mathematical models were developed using the AMESim® simulation software.

#### 1.1.1 Pressure and Flow Compensator Model

The compensators were previously modelled and verified in detail [8]. The pressure and flow compensator models are based on a fluid-dynamic model (FDM) and a mechanical-geometrical model (MGM). The FDM calculates the pressures inside the chambers and the flow rate between adjacent

chambers, while the MGM calculates the forces acting on the spool and determines its position and the corresponding flow areas. The FDM and the MGM are both based on a lumped parameter framework. The pressure inside each control volume is assumed to be spatially uniform and time dependent; a pressure-rise rate in Eq. (1) is obtained from the continuity equation and the state equation of the fluid:

$$\frac{dp_i}{dt} = \frac{\beta}{\rho_i} \frac{1}{V_i(x)} \left( \sum \dot{m} - \rho_i \frac{dV_i(x)}{dt} \right), \quad (1)$$

where the volume of the chamber is derived from the instantaneous position of the spool ( $x$ ). The model assumes a constant value of fluid temperature. The fluid density is evaluated as a function of pressure as described in [9] and [10]. The summation term represents the net mass flow rate entering or leaving the volume. This is obtained by considering the contribution of all orifices connected with the volume considered. The mass exchange occurring through the orifices is calculated using Bernoulli's generalized equation under quasi-steady conditions [8] and [9]. The forces acting on the spool are hydrostatic forces, the spring forces, friction forces, and hydrodynamic forces. The hydrodynamic forces have been neglected. The model employed is a slightly simplified version of an already verified one [8], in which redundant chambers and leakages (which have been proved to have a very low impact on the accuracy of simulation results) were removed in order to reduce the computation time. The corresponding increase in the volume of the remaining chambers also had a positive effect. Eq. (1) shows that hydraulic components have a considerably small time constant since mineral oils have a high bulk modulus  $\beta$  ( $\sim 1700$  MPa); therefore, even small flow rates induce high variations in the chamber pressure. The increase in chambers volume, therefore, leads to less stiff behaviours.

#### 1.1.2 Flow Characteristics Model of the Pump

The basic idea of the model is to consider the pump as a simple flow generator whose output is a function of both the given rotary speed (usually a constant value set in the range of 750 r/min to 2300 r/min) and the instantaneous displacement geometrically related to the swash plate angular position.

$$\dot{V}_{th} = V_d(\alpha) \cdot n. \quad (2)$$

The flow characteristic of the pump, therefore, is closely correlated to the equilibrium of the swash plate expressed through Newton's second law.

$$J_{EQ}\ddot{\alpha} + c\dot{\alpha} = \sum_{n=1}^N T_n + T_{ACT} \quad (3)$$

The viscous friction coefficient was set on the basis of dynamic experimental tests, as reported in Section 3. While the control actuator torque was successfully evaluated by developing a white box model of the compensators, the determination of the barrel torque proved to be quite elaborate, requiring the identification of a great number of parameters (such as the determination of pressure in each pumping piston, damping effects, the length and diameter of the pistons masses, valve plate geometry, etc.). Therefore a black box model was preferred to determine the barrel torque, in order to provide a fast but still reliable model of the system. This was achieved by measuring the pressure in the pump swash plate actuator chamber (proportional to the control actuator torque) at given values of pump delivery pressure ( $p_D$ ), swash plate angular position, and at different rotary speeds.

At steady-state conditions, being  $\dot{\alpha} \cong 0$ , Eq. (3) guarantees the equivalence:  $\sum_{n=1}^N T_n = T_{ACT}$ . Thus, given the area of control actuator piston and the arm of the actuating force, a correlation between the pump actuator pressure and barrel torque exists (Eq. 4):

$$\sum_{n=1}^N T_n = p_{ACT}(p_D, \alpha, n) \cdot A_{ACT} \cdot d_{ACT} \quad (4)$$

Through a surface fitting tool, a correlation was provided between the pressure in the pump actuator chamber and both the swash plate angular position and the pump outlet pressure, for a given set of pump shaft rotary speeds between 850 r/min to 2250 r/min (Fig. 1). The influence of the shaft rotary speed is the main improvement from the work presented in [8].

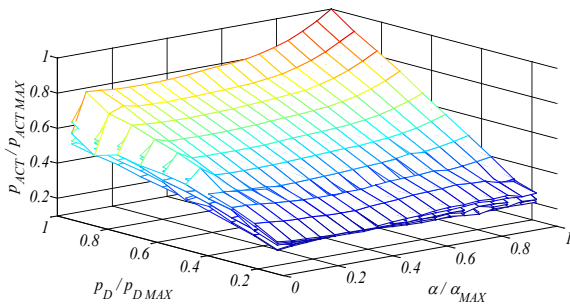


Fig. 1. Actuator pressure,  $p_{ACT} = f(p_D, \alpha, n)$

A suitable experimental activity was carried out to improve the model's accuracy in calculating the swash plate actuator pressure when the pump shaft rotary

speed varies. Fig. 2 shows a comparison between the experimental data and the simulation results. For confidential reasons, a more detailed explanation of the experimental setup cannot be provided here. It can, however, be observed that the new model actuator pressure presents a much better match with the experimental results if compared to the original model during pump speed variations.

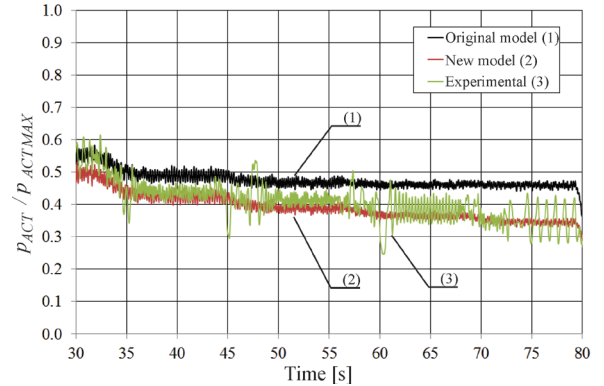


Fig. 2. Original and new pump model - actuator pressure comparison with experimental data

Hydraulic-mechanical and volumetric efficiencies were experimentally determined according to the ISO 4409:1986 standard [11]. Overall efficiency is reported in Fig. 3 at the maximum pump displacement values.

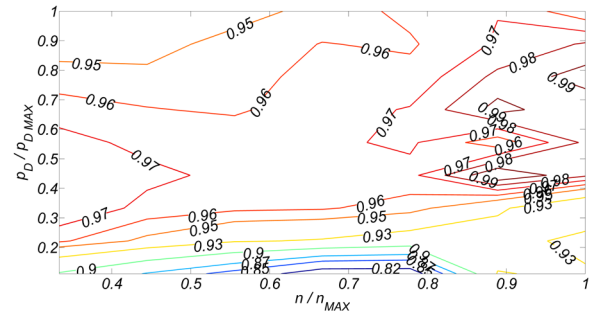


Fig. 3. Pump normalized overall efficiency,  $\eta_g/\eta_{gMAX}$  at  $\alpha/\alpha_{MAX} = 1$

The real flow outlet is thereby calculated as:

$$\dot{V} = \eta_v(p_D, \alpha, n) \cdot \dot{V}_{th} \quad (5)$$

while the torque required at the motor shaft is:

$$T = \frac{\Delta p \cdot V_d(\alpha)}{2\pi} \cdot \frac{1}{\eta_{hm}(p_D, \alpha, n)} \quad (6)$$

## 1.2 Directional Valve Model

The excavator under study is equipped with a load-sensing full flow-sharing valve block (Walvoil® DPX),

which is very effective for this kind of application. During a digging cycle, at least three valve sections are generally used at the same time, which could lead to the pump working in flow saturation conditions, i.e. the pump maximum flow is less than the flow required by the system. The operator might lose the direct control of the moving parts if this situation occurs in machinery in which a standard load-sensing (LS) circuit is adopted. A flow-sharing valve prevents this happening by evenly decreasing the flow to all the moving parts, thus maintaining the controllability of movements at the expense of a reduced velocity. The valve block is composed of multiple sections, each of which defines the outlet flow toward a specific actuator, extrapolates the LS pressure, maintains a constant pressure drop across the main spool metering area and provides the flow-sharing operation condition if required. A simple mathematical model cannot recreate all these functioning conditions. Therefore, the valve mathematical model was developed as a simplified valve model able to recreate the actual working conditions of the valve. Figure 4 shows the ISO scheme of a valve section.

The valve white box model has already been developed and validated [12], with a comparison between simulation and experimental results obtained in laboratory tests. The model is based on the same equations used for the pump flow compensator (section 2.1.1). The hydrodynamic forces acting on the spools were neglected, because the model was not conceived for design purposes, but as a tool for reproducing valve dynamic behaviours guaranteeing short simulation times.

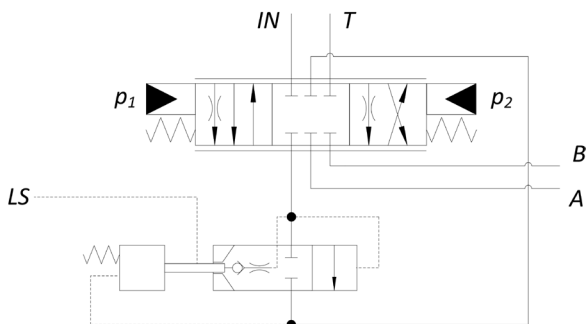


Fig. 4. Directional Flow Control Valve ISO scheme

### 1.3 Kinematics and Actuators Model

This section describes the modelling of the excavator's front tool kinematics, which was modelled to recreate the realistic forces acting on the hydraulic actuators during the movements. The kinematic model was

coupled with the hydraulic model using the Planar Mechanics library of AMESim® [13]. The excavation tool is composed of a boom, arm and bucket that are moved by means of hydraulic actuators. The kinematics were implemented as a lumped parameter model [8], [14] and [15]. The model is not yet intended to simulate the forces acting on the bucket during its interaction with the soil [16]. The kinematics model calculates the dynamic loads on the hydraulic cylinders as well as the instantaneous positions and the velocities of piston actuators. The hydraulic actuator model includes pressure dynamic calculation, according to Eq. (1), in the volumes at each side of the piston. Eq. (2) defines the mass flow rate in the volumes, also taking into account the leakages between the chambers.

The friction forces acting on the cylinder piston are derived from viscous and Coulomb friction in agreement with other research [17]. Due to the model causality, the viscous friction is only considered in the hydraulic actuator model.

## 2 EXPERIMENTAL SETUP

### 2.1 Experimental Setup and Tests on the Pump

Fig. 5 depicts the test rig ISO scheme used to analyse the pump's dynamic behaviour and estimate the viscous friction parameter  $c$  (Eq. (3)). Table 1 reports the instrumentation used for the tests. The test bench is also equipped with an off-line circuit for oil temperature control, consisting of a heat exchanger system that is electronically regulated to maintain a specified working temperature (50 °C). The pump was equipped with an angular sensor directly connected to the swash plate, where a torque limiter is typically mounted. A proportional flow control valve (A) was inserted on the pump outlet line to regulate the outgoing flow rate; a proportional relief valve (B) was inserted to maintain the system pressure at a desired set-point.

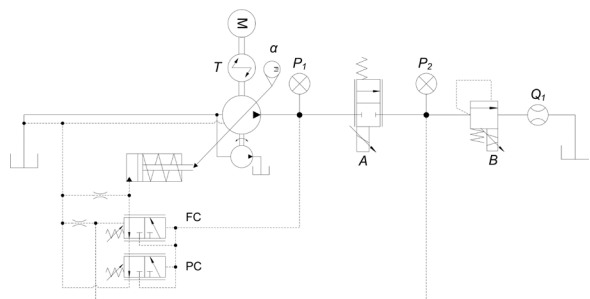


Fig. 5. Experimental setup for pump testing

The phenomenon of interest, i.e. the pump swash plate variation derived from the pressure difference induced by the opening variations of the control valve (A) was estimated as lower than 50 Hz, due to preliminary step response tests. According to the Nyquist-Shannon sampling theorem, a sample rate frequency of 200 Hz was chosen to avoid aliasing errors.

**Table 1.** Features of sensors and main elements of the experimental apparatus used in the present research

Sensor	Type	Main features
M	Electric Motor	ABB®, 4-quadrant electric motor, 75 kW
P	Pump	variable displacement axial piston pump, 84 cm <sup>3</sup> /r
P <sub>1</sub> to P <sub>8</sub>	Strain gage	Trafag®, Scale 0 to 40 MPa, 0.3 % FS accuracy
Q <sub>1</sub> to Q <sub>2</sub>	Flow meter	VSE® VS1, Scale 0.05 to 80 l/min, 0.3 % measured value accuracy
T	Torque meter	HBM® T, Scale: 0 to 500 Nm, 0.05 Accuracy Class
LVDT	Linear variable differential transformer	Magnet Schutz AWAX 015A01

**2.1.1 Testing Conditions**

The tests were carried out with the LS pressure kept constant by using the proportional relief valve (B). A swash plate position ( $\alpha$ ) dynamic transient was induced by a step variation of the servo proportional flow control valve (A) area. A typical transient behaviour of the pump swash plate on a flow step demand is reported in Fig. 6, while Fig. 7 shows the correspondent dynamic variation of LS and delivery pressure.

**2.2 Experimental Test Setup: Valve Block and Pump**

A suitable experimental setup was provided to test the functioning of the valve block and pump system. The hydraulic circuit ISO scheme is represented in Fig. 11. The tests were carried out by using the valve block, composed of two valve sections, coupled with the variable displacement axial piston pump, with a connection between pump FC and valve LS line. The pump was equipped with an angular sensor directly connected with the swash plate, as previously explained.

Fig. 8 illustrates the cross-section of each valve section along with the pressure-mapping points; the two linear variable differential transformers (LVDT) are connected to the main spool and the pressure

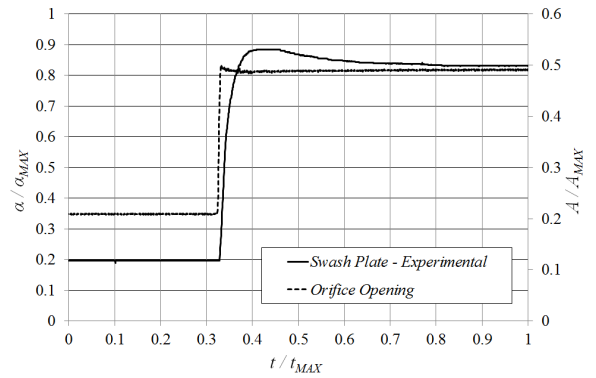


**Fig. 6.** Pump swash plate dynamic response to a step variation of the required flow rate

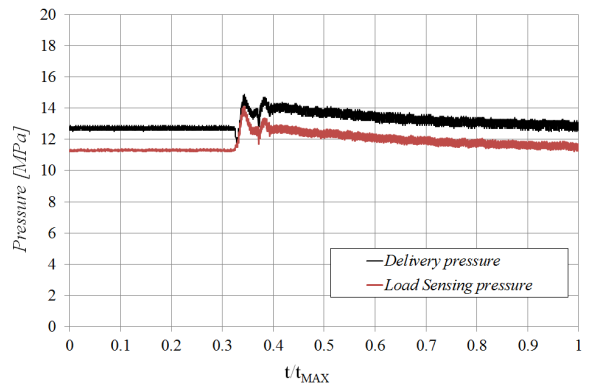


**Fig. 7.** Delivery pressure response to a step variation of the required flow rate

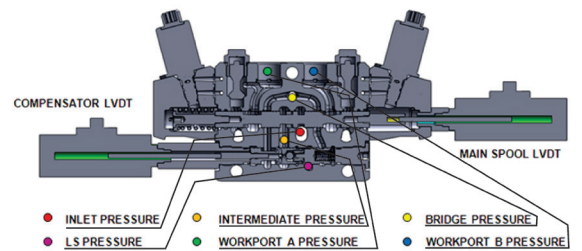


**Fig. 8.** Valve with installed LVDT and pressure mapping points

compensator spool. As shown in Fig. 11, two test bench lines were used to recreate the load on the two valves' outlet section. The lines are equipped with a flow meter and a proportional relief valve. A bleed valve was installed on the load-sensing line to maintain the line drained. The system was tested under standard working conditions, i.e. no flow saturation. The inputs of the experimental test were recorded and used as inputs for the simulation. The pump margin pressure was set at 2 MPa, i.e. pump delivery pressure was to be 2 MPa above the load-sensing pressure. The pump shaft rotary was set at a constant value of

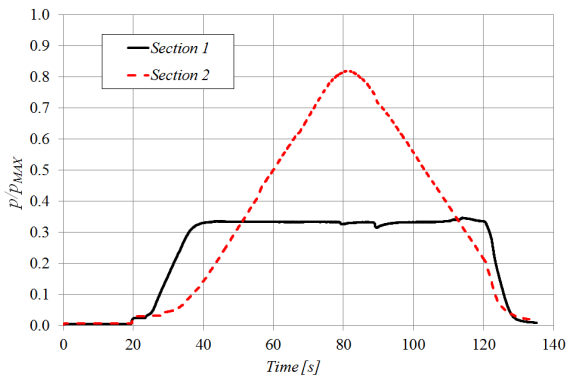


Fig. 9. Imposed loads to the valve sections

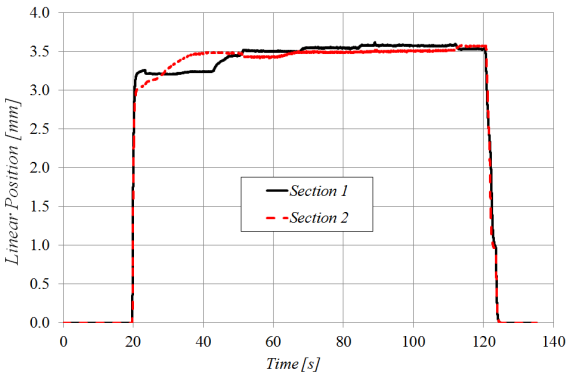


Fig. 10. Valve's main spools displacement

1500 r/min. Fig. 9 illustrates the loads imposed on the valve sections by means of the test bench proportional relief valves. Fig. 10 shows each section's main spool

position, imposed on the valves and acquired through the LVDTs. The double pressure compensation cycle, whose valve users pressures and main spools opening are reported in Figs. 9 and 10 respectively, is very useful to verify the valve's compensators behaviour, as the role of the main section (i.e. the one which provides the load-sensing signal) was switched during the simulation; this also means that the intermediate pressure inside the compensated section (i.e. the one connected to the minor load) had to be modulated by the compensator in order to maintain the desired pressure drop across the metering area. This testing condition provides realistic boundary conditions, useful for testing the valve's behaviour.

### 3 COMPARISON OF EXPERIMENTAL AND SIMULATION RESULTS

#### 3.1 Pump

The experimental boundary conditions (pump shaft rotary speed, LS pressure, servo proportional valve opening and FC pressure set point) were imposed as inputs to the pump mathematical model. Figs. 12 to 14 show the comparison between the experimental and numerical results regarding dynamic tests on the pump, performed at constant shaft rotary speed (equal to 1500 r/min in cases *a* and *c*; and 2000 r/min in case *b*) and constant LS pressure (equal to 10.5 MPa in cases *a* and *b*; and 18.5 MPa in case *c*).

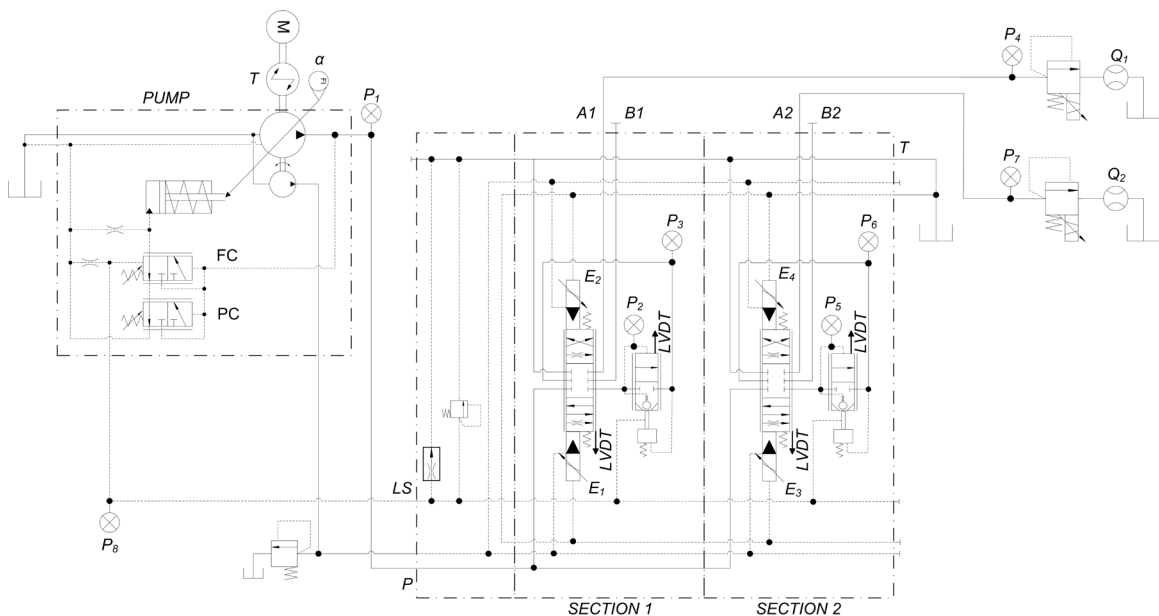


Fig. 11. Test setup for load-sensing, flow-sharing valve block

A satisfying match between the experimental and simulated swash plate positions is noticeable, as the simulated curve presents both overshoot and time constant very close to that from acquisitions for each of the working conditions tested.

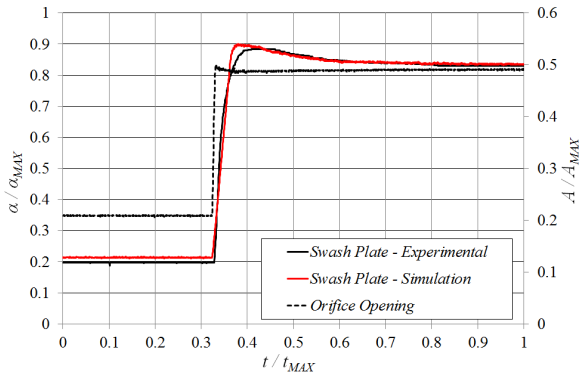


Fig. 12. Pump swash plate step response; case a

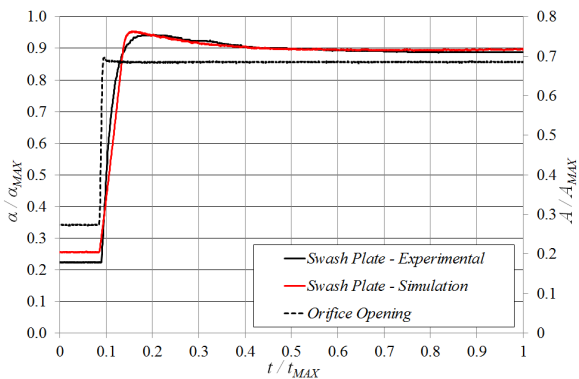


Fig. 13. Pump swash plate step response, case b

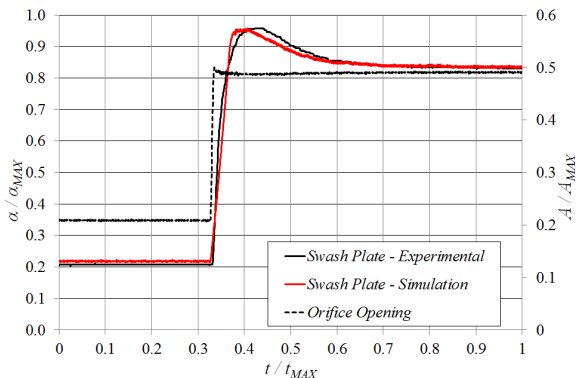


Fig. 14. Pump swash plate step response; case c

#### 4.2 Pump and Valve block

The simulations were performed using the load pressures and the pump shaft rotary speed recorded during experimental tests as inputs. The valves

opening were set equal to the experimental values acquired through the LVDTs installed.

Figs. 15 and 16 show the comparison between the experimental data and the simulation results for the intermediate chamber (see Fig. 8) of both valve sections. While the bridge chamber pressure is essentially equal to the effective load pressure as the pressure drop at the valve outlet is rather small due to large flow areas, the pressure in the intermediate chambers is equal to that of the section with the highest load (main section). That is to say, for the main section, the pressure drop across the compensator orifice is reduced as the compensator opens completely, while in the compensating section the flow is laminated in order to establish a pressure equal to that in the load-sensing line (i.e. the greatest one). The difference between the experimental values and the simulated one is less than 1%. Figs. 17 and 18 report the experimental and simulated positions of the compensator in both sections. As anticipated, when a section is compensating, the compensator laminates the flow in order to re-establish the desired pressure drop across the metering area and thus maintain the desired flow rate.

The pressure in the load-sensing line is essentially equal to that of the main section intermediate chamber, while the pump outlet pressure, i.e. valve inlet pressure (Fig. 19), is regulated by the flow compensator in order to be 2 MPa greater than the load-sensing pressure. The difference between experimental and simulated values is still less than 1%.

The outlet flow rate for both sections is shown in Figs. 20 and 21, and the swash plate angular position in Fig. 22. A good match exists between experimental and simulated data, with a maximum error in the evaluation of the outlet flow rate in the order of 10% of the maximum value, which is also ascribable to measuring errors in the main spool position, as the pressure perfectly matches that acquired.

### 4 EXCAVATOR MODEL AND SIMULATION

The results presented in the previous section show that the pump and valve models are capable of reproducing actual system working conditions. Thus, the model was extended to include the kinematics of a real excavator [8] and [18], and its hydraulic circuit ISO scheme is reported in Fig. 25. In order to present the capability of the complete model, it was subjected to a duty cycle described in Fig. 23, where the three valve spools were operated to simulate real operator actions during a typical digging cycle (without bucket-soil interaction), with the simultaneous opening of two or

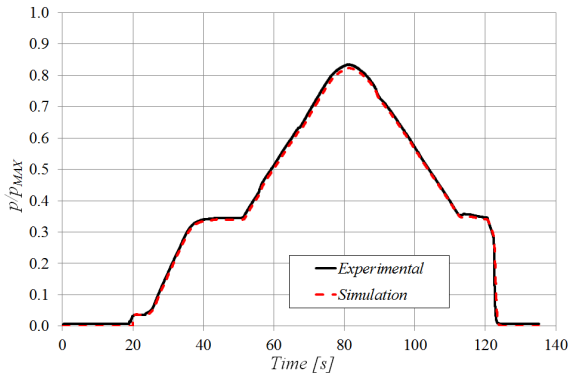


Fig. 15. Valve section 1 intermediate pressure

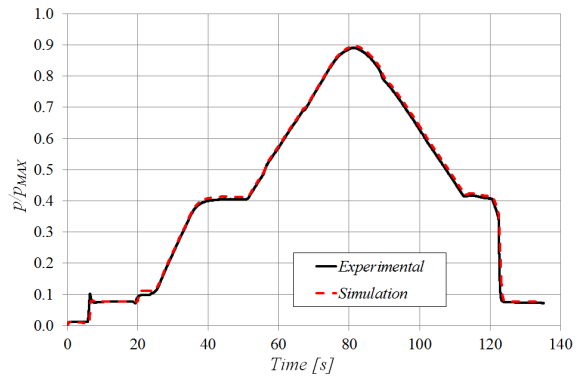


Fig. 19. Valve inlet pressure

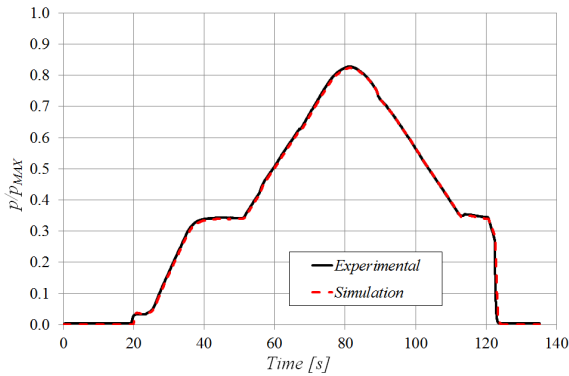


Fig. 16. Valve section 2 intermediate pressure

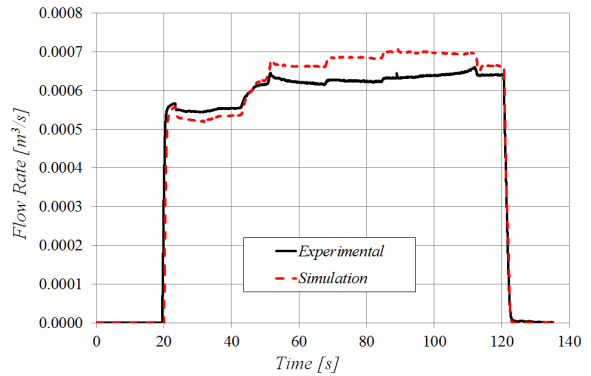


Fig. 20. Valve section 1 outlet flow rate

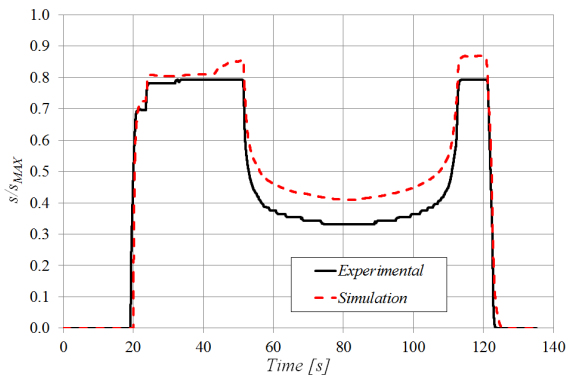


Fig. 17. Valve section 1 compensator displacement

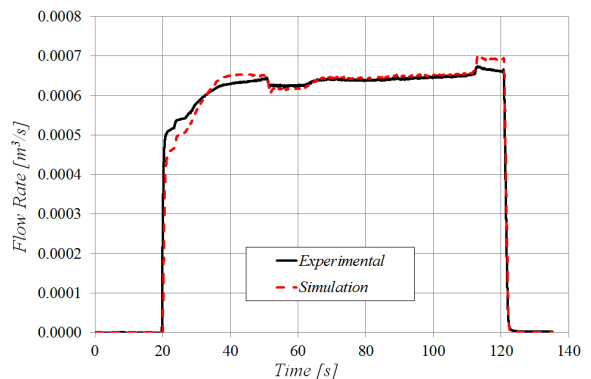


Fig. 21. Valve section 2 outlet flow rate

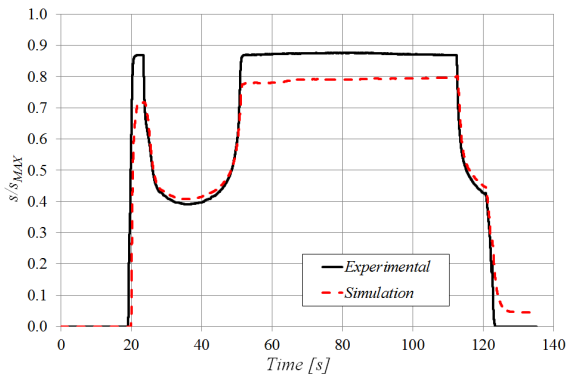


Fig. 18. Valve section 2 compensator displacement

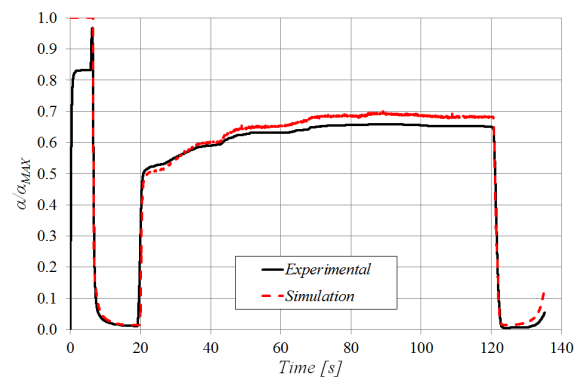


Fig. 22. Pump swash plate position

three valves. Because the external forces acting on the bucket were not considered, the load on the actuators is only due to inertial effects (as a consequence of boom, arm and bucket movements) and gravitational forces. Fig. 24 shows the instantaneous velocity of the excavation tool hydraulic actuators. Figs. 26 to 28 illustrate the pressure in boom, arm and bucket actuators, and the valve bridge chambers.

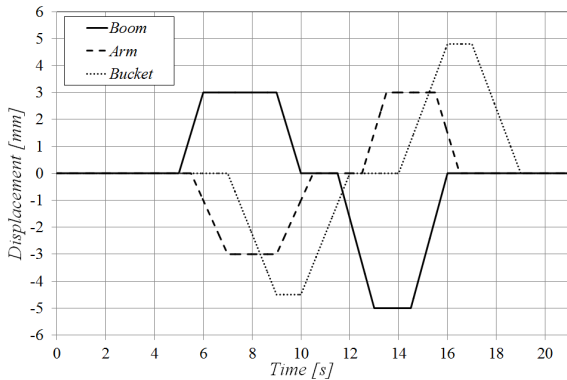


Fig. 23. Excavator duty cycle - valve main spools position

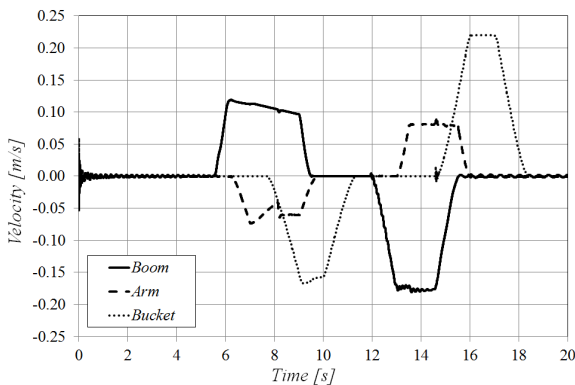


Fig. 24. Actuators velocity

Fig. 26 shows the oscillations due to the implements' inertial load, e.g. between 13 s and 15 s the boom velocity oscillates as a consequence of the simultaneous arm movements. Fig. 29 reports the pressure in the LS line and at the pump delivery line, the LS pressure line can be deduced by analysing Figs. 26 to 28, as a matter of the fact of where the LS line is the higher pressure request from the concurrent users. The flow rates through various valves can be seen in Fig. 30; as expected, the flow rate is not influenced by the effective load condition and is only a function of the valve opening, Fig. 23, as well know this is a feature of the LS systems. Fig. 31 represents the swash plate instantaneous position, held to guarantee the specific pump margin at the desired flow rate.

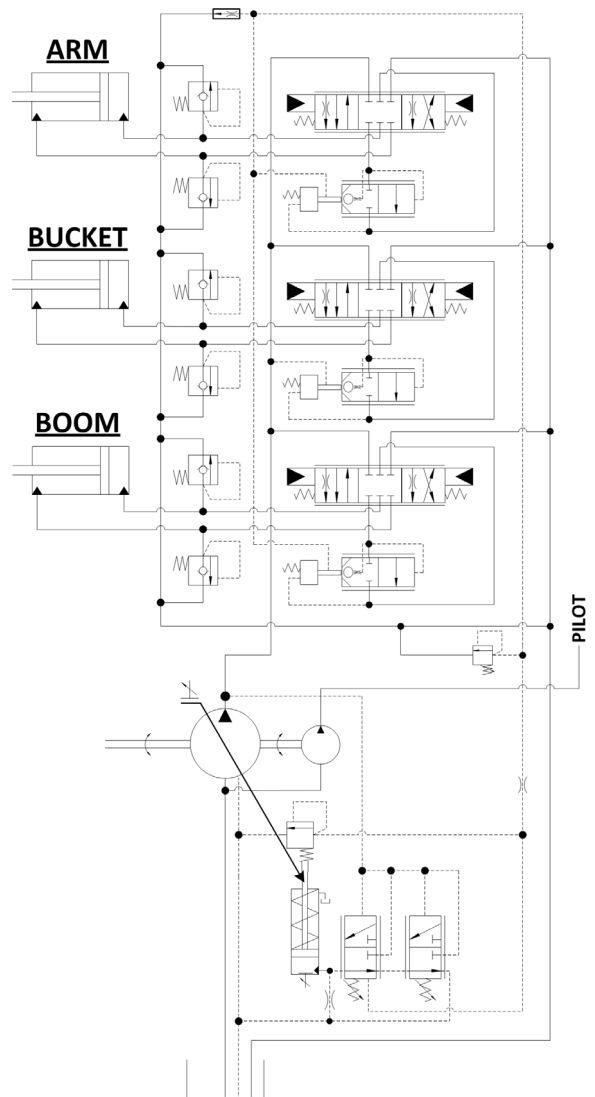


Fig. 25. Excavator's hydraulic system ISO scheme

Figs. 29 and 30 show the capability of the pump model to follow the request of the valve-opening law (flow rate demand) and to provide the correct delivery pressure in order to satisfy the load demand.

## 5 CONCLUSIONS

This paper presents a nonlinear mathematical model of an excavator hydraulic circuit, developed in the AMESim® modelling environment, able to replicate system actual operating conditions. The model is composed of hydraulic sub-models comprising a load-sensing variable displacement axial piston pump, a flow-sharing multi-section valve model and a 2D kinematic model to simulate the excavator's front excavation tool elements. The modelling approach

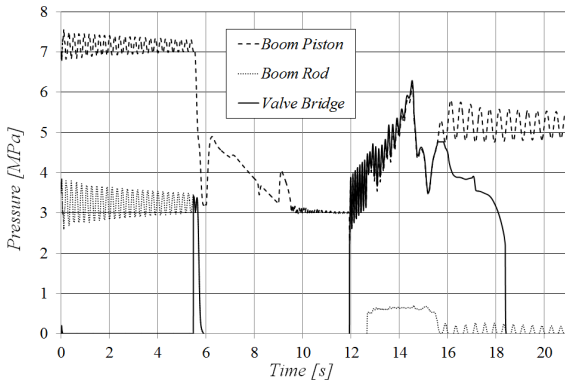


Fig. 26. Boom section pressures

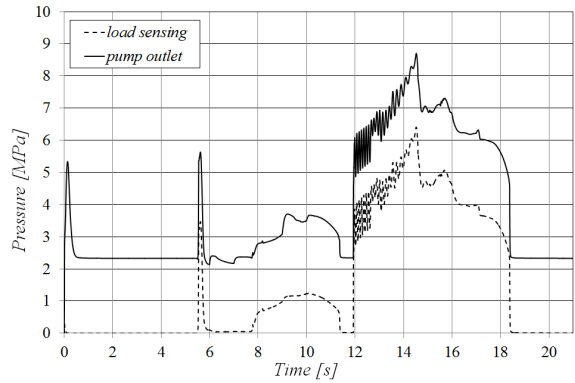


Fig. 29. Load-sensing and pump outlet pressure

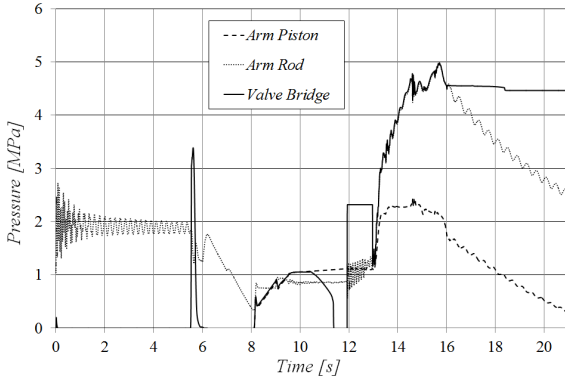


Fig. 27. Arm section pressures

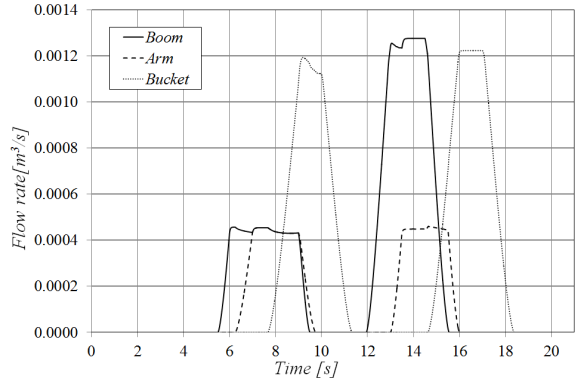


Fig. 30. Flow rates

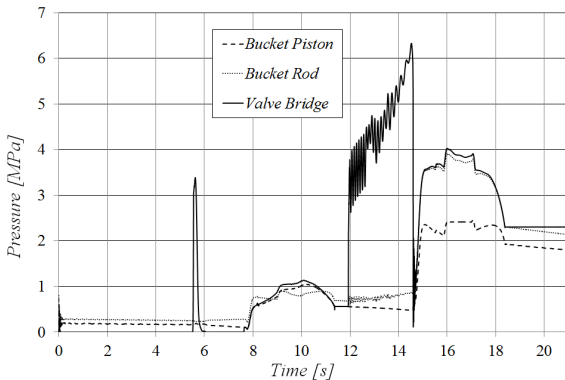


Fig. 28. Bucket section pressures

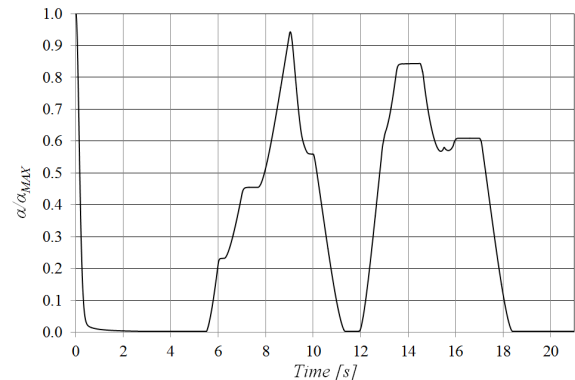


Fig. 31. Pump swash angle displacement

enables studying the system dynamic interaction in simulated actual load-sensing conditions where more than one section (multi-actuator) is used at the same time. The hydraulic model described consists of a grey box variable displacement pump model and a white box load-sensing, flow-sharing valve block model. The mathematical models have been validated and calibrated with stationary and dynamic tests in different conditions. The pump and valve models offer a satisfactory reproduction of realistic functioning conditions. The last section of the paper provides an

overall view of the hydraulic models capability coupled with the kinematics of an excavator. A combination of the various motions has been discussed, in an attempt to reproduce a realistic working cycle. The results presented show the potential of this model in aiding pump and valve designers in analysing/assessing the behaviour of their components when mounted in the entire system. The simplified modelling approach proposed enables replicating the most significant dynamics of the system components, during actual working conditions. Furthermore, the model proposed

requires short computational times and may be used for “control-oriented” applications; once compiled in a dynamic linked library (DLL), the mathematical model is able to run real-time simulations on a suitable HiL platform for designing and testing control, and developing diagnostic strategies.

## 6 ACKNOWLEDGMENTS

The authors would like to acknowledge the active support given to this research by Casappa S.p.A. and Walvoil S.p.A. (Italy).

## 7 NOMENCLATURE

$A_{ACT}$	Actuator piston area [m <sup>2</sup> ]
$c$	Viscous friction coefficient [Nm/(rad/s)]
$d_{ACT}$	Actuator piston arm [m]
$J_{EQ}$	Swash plate inertia [kg·m <sup>2</sup> ]
$\dot{m}$	Mass flow rate [kg/s]
$n$	Shaft rotary speed [r/s]
$p$	Pressure [Pa]
$T_{ACT}$	Actuator torque [Nm]
$T_n$	Barrel torque [Nm]
$V(x)$	Control volume [m <sup>3</sup> ]
$V_d$	Pump displacement [m <sup>3</sup> /r] Theoretical flow rate [m <sup>3</sup> /s]
$x$	Spool position [m]

### Greek Symbols

$\alpha$	Swash plate angular position [rad]
$\beta$	Bulk modulus [Pa]
$\eta_g$	Overall efficiency [-]
$\eta_{hm}$	Hydraulic-mechanical efficiency [-]
$\eta_v$	Volumetric efficiency [-]
$\rho$	Fluid density [kg/m <sup>3</sup> ]

### Subscript

$D$	Delivery
$i$	Volume index
$n$	Piston index

## 8 REFERENCES

- [1] Inderelst, M., Losse, S., Sgro, S., Murrenhoff, H. (2011). Energy efficient system layout for work hydraulics of excavators. *12<sup>th</sup> Scandinavian International Conference on Fluid Power*, Tampere, vol. 1, p. 177-191.
- [2] Zimmerman, J., Ivantysynova, M. (2011). Hybrid displacement controlled multi-actuators hydraulic systems. *12<sup>th</sup> Scandinavian International Conference on Fluid Power*, Tampere.
- [3] Casoli, P., Gambarotta, A., Pompini, N., Riccò, L. (2014). Development and application of co-simulation and control-oriented modeling in the improvement of performance and energy saving of mobile machinery. *Energy Procedia*, vol. 45, p. 849-858, DOI:10.1016/j.egypro.2014.01.090.
- [4] Wu, D., Burton, R., Schoenau, G., Bitner, D. (2007). Analysis of a pressure –compensated flow control valve. *In ASME Journal of Dynamic Systems, Measurement and Control*, vol. 129, no. 2, p. 203-211, DOI:10.1115/1.1870037.
- [5] Borghi, M., Specchia, E., Zardin, B. (2009). Numerical analysis of the dynamic behaviour of axial piston pumps and motors slipper bearings. *SAE International Journal of Passenger Cars - Mechanical System*, vol. 2, no. 1, p. 1285-1302, DOI:10.4271/2009-01-1820.
- [6] Zecchi, M., Ivantysynova, M. (2012). Cylinder block / valve plate interface – a novel approach to predict thermal surface. *8<sup>th</sup> International Fluid Power Conference*, Dresden.
- [7] Williamson, C., Lee, S., Ivantysynova, M. (2005). Active vibration damping for an off-road vehicle with displacement controlled actuators. *International Journal of Fluid Power*, vol. 10, no. 3, p. 5-16, DOI:10.1080/14399776.2009.10780984.
- [8] Casoli, P., Anthony, A. (2013). Gray box modeling of an excavator's variable displacement hydraulic pump for fast simulation of excavation cycles. *Control Engineering Practice*, vol. 21, no. 4, p. 483-494, DOI:10.1016/j.conengprac.2012.11.011.
- [9] McCloy, D., Martin, H.M. (1973). *The Control of Fluid Power*. Hellis Horwood Limited, London.
- [10] Casoli, P., Vacca, A., Franzoni, G., Berta, G.L. (2006). Modeling of fluid properties in hydraulic positive displacement machines. *Simulation Modeling Practice and Theory*, vol. 14, no. 8, , p. 1059-1072, DOI:10.1016/j.simpat.2006.09.006.
- [11] ISO4409-1986. *Hydraulic Fluid Power – Positive displacement pumps, motors and integral transmissions – Determination of steady-state performance*. International Organization for Standardization, Geneva.
- [12] Casoli, P., Anthony, A., Riccò, L. (2012). Modeling of an Excavator system – load sensing flow sharing valve model. *SAE Commercial Vehicle Engineering Congress*, Rosemont, DOI:10.4271/2012-01-2042.
- [13] LMS Imagine – AMESim® (2011). *Reference manual*, The American Society of Mechanical Engineers, New York.
- [14] Lin, S.-T., Huang, J.-N. (2002). Stabilization of Baumgarte's method using the Runge-Kutta approach. *ASME Journal of Mechanical Design*, vol. 124, no. 4, p. 633-641, DOI:10.1115/1.1519277.
- [15] Marquis-Favre, W., Bideaux, E., Scavarda, S. (2005). A planar mechanical library in the AMESim simulation software. Part I: Formulation of dynamics equations. *Simulation Modelling Practice and Theory*, vol. 14, no. 1, p.25-46, DOI:10.1016/j.simpat.2005.02.006.
- [16] Grzesikiewicz, W. (1998). Dynamics of a ground digging tool. *XI. Scientific Conference Problems of Work Machines*, Zakopane.
- [17] Šulc, B., Jan, J.A. (2002). Nonlinear modelling and control of hydraulic actuators. *Acta Polytechnica*, vol. 42, no. 3, p. 41-47.
- [18] Casoli, P., Gambarotta, A., Pompini, N., Riccò, L. (2015). Coupling excavator hydraulic system and internal combustion engine models for the real-time simulation. *Control Engineering Practice*, vol. 41, p. 26-37, DOI:10.1016/j.conengprac.2015.04.003.

# Non-Newtonian Shear-Thinning Fluid Passing Through a Duct with an Obstacle, Using a Power Law Model

Mohammadreza Saffarian<sup>1</sup> – Moona Mohammadi<sup>1,\*</sup> – Mohammadreza Mohammadi<sup>2</sup>

<sup>1</sup> Shahid Chamran University, Faculty of Mechanical Engineering, Iran

<sup>2</sup> Iranian National Gas Company, Bushehr Gas Company, Iran

*Non-Newtonian fluids have not been frequently considered in different research although they are common fluid type in the industry and environment in comparison to Newtonian fluids. In this paper, a non-Newtonian fluid with a shear-thinning property is considered in a specific geometric condition. The flow is considered to be laminar, and the geometric subject of the research is a rectangular duct with an obstacle, which is assumed to be in the middle of the duct with a height of half the duct width. This research provides a numerical solution using a written MATLAB code with a SIMPLEC algorithm and a power law model. This code is validated by comparing code results with analytical results for a specific condition. The results of this research show variations of velocity and viscosity in the duct, which can be extremely useful in future research and applications, not only because of frequent usage of shear-thinning fluids in industrial applications but also because of the common duct shape facilities in different processes in several industries.*

**Keywords:** non-Newtonian fluid, SIMPLEC, internal flow, shear-thinning flow

## Highlights

- Using numerical calculation for a non-Newtonian fluid.
- The behaviour of shear thinning fluid in a duct shape geometry with one obstacle.
- Variation of velocity and viscosity before and after an obstacle for shear-thinning fluids.
- Result validation with analytical solution.

## 0 INTRODUCTION

At present, the usage of non-Newtonian fluids is very common in industrial applications. Regarding significant differences between their properties and behaviour with that of Newtonian fluids, various research should be done to understand their behaviour in different conditions.

Computational fluid dynamics (CFD) is a common numerical calculation procedure that have been used in several simulation research studies for different geometries [1] to [7]. Rek et al. [1] used CFD simulation to analyse a heating oven. Lypse et al. [2] worked on an URANS simulation of flow for square cylinder geometry. Liao et al. [3] used CFD to simulate the flow in a directional valve. Vosoughifar et al. [4] worked on fluid flow over stepped spillways. Ravnik et al. [5] proposed a numerical model for particle movement in cellular flow. Ternik and Rudolf [6] considered a heated circular cylinder numerically. Herakovič et al. [7] proposed a fluid model for flow force reduction and used the Ansys CFX CFD simulation tool for their work.

Despite using CFD in all this and other similar research, different methods of CFD were mostly used in different conditions or industrial applications while for none of them was the fluid assumed to be non-Newtonian.

In contrast, non-Newtonian fluids were studied by several other researchers using two main approaches. In the first approach, a case study industrial application was considered [8] to [12]. Speetjens et al. [8] studied non-Newtonian fluid flow in industrial in-line mixers. Haun et al. [9] derived a lubrication equation for a non-Newtonian thin film. Marn et al. [10] had a biological focus on working with aortic valves. Petrun et al. [11] engaged various viscosity parameters in a modified elasto-plastic friction model and discussed their effect on the final friction force-torque, transmitted through the contact of the friction clutch. Another example of application of non-Newtonian fluids is in the drilling industry, studied by Safaïy et al. [12].

Although this approach follows an industrial case study, in the second approach a basic study has been developed that can be useful in several industrial applications [13] to [21]. Safaei et al. [13] and Ternik and Rudolf [14] considered heat transfer convection in a determined geometry with a specific non-Newtonian fluid. Ntamba and Fester [15] worked on short square-edged orifice plates to determine pressure losses. Ashhab et al. [16] studied blood flow as a non-Newtonian fluid and selected micro-channels as the problem geometry using FLUENT to solve the CFD procedure. Similarly, Bandyopadhyay and Das [17] used CFD and FLUENT for solving a procedure; however, they worked with an elbow

shape to investigate non-Newtonian and gas non-Newtonian liquid flow. Shahmardan et al. [18] worked on a channel with a cavity shape. Norouzi et al. [19] used an analytical solution in a curved rectangular duct for a creeping dean flow of Bingham plastic. Other examples of non-Newtonian fluid research are Maghmoumi et al. [20] Yao and Molla [21], both working on flat plates.

The current research follows a numerical solution for a non-Newtonian fluid passing a duct, which is generally the same method of all the aforementioned research. The main approach of this research can be determined as basic research [13] and [21] using power law [10], [17] and [21] as the solution method. The problem geometry has some similarities with [8] and [19], and shear-thinning fluid was considered in [21]. Despite all these similarities, the unique geometry of this research in which a plane is placed in the middle of the duct and the size of the plane is half the height of the duct width had not previously been considered, while the final results of this paper lead to an illustration of the velocity profile and the viscosity variation in different values of index  $n$  for a shear-thinning fluid.

### 1 MATERIAL AND METHOD

Newtonian fluid behaviour passing an obstacle can be dramatically different from that of a non-Newtonian fluid. In a Newtonian fluid, viscosity is constant, so velocity distribution will be obtained from a constant viscosity, while in a non-Newtonian fluid viscosity is variable and is dependent on different velocity gradients in the flow field.

According to fluid type, a non-Newtonian fluid can be considered by different mathematical models, such as power law, which are applicable for shear-thinning and shear-thickening fluid. In this model, the tension value and fluid shear rate can be defined as Eqs. (1) and (2) [22].

$$\tau_{yx} = m\dot{\gamma}_{yx}^n \tag{1}$$

$$\mu = m\dot{\gamma}^{n-1} \tag{2}$$

where  $m$  and  $n$  are power coefficients and  $\tau_{yx}$ ,  $\dot{\gamma}_{yx}$  and  $\mu$  are shear stress, shear rate and viscosity, respectively. The  $n$  value in these two fluid type is defined as follows.

$$\text{Shear thinning } n < 1, \tag{3}$$

$$\text{Shear thickening } n > 1. \tag{4}$$

In this research, a MATLAB code is used for calculations based on the SIMPLEC method to obtain

velocity distribution, while flow is considered to be laminar.

Three different grid networks were considered to show network independence. Considering  $21 \times 83$  grid,  $25 \times 100$  grid and  $31 \times 125$  grid, it was deduced that velocity has very little difference in these grids. Thus, a  $25 \times 100$  grid is used in calculations due to a reduced calculation time with the same accuracy. Table 1 shows mesh independence in considered grids.

**Table 1.** Mesh number and average of lateral velocity results

Mesh Number	21×83	25×100	31×125
Average of lateral velocity above obstacle [m/s]	0/967744	0/976555	0/981629

### 1.1 Mathematical Method

While Navier-Stocks equations are applicable in Newtonian fluids, in non-Newtonian fluids Cauchy equations are used. The governing equations in steady, 2-dimentional and isotherm conditions are as follows [23]:

$$\frac{\partial V_x}{\partial x} + \frac{\partial V_y}{\partial y} = 0, \tag{5}$$

$$\rho[V_x \frac{\partial V_x}{\partial x} + V_y \frac{\partial V_x}{\partial y}] = -\frac{\partial P}{\partial x} + \frac{\partial \tau_{xx}}{\partial x} + \frac{\partial \tau_{xy}}{\partial y}, \tag{6}$$

$$\rho[V_x \frac{\partial V_y}{\partial x} + V_y \frac{\partial V_y}{\partial y}] = -\frac{\partial P}{\partial y} + \frac{\partial \tau_{yx}}{\partial x} + \frac{\partial \tau_{yy}}{\partial y}. \tag{7}$$

Unlike Newtonian fluid, the relation between the tension and shear rate in non-Newtonian fluid is non-linear.

As mentioned before, the Cauchy momentum in non-Newtonian fluids is the governing equation, but Navier-Stocks equations can be used in numerical solutions if in every grid viscosity assumed to be constant and viscosity variation assumed to be variable in all the field.

The calculated viscosity in Eq. (1) is a scalar value due to the use of rheometer and shear rate, while viscosity and shear rate is a tensor so it is necessary to use the average  $\dot{\gamma}$  for viscosity calculation.

For solving this problem, the average shear rate value is used. This value, which is called the extended shear rate, is defined as follows [18]:

$$\bar{\dot{\gamma}} = \bar{\dot{\gamma}} = \sum_i \sum_j \dot{\gamma}_{ij} \dot{\gamma}_{ji}. \tag{8}$$

In Eq. (8), the shear rate value is calculated according to Eq. (9) [18]:

$$\dot{\gamma} = \{2[(\frac{\partial V_x}{\partial x})^2 + (\frac{\partial V_y}{\partial y})^2 + (\frac{\partial V_z}{\partial z})^2] + (\frac{\partial V_x}{\partial x} + \frac{\partial V_y}{\partial y})^2 + (\frac{\partial V_x}{\partial x} + \frac{\partial V_z}{\partial z})^2 + (\frac{\partial V_y}{\partial y} + \frac{\partial V_z}{\partial z})^2\}^{0.5}. \tag{9}$$

For this calculation, it is necessary to estimate the field velocity as the first step; after calculating  $\dot{\gamma}$  from Eq. (9), viscosity would be calculated via Eq. (1) and is substituted in Eq. (10).

$$\mu = 0.9\mu_{old} + 0.1\mu_{new}. \tag{10}$$

The value of  $\mu_{old}$  can be assumed to be a Newtonian fluid viscosity. The value of  $\mu_{new}$  is calculated value from Eq. (1).

Because the flow is assumed to be laminar, it is necessary to calculate critical Reynolds number to determine maximum velocity in which the flow in the duct remains laminar. Eq. (11) shows how to calculate critical Reynolds [22].

$$Re_{MR_c} = \frac{6464n}{(3n+1)^2} (2+n)^{(2+n)/1+n}. \tag{11}$$

In Eq. (11)  $Re_{MR_c}$  is critical Reynolds and  $n$  is index number of non-Newtonian fluid.

Substituting obtained critical Reynolds from Eq. (11), critical velocity will be obtained from Eq. (12). The value of diameter ( $D$ ) in Eq. (12) is calculated based on the hydraulic diameter. Because the considered problem is a duct, the hydraulic diameter will be obtained from Eq. (13) [8].

$$Re_{PL} = \frac{\rho V^{2-n} D^n}{8^{n-1} m \left(\frac{3n+1}{4n}\right)^n}, \tag{12}$$

$$D_h = \frac{4A}{P} = \frac{4ab}{2(a+b)} = \frac{2ab}{(a+b)}. \tag{13}$$

In this equation,  $a$  and  $b$  are the width and height of the considered section.

As previously mentioned, the equation under consideration is solved based on the SIMPLEC method. To avoid divergence, a velocity matrix is divided into internal and external sections and is assumed to be zero in the boundary. The entrance boundary is separated from calculated values and is applied as a boundary condition of this matrix. The upwind method and staggered grid are used for discretization. Fig. 1 shows how to determine grids in this mesh generation. Pressure and velocity

coefficients in the numerical solution are 0.3 and 0.5 respectively [24].

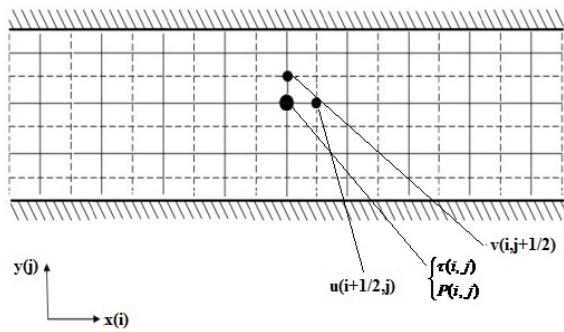


Fig. 1. Velocity and pressure node in staggered grid

## 2 RESULTS AND DISCUSSION

In this research, a duct with the length of 1 m and the height of 25 cm is considered. As previously mentioned, the selected grid network is 25×100 in the  $y \times x$  plane. The duct has an obstacle in the middle, as shown in Fig. 2. Velocities on the wall are assumed to be zero and assumed to be a certain value in the entrance boundary in the program.

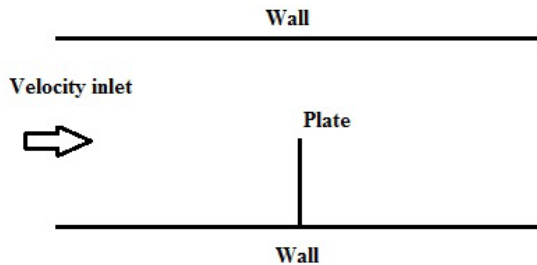


Fig. 2. Schematic of duct

Numerical solution validation can be performed by comparing the results with experimental, analytical solutions or previously validated numerical solutions. Shahmardan et al. [18] compared their results with an analytical solution, while a Newtonian fluid was used in the validation section. Similarly, in this paper, the same method was used and the results of numerical solution code were compared with an analytical solution for a Newtonian fluid. For the purpose of validation, the code was applied on a duct with no obstacle in the middle using a Newtonian fluid as a passing fluid. Table 2 shows the results of calculated velocity values in different Reynolds numbers while the analytical result in the considered point is 1 m/s.

In this research, four different fluids with different values of  $m$  and  $n$  have been considered.

Table 3 shows fluid properties and critical Reynolds in each considered fluid. According to the properties of each fluid, critical Reynolds will be calculated according to Eq. (11). To make the results of different fluids comparable, an equal Reynolds number (150) was used.

**Table 2.** Calculated velocities in different Reynolds numbers

Calculated numerical velocity	Reynolds number
0.9930	800
0.9949	900
1.0013	1000
1.0000	1100

**Table 3.** Properties of four selected fluids [22]

$n$	$m$	$\rho$ [kg/m <sup>3</sup> ]	$Re_{cr}$
0.5	12	1130	2381.46
0.68	0.4	1000	2292.13
0.3	9.6	1090	2344.74
0.41	2.6	1225	2422.65

Fig. 3 shows viscosity variation in Reynolds number 150 in different  $n$  values. This figure demonstrates that at the place of the obstacle, a huge variation in viscosity occurs and there is a dramatic drop before the obstacle and a sharp increase after that. The amount of this drop in  $n = 0.5$  is higher than other values of  $n$ .

When all properties, such as  $m$  and density, are engaged, the viscosity variation does not have a certain order.

For determining the effect of  $n$ , viscosity is calculated in a specific condition in which density and the  $m$  value are equal and just  $n$  changes. This condition is shown in Fig. 4, which illustrates that the increasing value of  $n$  will result in an increase in viscosity.

Lateral velocity passing on the obstacle in different  $n$  numbers is shown in Figs. 5 and 6. These figures illustrate that fluid velocity passing on the obstacle would have sudden changes because of constant value of velocity and cross sectional area changing, and that in nodes beside the obstacle a sharp increase would happen.

Figs. 7 and 8 demonstrate velocity variations in the duct, which have a significant variation above the obstacle; in  $n = 0.68$ , the velocity increase is at maximum; for  $n$  values of 0.41, 0.3 and 0.5, the velocity increase is decreasing, respectively.

Regarding Fig. 3, these variations are exactly the opposite of the variation of viscosity passing the

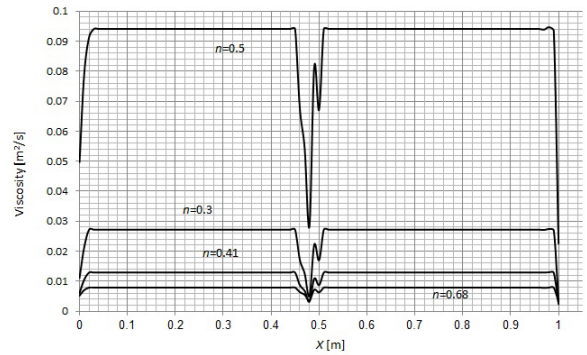


**Fig. 3.** Viscosity variations in axial direction,  $Re=150$

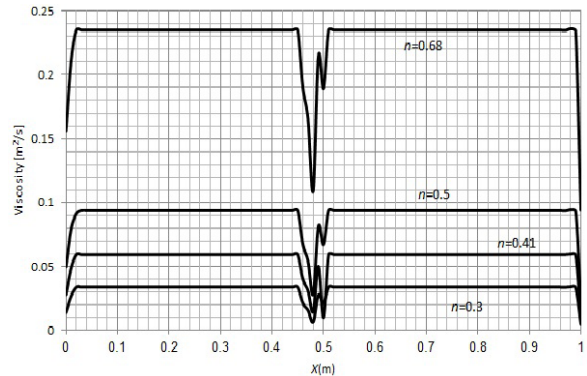


**Fig. 4.** Comparison of 4 different hypothetical  $n$  index,  $Re=150$ ,  $\rho = 1130$  kg/m<sup>3</sup>,  $m=12$

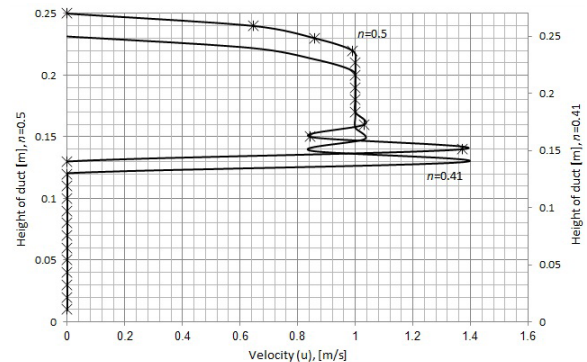


**Fig. 5.** Lateral velocity passing in obstacle in different  $n$  number,  $Re=150$

obstacle. In other words, regarding low viscosity, fluid resistance against the movement is less.

Figs. 9 to 12 illustrate variation of the lateral velocity before and after the obstacle in 4  $n$  values. According to these figures, before the obstacle velocity is increased and after that the velocity is decreased. In three values of  $n$ , 0.68, 0.5 and 0.3, the velocity increase is similar but in  $n = 0.41$  the velocity increase is less due to the higher density in the fluid.

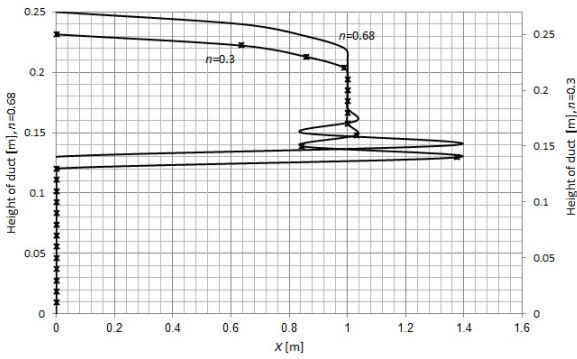


**Fig. 6.** Lateral velocity passing in obstacle in different  $n$  number,  $Re=150$

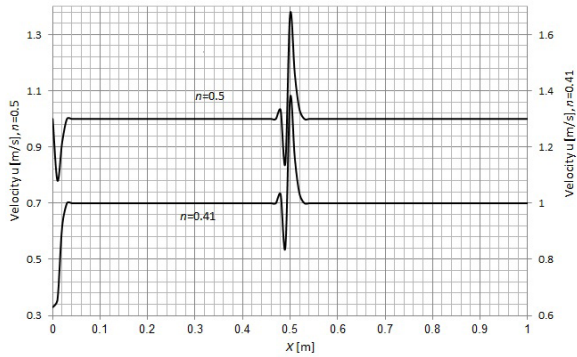


**Fig. 7.** Velocity variations in axial direction,  $Re=150$

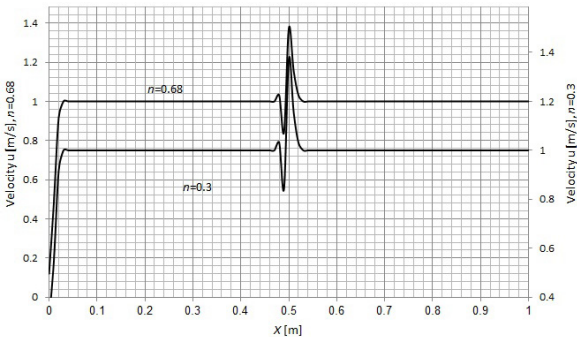


**Fig. 8.** Velocity variations in axial direction,  $Re=150$

It can be deduced that velocity increase is related to viscosity decrease, and the velocity decrease is dependent on viscosity increase.

### 3 CONCLUSION

In this paper, non-Newtonian shear-thinning fluid in a duct passing an obstacle is considered and four values of  $n$  are used.

The results of this research show that in constant fluid properties the increase in value of  $n$  will also

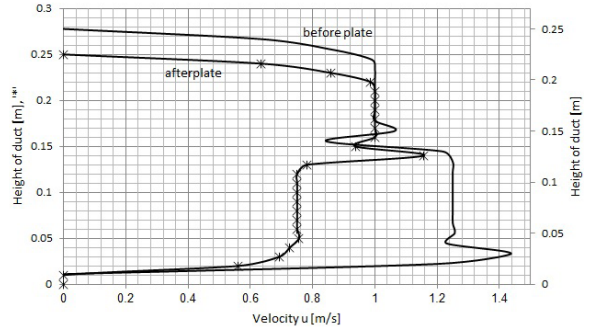


**Fig. 9.** Velocity variations in lateral direction before and after obstacle,  $Re = 150, n = 0.68$

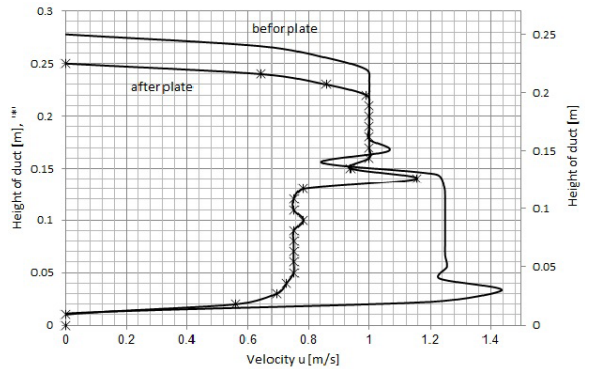


**Fig. 10.** Velocity variations in lateral direction before and after obstacle,  $Re=150, n=0.5$

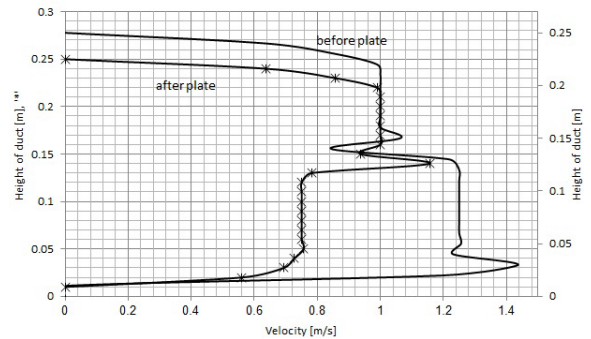


**Fig. 11.** Velocity variations in lateral direction before and after obstacle,  $Re=150, n=0.3$

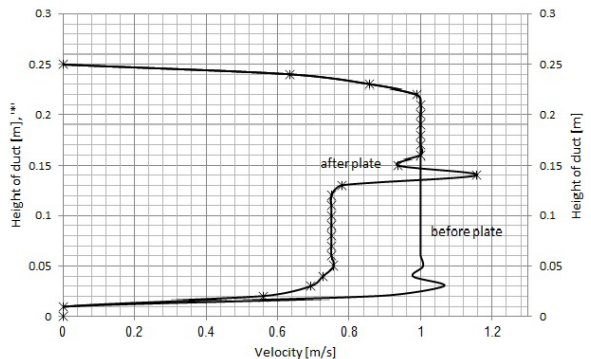


**Fig. 12.** Velocity variations in lateral direction before and after obstacle,  $Re=150, n=0.41$

cause an increase in viscosity. Velocity variation in the duct has an opposite relation with viscosity; in the minimum value of viscosity, the velocity would be maximum due to low fluid resistance against the flow movement. Because of rapid changes in the cross-sectional area in the flow passing the obstacle, velocity has a significant increase in nodes near the plate.

The results of this research revealed a huge decline before the obstacle and a significant rise after that, while the amount of this drop in  $n = 0.5$  is higher than other values of  $n$ . The results also showed similarities between three values of  $n$ , 0.68, 0.5 and 0.3, in velocity increase while, at  $n = 0.41$  the velocity increase is less due to the higher density in the fluid.

This paper finally provided the variation of velocity and viscosity and their dependence on fluid properties in a specific geometry. Although some similarities can be found in the geometrical aspects in previous research in which the duct shape was considered, this paper focused on the effect of a plate in the middle of the duct on velocity and viscosity variations. The other major finding of this paper is the fluid type assumption (i.e. shear thinning), which had not frequently been considered in previous research and had been never studied in such a geometry before.

#### 4 NOMENCLATURE

$m$	Power coefficient [-]
$n$	Power coefficient [-]
$\tau$	Shear stress [kg/m·s <sup>2</sup> ]
$\tau_{ij}$	Shear stress in $i, j$ plane [kg/m·s <sup>2</sup> ]
$\dot{\gamma}$	Shear rate [s <sup>-1</sup> ]
$\dot{\gamma}_{ij}$	Shear rate in $i, j$ plane [s <sup>-1</sup> ]
$\mu$	Viscosity [m <sup>2</sup> /s]
$V$	Velocity [m/s]
$V_i$	Velocity in $i$ direction [m/s]
$P$	Pressure [kg/m·s <sup>2</sup> ]
$\rho$	Density [kg/m <sup>3</sup> ]
Re	Reynolds number
$Re_{MR_c}$	Critical Reynolds
$D$	Diameter [m]

#### 5 REFERENCES

- [1] Rek, Z., Rudolf, M., Zun, I. (2012). Application of CFD simulation in the development of new generation heating oven. *Strojniški vestnik - Journal of Mechanical Engineering*, vol. 58, no. 2, p. 134-144, DOI:10.5545/sv-jme.2011.163
- [2] Lapse, J., Skerget, L., Ravnik, J. (2015). BEM-based algorithm for URANS simulation of flow over a square cylinder. *Strojniški vestnik - Journal of Mechanical Engineering*, vol. 61, no. 4, p. 254-264, DOI:10.5545/sv-jme.2014.2185
- [3] Liao, Y., Yuan, H., Lian, Z., Feng, J., Guo, Y. (2015). Research and analysis of hysteresis characteristics of a large flow directional valve. *Strojniški vestnik - Journal of Mechanical Engineering*, vol. 61, no. 6, p. 355-364, DOI:10.5545/sv-jme.2015.2487.
- [4] Vosoughifar, H., Dolatshah, A., Shokouhi, S., Nezhad, S. (2013). Evaluation of fluid flow over stepped spillways using the finite volume method as a novel approach. *Strojniški vestnik - Journal of Mechanical Engineering*, vol. 59, no. 5, p. 301-310, DOI:10.5545/sv-jme.2012.669.
- [5] Ravnik, J., Hribersek, M., Vogel, F., Steinmann, P. (2014). Numerical simulation of particle movement in cellular flows under the influence of magnetic forces. *International Journal of Simulation Modelling*, vol. 13, no. 3, p. 312-322, DOI:10.2507/IJSIMM13(3)4.268.
- [6] Ternik, P., Rudolf, R. (2014). Laminar forced convection heat transfer. *International Journal of Simulation Modelling*, vol. 13, no. 3, p. 312-322, DOI:10.2507/IJSIMM13(3)5.271.
- [7] Herakovič, N., Duhovnik, J., Šimic, M. (2015). CFD simulation of flow force reduction in hydraulic valves. *Tehniški vjesnik - Technical Gazette*, vol. 22, no. 2, p. 453-463, DOI:10.17559/TV-20141128090939.
- [8] Speetjens, M., Rudman, M., Metcalfe, G. (2006). Flow Regime Analysis of Non-Newtonian Duct Flow. *Physics of Fluids*, vol. 18, no. 1, p. 013101-1/14, DOI:10.1063/1.2163913.
- [9] Huan, J., Zhang, L. (2006). A variational approach to the establishment of a lubrication equation for a non-Newtonian thin film. *Strojniški vestnik - Journal of Mechanical Engineering*, vol. 52, no. 9, p. 587-591.
- [10] Marn, J., Iljaz, J., Zonic, Z., Ternik, P. (2012). Non-Newtonian blood flow around healthy and regurgitated aortic valve with coronary blood flow involved. *Strojniški vestnik - Journal of Mechanical Engineering*, vol. 58, no. 7-8, p. 482-491, DOI:10.5545/sv-jme.2010.023.
- [11] Petrun, T., Flaker, J., Kegl, M. (2013). A theoretical and numerical study of an additional viscosity term in a modified elasto-plastic friction model for wet friction clutch simulation. *Strojniški vestnik - Journal of Mechanical Engineering*, vol. 59, no. 6, p. 358-366, DOI:10.5545/sv-jme.2012.920.
- [12] Safaie, M., Maghroumi, Y., Karimipour, A. (2012). Numerical investigation of turbulence mixed convection heat transfer of water and drilling mud inside a square enclosure by finite volume method. *The 4th International Meeting of Advances in Thermofluids*, vol. 1440, no. 1, AIP Publishing, DOI:10.1063/1.4704283.
- [13] Safaie, M., Rahmani, B., Goodarzi, M. (2011). Numerical study of laminar mixed convection heat transfer of power-law. *International Journal of Physical Sciences*, vol. 6, no. 33, p. 7456-7470, DOI:10.5897/IJPS11.1092.
- [14] Ternik, P., Rudolf, R. (2013). Laminar natural convection of non-Newtonian nanofluids in a square enclosure with differentially heated side walls. *International Journal of Simulation Modelling*, vol. 12, no. 1, p. 5-16, DOI:10.2507/IJSIMM12(1)1.215.
- [15] Ntamba, B., Fester, V. (2012). Pressure losses and limiting Reynolds numbers for non-Newtonian fluids in short square-

- edged orifice plates. *Journal of Fluids Engineering*, vol. 134 no. 9, p. 091204-091204-9, DOI:10.1115/1.4007156.
- [16] Ashhab, M., Al-Salaymeh, A., Al-Muhtaseb, A., Al-Muhtaseb, M. (2012). Hershel- Bulkley Blood Flow in Rectangular Microchannels. *International Journal of Research and Reviews in Applied Sciences*, vol. 10, no. 1, p. 23-29.
- [17] Bandyopadhyay, T., Das, S. (2013). Non-Newtonian liquid flow through elbows- CFD analysis. *Journal Applied Fluid Mechanics*, vol. 6, no. 1, p. 131-141.
- [18] Shahmardan, M., Norouzi, M., Naghikhani, A. (2014). Numerical simulation of non-Newtonian Fluid through a channel with a cavity. *Modares Mechanical Engineering*, vol. 14, no. 6. p. 35-40. (In Persian)
- [19] Norouzi, M., Vamerzani, B., Davoodi, M., Biglari, N., Shahmardan, M. (2015). An exact analytical solution for creeping dean flow of Bingham plastics through curved rectangular ducts. *Rheologica Acta*, vol. 54, no. 5, p. 391-402, DOI:10.1007/s00397-014-0807-x.
- [20] Maghmoumi, Y., AbolHasan Alavi, S., Safaei, M., Nourollahi, I. (2008). Numerical analyses of steady non-Newtonian flow over flat plate on intermediate Reynolds Numbers by finite volume method. *International Journal of Advanced Design and Manufacturing Technology*, vol. 1, no. 4, p. 21-31.
- [21] Yao, L., Molla, M. (2007). The boundary layer of a non-Newtonian fluid on a flat plate with a uniform heat flux. *Journal of Heat Transfer*, vol. 131, no. 1, p. 011702-011708, DOI:10.1115/1.2977610.
- [22] Chhabra, R., Richardson, J. (2008). *Non Newtonian Flow and Applied Rheology*, Elsevier, Amsterdam.
- [23] Irgens, F. (2014). *Rheology and Non-Newtonian Fluids*. Springer International Publishing, Heidelberg, DOI:10.1007/978-3-319-01053-3.
- [24] Patankar, S. (1990). *Numerical Heat Transfer and Fluid Flow*. Mc Graw Hill Book Company, New York.

# The Influence of Micro- and Nano-Filler Content on the Mechanical Properties of Epoxy Composites

Iskender Ozsoy<sup>1</sup> – Askin Demirkol,<sup>1,\*</sup> – Abdullah Mimaroglu<sup>1</sup> – Huseyin Unal<sup>1</sup> – Zafer Demir<sup>2</sup>

<sup>1,\*</sup> University of Sakarya, Faculty of Engineering, Turkey

<sup>2</sup> University of Anadolu, Porsuk High School, Turkey

*In this study, the influence of micro- and nano-filler content on the mechanical properties of epoxy composites was studied. The matrix material is epoxy; the micro-fillers are Al<sub>2</sub>O<sub>3</sub>, TiO<sub>2</sub> and fly ash added in 10 wt% to 30 wt% by weight ratio; the nano-fillers are Al<sub>2</sub>O<sub>3</sub>, TiO<sub>2</sub> and clay added in 2.5 wt% to 10 wt% by weight ratio. Test samples were prepared using an open mould type die. Tensile, three-point bending and hardness tests were carried out. The tensile strength, elastic modulus, elongation at break, flexural strength, flexural modulus, and the hardness of the composite materials were obtained and evaluated. The results show that the tensile strength, flexural strength and elongation at the break values of composites decreased while the tensile modulus and flexural modulus increased with the increasing micro- and nano-filler content ratio.*

**Keywords:** micro-filler; nano-filler; mechanical properties; epoxy; composite

## Highlights

- This paper highlights possible reasons for variations in the mechanical properties of composites filled with nano- and micro-filler to compare the mechanical property of composites containing various amounts of nano- and micro-fillers.
- Small amounts of nano-size particles in epoxy have a strong effect on both tensile and flexural strength as well as ductility.
- Agglomeration problems have been observed at a higher amounts of filler ratios in composites.

## 0 INTRODUCTION

Various fillers have been used to design the desired properties in the polymer matrix. These fillers are mineral fillers, agricultural and/or puzzolanic wastes. In this field, researchers have studied the effects of particle shape, filler type, size, content ratio, and adhesion between matrix and fillers on the mechanical properties of polymer composites. Zaman et al. [1] studied the micro- and nano- ZnO-filled polypropylene composites with filler ratios between 2 wt% to 8 wt%. Nano-filled composites showed better results than micro-filled composites at the same filler ratios. They stated that the dispersion of particles is optimal in the 5 wt% filler content because the morphology images and dispersion of nano-fillers were better, which led to stronger interfacial adhesion between matrix and fillers. Gao et al. [2] studied nano- CaCO<sub>3</sub>-filled polystyrene composites. They concluded that fillers added stiffness to the polymer composite, but increasing the filler ratio beyond that point caused an agglomeration of particles, which decreased the adhesion between matrix and fillers and caused a drop in the mechanical strength of the composite. Agubra et al. [3] investigated the effects of dispersion methods on the mechanical behaviour of nano-clay-filled glass fibre epoxy composites. They stated that increasing viscosity causes problems in the homogeneous dispersion of fillers and results in

the agglomeration of the filler particles. Lam et al. [4] studied the hardness values of nano-clay-filled epoxy composites. They stated that the hardness values of the composite is increased by adding nano-clay fillers up to a limit and then decreased because of clusters at the high filler ratios. Yasmin and Daniel [5] investigated graphite-filled epoxy composites with 2.5 % to 5 % by weight filler ratios. They concluded that the tensile strength and modulus of the composite are increased by adding fillers, and an agglomeration of fillers occurred at a 5 wt% filler ratio. Sayer [6] used ceramic fillers, such as SiC, Al<sub>2</sub>O<sub>3</sub>, and B<sub>4</sub>C, in the glass-reinforced epoxy resin. He concluded that the elastic modulus and buckling load carrying capability of composites were increased by adding ceramic fillers. Asi [7] studied the mechanical properties of Al<sub>2</sub>O<sub>3</sub>-filled glass fibre-reinforced epoxy composites. He concluded that the tensile strength of composites decreased with the addition of Al<sub>2</sub>O<sub>3</sub> fillers. While the bending strength increased up to 10 wt% filler ratio and decreased at higher ratios. Yang et al. [8] studied the mechanical properties of rice husk flour-filled polypropylene composites. They stated that high filler ratios increased the interfacial area and made the polymer composite brittle. Thus, the tensile and impact strength of the composites decreased while the tensile modulus increased. Ibrahim et al. [9] investigated oil palm ash-filled unsaturated polyester composites with 10 wt% to 30 vol% filler ratios. They

\*Corr. Author's Address: University of Sakarya, Faculty of Engineering, Sakarya, Turkey, askind@sakarya.edu.tr

observed an increase in the modulus and a decrease in the tensile and flexural strength of the composites with added filler materials. Li et al. [10] studied rice bran carbon/nitrile rubber composites. They investigated different particle size effects and reached a better dispersion with small particle fillers. Increasing the particle size and the filler ratio caused difficulties in the homogeneous dispersion of fillers, leading to weak adhesion between matrix and fillers. Imoisili et al. [11] investigated cocoa pod-filled epoxy composites with 5 wt% to 30 wt% filler ratios. They stated that the best dispersion of the filler was at the 5 wt% filler ratio. Furthermore, the mechanical strength values decreased while modulus and microhardness values increased when fillers were added. Ray et al. [12] studied the mechanical properties of fly ash-filled vinylester composites. They stated that the fly ash increased the stiffness and rigidity of composite, but the mechanical strength was reduced with a high content ratio. Raja et al. [13] studied fly ash-impregnated glass fibre-reinforced polyester composites. The addition of 10 wt% fly ash improved the mechanical properties of the composite. Chauhan and Thakur [14] investigated the filler size and loading effects on the mechanical and tribological performance of cenosphere-filled vinylester composites. They stated that the mechanical and tribological performance increased, and optimum values were obtained with a 6 wt% filler ratio. Prakash et al. [15] investigated the influence of micro- and nano-fillers on the mechanical properties of pultruded unidirectional glass fibre-reinforced epoxy composite systems and concluded that the improved mechanical properties indicate that the unidirectional glass fibre-reinforced epoxy with combined micro- and nanofiller-filled composite is a good candidate for structural application. Manjunath et al. [16] studied the effect of filler content on the performance of epoxy/PTW composites and concluded that PTW additions showed beneficiary effects on the density, hardness, and stiffness properties of composites; however, strength properties and ductility were found to decrease with the increasing content of PTW. Finally, Sudheer et al. [17] gave a general review of epoxy composites and particularly on ceria epoxy nanocomposites.

In this study, the influence of the micro- and nano-filler content ratios of the mechanical properties of epoxy composites was studied. For this purpose, tensile, three-point bending, and hardness tests were carried out. Tensile strength, elastic modulus, elongation at break, flexural strength, flexural modulus and the hardness of the epoxy composites were obtained and evaluated.

## 2 EXPERIMENTAL

### 2.1 Materials

In this study, epoxy resin is the polymer matrix material. Micro-fillers, such as aluminium oxide ( $\text{Al}_2\text{O}_3$ ), titanium dioxide ( $\text{TiO}_2$ ) and fly ash, were added at a 10 % to 30 % by weight ratio. Nano-fillers, such as aluminium oxide ( $\text{Al}_2\text{O}_3$ ), titanium dioxide ( $\text{TiO}_2$ ) and nanoclay, were added at 2.5 % to 10 % by weight ratios. The materials used and their properties are given in Table 1.

**Table 1.** Properties of materials used

Materials	Properties	Density [gr/cm <sup>3</sup> ]	Supplier
Epoxy resin (MGS L285)	Bisphenol A	1.178	Dost Chemia Co.
Aluminium oxide ( $\text{Al}_2\text{O}_3$ )	45 $\mu\text{m}$	3.90	Eczacibası Esan Co.
Titanium dioxide ( $\text{TiO}_2$ )	50 $\mu\text{m}$	4.00	Sintas Plastic Co.
Fly ash	45 $\mu\text{m}$	2.00	Kutahya Cement Co.
Aluminium oxide ( $\text{Al}_2\text{O}_3$ )	40 nm	3.88	Grafen Chemia Co.
Titanium dioxide ( $\text{TiO}_2$ )	10 nm, anatase	3.90	Grafen Chemia Co.
Nanoclay (Montmorillonite modified with Trimethyl stearyl ammonium)	Nanomer 10 $\mu\text{m}$	1.90	Sigma Aldrich

### 2.2 Composite Preparation

In the composite material preparation process, the filler was dried in an oven at 70 °C for 4 h. The epoxy resin was heated in order to reduce viscosity before mixing. Fillers were then added into the resin and mixed using mechanical stirrer for 2 h. During this stage, vacuum processes were used to remove the entrapped air. After that, the hardener (Curing agent MGS LH 285) was added and mixed manually. The vacuum process was again applied. Afterwards, composite resin was poured into the open moulds. In the case of nano-filler, before the hardener was added, the resin was subjected to an ultrasonic method for 15 min. Finally, specimens in the moulds were tested at room conditions for 24 h, following which they were placed in an oven and heated at 60 °C for 15 h and 80 °C for 5 h for post-curing in order to cross-link.

### 3 RESULTS

Standard tensile tests were performed using a Shimadzu test machine with a crosshead speed of 5 mm/min at room temperature ( $23 \pm 1$  °C). The tensile strength value was determined according to the ASTM D638-10 standard [18]. The tensile strength, elastic modulus and strain [%] values were obtained and evaluated. Three-point bending tests were carried out using a Shimadzu test machine according to the ASTM D790-10 [19] standard. The test specimen dimensions were 3.2 mm × 12.7 mm × 127 mm and the test speed was 2 mm/min. Flexural strength, flexural modulus, and elongation at break values were obtained and evaluated.

Flexural stress was calculated according to Eq. (1):

$$\sigma = \frac{3FL}{2bd^2}, \quad (1)$$

where  $\sigma$  is the flexural stress [MPa],  $F$  is the load [N],  $L$  is the span [mm],  $b$  is the specimen width [mm] and  $d$  is the specimen thickness [mm].

Flexural modulus was calculated according to Eq. (2):

$$E_B = \frac{L^3 m}{4bd^3}, \quad (2)$$

where  $E_B$  is the flexural modulus [MPa],  $L$  is the span [mm],  $b$  is the specimen width [mm],  $d$  is the specimen

thickness [mm], and  $m$  is the slope of the linear region of the load-displacement curve.

Bending strain was calculated according to Eq. (3):

$$\varepsilon = \frac{6Dd}{L^2}, \quad (3)$$

where  $\varepsilon$  is the strain [mm/mm],  $D$  is the maximum displacement at the central point of the specimen,  $d$  is the specimen thickness [mm], and  $L$  is the span [mm].

Finally, the hardness test was carried out with a Barcol hardness tester according to the ASTM D2583-07 [20] standard.

All tests were repeated at least between 3 to 5 times, and the results were recorded and plotted, see Figs. 1 to 8.

Fig. 1 presents the relationship between the tensile strength and filler content of micro- and nano-epoxy composites. It is clear that the tensile strengths of micro-filled composites decreased with increasing filler content ratio. The results also show the reduced sensitivity of the strength of  $\text{Al}_2\text{O}_3$  filled composites to the change in filler content ratios. In the case of nano-filler, the strength is in an increase up to 2.5 % filler content. This increase is about 8 % and 12 % for nano- $\text{TiO}_2$  and nano- $\text{Al}_2\text{O}_3$ -filled composites, respectively. Beyond this ratio, there is some drop in the strength of the composite.

Fig. 2 shows the variation of tensile modulus of micro- and nano-filler composites with filler content. In this figure, the tensile modulus of epoxy composites

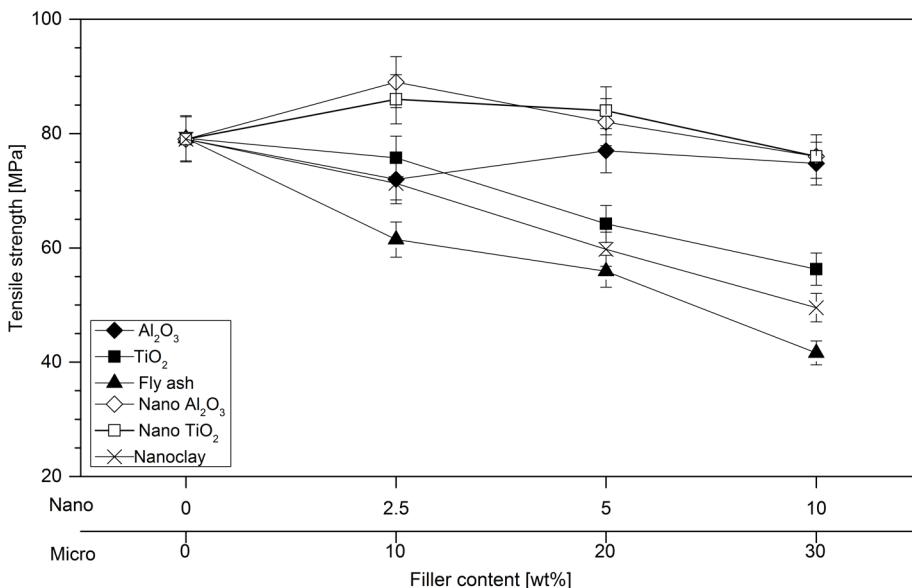


Fig. 1. The relationship of tensile strength against filler content of micro and nano epoxy composites

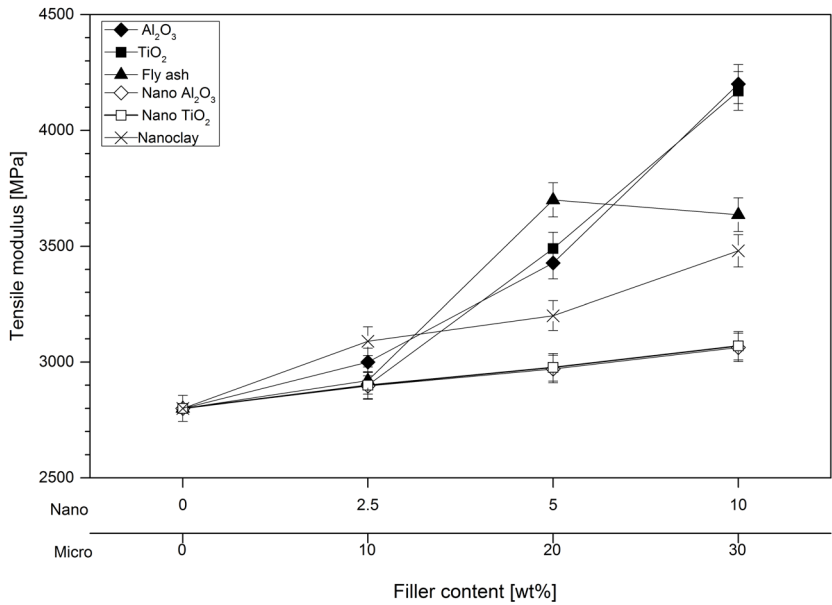


Fig. 2. The relationship of tensile modulus against filler content of micro and nano epoxy composites

increased with increasing filler content. Micro- and nano-fillers increased the polymer stiffness, and this increased its modulus. With a 200 % increase in filler content, there is a 50 % increase in the modulus for both Al<sub>2</sub>O<sub>3</sub>- and TiO<sub>2</sub>-filled epoxy composites. In the case of nano-fillers, for a 300 % increase in nano-filler content, the modulus of nano-Al<sub>2</sub>O<sub>3</sub>, nano-TiO<sub>2</sub> and nano-clay increased by 9 %, 9.6 %, and 24 %, respectively.

Fig. 3 presents the variation of elongation at break with filler content for micro- and nano-epoxy composites. It is clear from this figure that the elongation-at-break values decreased with increases of the filler content of the composite. The fillers gave the matrix the brittle behaviour. For a 200 % increase in micro-Al<sub>2</sub>O<sub>3</sub>, TiO<sub>2</sub> and fly ash filler content, the decreases in the elongation at break are 50 %, 66 %, and 65 %, respectively. For a 300 % increase

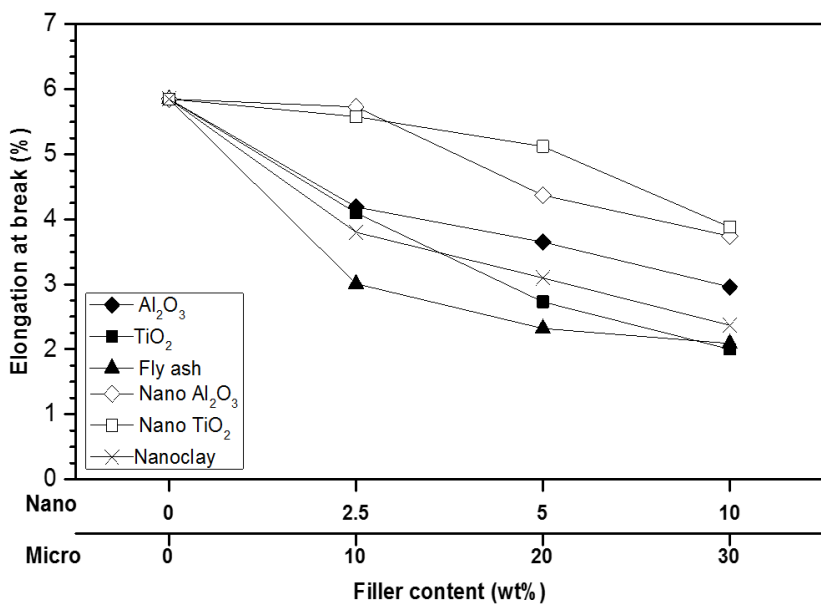


Fig. 3. The relationship of elongation at break against filler content of micro and nano epoxy composites

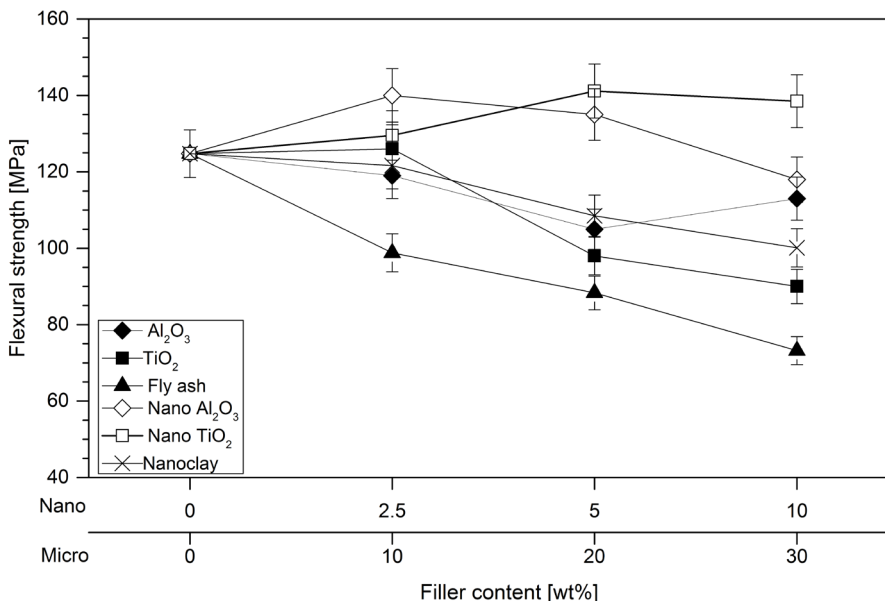


Fig. 4. The relationship of flexural strength against filler content of micro- and nano-epoxy composites

in nano-Al<sub>2</sub>O<sub>3</sub>, nano-TiO<sub>2</sub> and nano-clay content, the decreases in the elongation at break are 37 %, 34 %, and 60 %, respectively.

Fig. 4 shows the flexural strength against filler content curves of micro- and nano-epoxy composites. In this figure, the flexural strengths of micro-composites decreased with increasing filler content, and this decrease ranged between 12 % to 45 %. The nano-composites follow an increasing trend up to

2.5 % to 5 % ratios, and then a decreasing trend at higher filler ratios; 2.5 wt% filled nano Al<sub>2</sub>O<sub>3</sub> showed the highest increase at 12 %. The nano-TiO<sub>2</sub>-filled composite reaches a 13 % increase in flexural strength at 5 a wt% filled ratio. The nano-clay-filled composite follows a decreasing trend, and this decrease reaches 20 % at the 10 % filler ratio.

Fig. 5 shows the relationship between the flexural modulus filler content of micro- and nano-epoxy

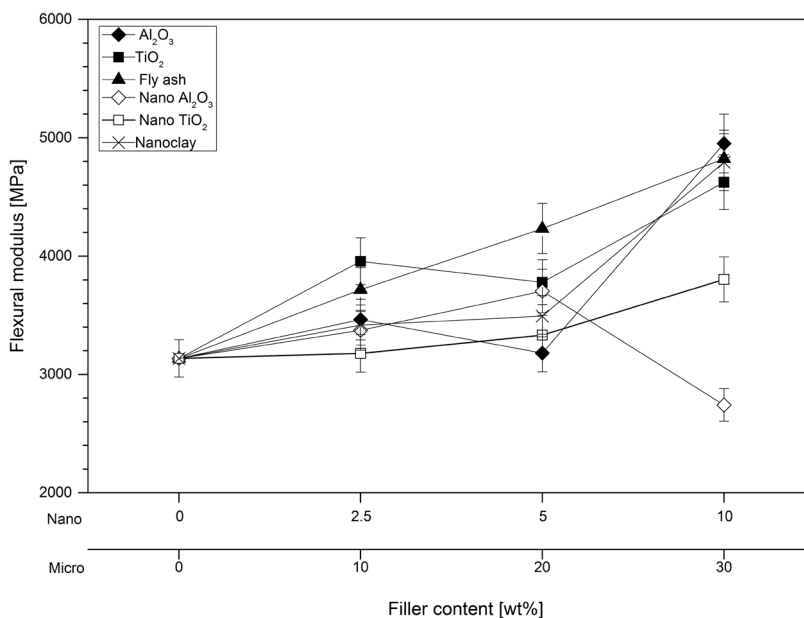


Fig. 5. The relationship of flexural modulus against filler content of micro and nano epoxy composites

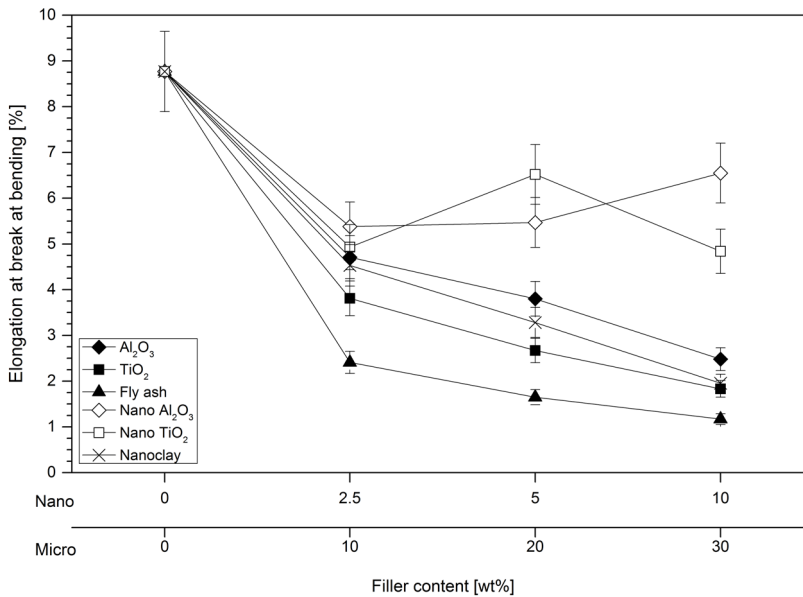


Fig. 6. The relationship of elongation at break at bending against filler content of micro and nano epoxy composites

composites. As the fillers increased the rigidity and stiffness behaviour in the polymer composite, the flexural modulus increased with the increasing filler content. The highest flexural modulus values were reached with 30 wt% micro-filler content composites. For a 200 % increase in micro Al<sub>2</sub>O<sub>3</sub>, TiO<sub>2</sub> and fly ash content, there are 57 %, 47 % and 53 % increases in the flexural modulus of the composite, respectively. For a 300 % increase in nano-filler content, there are 9 % and 45 % increases in nano-TiO<sub>2</sub> and nano-clay

epoxy composites flexural modulus, respectively. In the case of nano-Al<sub>2</sub>O<sub>3</sub>, there is an increasing and decreasing behaviour of 12 %.

Fig. 6 presents the variation of elongation at the break with filler content for micro- and nano-epoxy composites. As the presence of rigid fillers increased the matrix's brittle behaviour, which was reflected as reduced elongation at the break values of the materials, the figure shows that the minimum elongation at break values occurred at the maximum

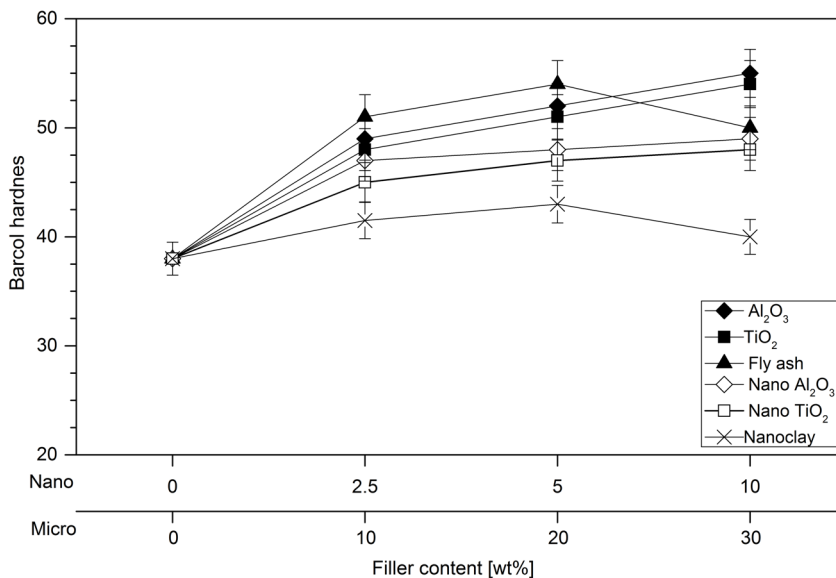
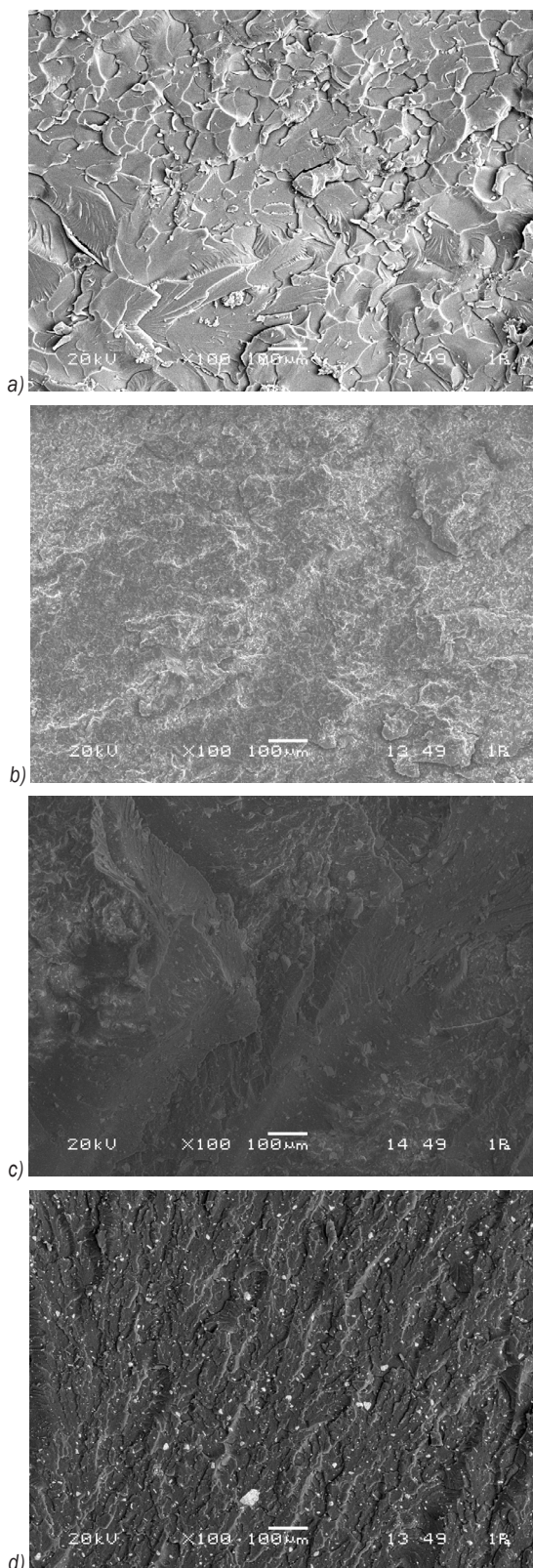


Fig. 7. The relationship of hardness against filler content of micro and nano epoxy composites



**Fig. 8.** Fracture surfaces of tensile test specimens, a) Pure epoxy, b) 20 wt%  $\text{Al}_2\text{O}_3$  filled, c) 20 wt%  $\text{TiO}_2$  filled, and d) 5 wt% nano  $\text{TiO}_2$  filled

filler ratio in the composites. For a 200 % increase in micro  $\text{Al}_2\text{O}_3$ ,  $\text{TiO}_2$  and fly ash filler content, there are decreases in the elongation at break values of 72 %, 80 %, and 87 %, respectively. In the case of nano-filler for a 300 % increase in filler content, there are 39 %, 45% and 78 % decreases in the elongation at break for nano- $\text{Al}_2\text{O}_3$ , nano- $\text{TiO}_2$ , and nano-clay composites, respectively.

Fig. 7 shows the variations in the hardness of micro- and nano-epoxy composites with filler content. It is clear that the hardness of the composites increased with increasing filler content. Again, the rigid fillers increased the hardness of the epoxy resin. Apart from fly ash and nano clay-filled epoxy composites, all composites followed an increasing profile with increasing filler content. There is an increase of 30 % to 50 % in hardness value with an increase of 200 % to 300 % in filler contents.

Fig. 8 shows the fracture surface of the tensile specimen for pure epoxy, 20 wt%  $\text{Al}_2\text{O}_3$ , 20 wt%  $\text{TiO}_2$  and 5 wt% nano- $\text{TiO}_2$  epoxy composites. It is clear that the filler-filled composites fracture is a brittle mechanism-type failure.

#### 4 DISCUSSIONS

It is clear from the results that the tensile strengths of micro-filled composites decreased with increasing filler content ratios. This could be explained as the increasing filler content caused the weak adhesion between matrix and fillers and led to the decrease of the strength of the epoxy composite. In the case of nano-filler, the drop in strength is due to the non-homogeneous distribution of fillers at high filler ratios, which led to the agglomeration and caused stress concentration regions, leading to some drop in the strength. The decrease in nano-clay-filled epoxy composite strength could be explained by the agglomeration problem even at low filler content ratios.

The drop in elongation at break values of the composite with filler content could be explained as the elastic properties of the composite depend on the polymer matrix, which shows brittle behaviour in the presence of the fillers. This is because these fillers restrict the mobility of the polymer, and the higher the filler content is, the higher the brittleness of the composite is.

The decrease in the flexural strength of the composites could be explained by the agglomeration of the nano-fillers at higher ratios and by the presence of weak adhesive between the filler and matrix materials at high micro-filler contents. The increase in

flexural modulus with the increasing filler content is because the fillers increased the rigidity and stiffness behaviour of the polymer composite.

In most cases, the filler increased the hardness of the composite. In the case of fly ash and nano-clay and a high filler content ratio, a small drop in hardness value was observed. This could be explained by the weakness in the adhesion between the epoxy matrix and filler materials. Lam et al. [4] explained that increasing the filler ratio caused the increasing cluster in the nano clay filled composite and a decrease in the hardness value of the epoxy composite.

In general, it is clear from Figs. 1 to 7 that the filler content has a significant effect and enhancement on most of the mechanical properties of epoxy composites but this is only effective up to certain filler ratio levels. In the case of micro-fillers, overly high levels of filler content cause a weakness in the adhesion force between the matrix and the filler, while high levels of nano-fillers show an agglomeration problem. Hence, a drop or weakness in the mechanical properties of the epoxy composite occurs.

## 5 CONCLUSIONS

From this study the following conclusions are reached:

- The tensile strength, flexural strength and elongation at break values of micro-filler  $Al_2O_3$ ,  $TiO_2$ , fly ash and nano-fillers  $Al_2O_3$ ,  $TiO_2$ , clay epoxy composites decreased with increasing filler ratio.
- The tensile modulus and flexural modulus of micro-filler  $Al_2O_3$ ,  $TiO_2$ , fly ash and nano-fillers  $Al_2O_3$ ,  $TiO_2$ , clay epoxy composites increased with increasing filler content.

In general, the hardness of the micro-filler  $Al_2O_3$ ,  $TiO_2$ , fly ash and nano-fillers  $Al_2O_3$ ,  $TiO_2$ , clay epoxy composites increased with increasing filler content.

- Epoxy composites showed brittle behaviour with the addition of the filler.
- The problem of the agglomeration of the filler is present at higher nano-filler ratios
- The results are in agreement with the results reached by [3], [4] and [13].

## 6 ACKNOWLEDGEMENT

This study was supported by the Sakarya University Scientific Research Projects Coordinatorship, with project no: 2010-50-02-004 and 2010-50-06-005.

## 7 REFERENCES

- [1] Zaman, H.U., Hun, P.D., Khan, R.H., Yoon, K.B. (2012). Morphology, mechanical, and crystallization behaviors of micro- and nano-ZnO filled polypropylene composites. *Journal of Reinforced Plastics and Composites*, vol. 31, no. 5, p. 323-329, DOI:10.1177/0731684411436126.
- [2] Gao, Y., Liu, L., Zhang, Z. (2009). Mechanical performance of nano- $CaCO_3$  filled polystyrene composites. *Acta Mechanica Solida Sinica*, vol. 22 no. 6, p. 555-562, DOI:10.1016/S0894-9166(09)60386-4.
- [3] Agubra, V.A., Owuor, P.S., Hosur, M.V., (2013). Influence of nanoclay dispersion methods on the mechanical behaviour of e-glass/epoxy nanocomposites. *Nanomaterials*, vol. 3, no. 3, 550-563, DOI:10.3390/nano3030550.
- [4] Lam, C.K., Cheung, H.Y., Lau, K.T., Zhou, L.M., Ho, M.W., Hui, D. (2005). Cluster size effect in hardness of nanoclay/epoxy composites. *Composites: Part B: Engineering*, vol. 36, no. 3, p. 263-269, DOI:10.1016/j.compositesb.2004.09.006.
- [5] Yasmin, A., Daniel, I.M. (2004). Mechanical and thermal properties of graphite platelet/epoxy composites. *Polymer*, vol. 45, no. 24, p. 8211-8219, DOI:10.1016/j.polymer.2004.09.054.
- [6] Sayer, M., (2014). Elastic properties and buckling load evaluation of ceramic particles filled glass/epoxy composites. *Composites Part B: Engineering*, vol. 59, p. 12-20, DOI:10.1016/j.compositesb.2013.11.016.
- [7] Asi, O. (2009). Mechanical properties of glass-fiber reinforced epoxy composites filled with  $Al_2O_3$  particles. *Journal of Reinforced Plastics and Composites*, vol. 28, no. 23, p. 2861-2867, DOI:10.1177/0731684408093975.
- [8] Yang, H.S., Kim, H.J., Son, J., Park, H.J., Lee, B.J., Hwang, T.S. (2004). Rice-husk flour filled polypropylene composites; mechanical and morphological study. *Composite Structures*, vol. 63, no. 3-4, p. 305-312, DOI:10.1016/S0263-8223(03)00179-X.
- [9] Ibrahim, M.S., Sapuan, S.M., Faieza, A.A. (2012). Mechanical and thermal properties of composites from unsaturated polyester filled with oil palm ash. *Journal of Mechanical Engineering and Sciences*, vol. 2, p. 133-147, DOI:10.15282/jmes.2.2012.1.0012.
- [10] Li, M.C., Zhang, Y., Cho, U.R. (2014). Mechanical, thermal and friction properties of rice bran carbon/nitrile rubber composites: Influence of particle size and loading. *Materials & Design*, vol. 63, p. 565-574, DOI:10.1016/j.matdes.2014.06.032.
- [11] Imoisili, P.E., Ezenwafor, T. C., AttahDaniel, B. E., Olusunle, S.O.O. (2013). Mechanical properties of cocoa-pod/epoxy composite; effect of filler fraction. *American Chemical Science Journal*, vol. 3, no. 4, p. 526-531, DOI:10.9734/ACSJ/2013/5526.
- [12] Ray, D., Bhattacharya, D., Mohanty, A.K., Drzal, L.T., Misra, M. (2006). Static and dynamic mechanical properties of vinyl ester resin matrix composites filled with fly ash. *Macromolecular Materials and Engineering*, vol. 291, no. 7, p. 784-792, DOI:10.1002/mame.200600097.
- [13] Raja, R.S., Manisekar, K., Manikandan, V. (2014). Study on mechanical properties of fly ash impregnated glass fiber

reinforced polymer composites using mixture design analysis. *Materials & Design*, vol. 55, p. 499-508, DOI:0.1016/j.matdes.2013.10.026.

- [14] Chauhan, S.R., Thakur, S., (2013) Effects of particle size, particle loading and sliding distance on the friction and wear properties of cenosphere particulate filled vinylester composites. *Materials & Design*, vol. 51, p. 398-408, DOI:10.1016/j.matdes.2013.03.071.
- [15] Prakash, A.M., Kumar, G.S., Sandeep, N., Ravikumar, K. (2015). A Review on ceria epoxy nanocomposites with a new research proposal. *IOSR Journal of Mechanical and Civil Engineering*, vol. 12, no. 3, p. 1-3.
- [16] Manjunath, M., Renukappa, N.M., Suresha, B. (2015). Influence of micro and nanofillers on mechanical properties of pultruded unidirectional glass fiber reinforced epoxy composite systems. *Journal of Composite Materials*, in press, DOI:10.1177/0021998315588623.
- [17] Sudheer, M., Prabhu, R., Raju, K., Bhat T. (2014). Effect of filler content on the performance of epoxy/PTW composites. *Advances in Materials Science and Engineering*, Article ID 970468, DOI:10.1155/2014/970468.
- [18] ASTM D638-10(2010). *Standard Test Method for Tensile Properties of Plastics*. American Society for Testing and Materials, West Conshohocken, DOI:10.1520/D0638-14.
- [19] ASTM D790-10(2010). *Standard Test Methods for Flexural Properties of Unreinforced and Reinforced Plastics and Electrical Insulating Materials*. American Society for Testing and Materials, West Conshohocken, DOI:10.1520/D0790-10.
- [20] ASTM D2583-07 (2007). *Standard Test Method for Indentation Hardness of Rigid Plastics by Means of a Barcol Impressor*. American Society for Testing and Materials, West Conshohocken, DOI:10.1520/D2583-07.

# Prediction of the True Stress of ZE20 Magnesium Alloy at Different Temperatures and Strain Rates

Sedat Bingöl<sup>1,\*</sup> – Wojciech Misiolek<sup>2</sup>

<sup>1</sup> Dicle University, Department of Mechanical Engineering, Turkey

<sup>2</sup> Institute for Metal Forming, Lehigh University, USA

Compression tests were performed to obtain flow stress curves of a newly developed magnesium ZE20 alloy for automobile applications. The experiments were performed in a temperature range from 200 °C to 425 °C and the strain rates from 0.01 to 15 s<sup>-1</sup> to examine the material responses at various processing conditions. Artificial neural network (ANN) and gene expressing programming (GEP) were used for the estimation of the true stress curves obtained from the experimental tests. Recently, a few studies were performed to estimate the true stress of different magnesium alloys by using ANN modelling method. However, this method has not yet been applied for the ZE20 alloy; therefore, it was the subject in this study. Furthermore, this study is the first attempt of using a GEP model to predict the true stress of a magnesium alloy. Both developed ANN and GEP models successfully predicted the true stress of ZE20 alloy.

**Keywords:** magnesium, ZE20, compression, true stress, GEP, ANN, prediction

## Highlights

- The compression tests were performed to obtain the flow stress curves of a newly developed magnesium ZE20 alloy for automobile applications.
- An artificial neural network (ANN) and gene expressing programming (GEP) were used for the estimation of the true stress curves obtained from the experimental tests.
- Good agreement between predicted and experimental true stress results was obtained for ZE20 alloy using both ANN and GEP models.
- An equation was derived from the developed GEP model which is simple and can easily be used for further true stress predictions of the ZE20 alloy.

## 0 INTRODUCTION

In response to increasing energy and resource consumption in the automotive industry, designers have recently become more interested in lightweight alternatives to common materials. Strong expectations exist that the automotive industry will begin using magnesium alloys in the production of numerous components due to their high strength/weight ratio.

Most magnesium products in the automotive industry are manufactured via high pressure die casting (HPDC); such products include engine blocks and heads, transmission housings, and other small components [1]. Designers are searching for new ways of building automobiles with reduced harmful environmental impact. Reducing the weight of automobiles is an important opportunity for reducing fuel consumption. Therefore, the share of wrought magnesium alloys needs to improve. Although these alloys have better mechanical properties than cast magnesium alloys, they have had limited usage until now due to deformation limitations.

In the recent literature, many studies focus on the deformation processing of wrought Mg alloys. Li et al. [2] performed compression tests to determine a

basic relationship for a wrought magnesium alloy with a wide range of strain rates; the results showed that the flow curve reaches a steady state at low strain values. Mishra et al. [3] encountered an abnormal change in the behaviour of Mg due to the addition of Ce. Luo et al. [4] studied high ductility magnesium-zinc-cerium extrusion alloys. Their studies showed that by adding a small amount of zinc, the strength of the Mg-Ce alloy can be improved notably. Luo et al. [5] also examined the microstructure and mechanical properties of extruded magnesium alloy tubes; the results revealed that the mechanical properties can be improved with the addition of Ce to pure magnesium. Chino et al. [6] investigated the compressive properties of Mg alloys from room temperature up to 500 °C to understand the effects of Ce on the deformation process; the results showed that the addition of Ce increased the ductility of Mg alloy at room temperature, but decreased it at 300 °C. El-Morsy et al. [7] investigated the microstructural evolution of AZ61. They achieved fine grain size via a combination of hot extrusion and thermomechanical processing.

In light of the literature survey, it can be said that a significant part of the current research and development projects on magnesium alloys and their

use in the automotive industry is generally focused on wrought magnesium alloys. The reason for this is the fact that the average usage of magnesium alloys in automobiles today is low and, therefore, there is great potential for its increase.

The prediction of metal behaviour based on nature-inspired computational techniques, such as artificial neural networks (ANN), are attracting considerable interest from researchers. ANNs offer a good and fast alternative to conventional methods for predictive modelling [8] and [9]. Regarding the application of ANN modelling to metal forming, Li et al. [10] showed that ANNs can be used to predict the tensile strength of extrusion tubes. Zhou et al. [11] used ANN to predict the extrusion load and exit temperature for AZ31B magnesium alloy. Bingol et al.

[12] predicted the extrusion load of gear like profiles for different extrusion dies by ANN. Ayer et al. [13] performed an ANN modelling for lateral extrusion load estimation. The results they obtained were in good agreement with the experimental results. Toros and Ozturk [14] developed an ANN modelling to analyze the material flow curves of strain-hardened magnesium alloys. Sabokpa et al. [15] suggested an ANN model for the prediction of the flow behaviour of AZ81 magnesium alloy. In another study, Qin et al. [16] predicted the deformation behaviour of ZK60 by ANN. Djavanroodi et al. [17] successfully used ANN modelling for die design in equal-channel angular pressing.

Another artificial intelligence (AI) technique, gene-expressing programming, which is a new

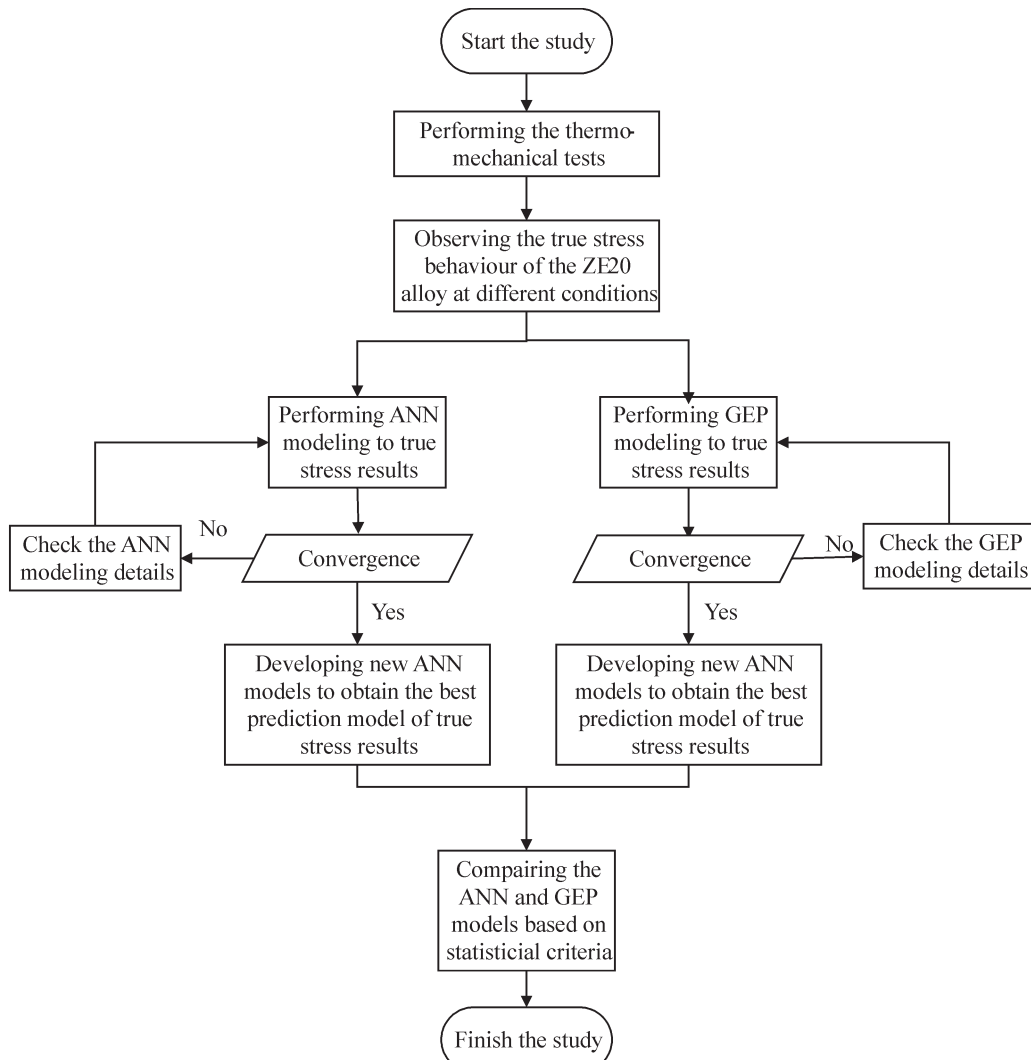


Fig. 1. Framework of this study

evolutionary algorithm developed by Ferreira [18], has been used in different engineering areas [19]. Several gene-expressing programming (GEP) approaches have been conducted and reported in the literature, but it is important to note that a predictive GEP model for the deformation behaviour of a magnesium alloy has not been reported in literature and is the subject of this study. In the current study, the formability of the ZE20 magnesium alloy, which was recently developed by General Motors [4] and [5], was studied. After compression tests of the alloy, the ANN and GEP models were developed to predict the true stress curves of the alloy. The capability of the developed models has been evaluated using statistical measurement criteria such as the coefficient of determination ( $R^2$ ), mean square error (MSE) and mean absolute error (MAE).

## 1 METHODOLOGY

The study was conducted in two phases: in the first, the thermo-mechanical tests were performed to obtain the flow stress curves for ZE20 magnesium alloy. In the second, the ANN and GEP models were developed to predict the true stress curves of ZE20 alloy. Finally, the best ANN and GEP models developed have been compared. The framework of the study can be seen in Fig. 1.

### 1.1 Experimental Study

A new magnesium alloy, ZE20 (Mg – 2 wt.% Zn – 0.2 wt.% Ce), was deformed to observe the resulting true stress behaviour. The detailed results of the physical modelling are reported in the literature [20]. The accuracy of the ANN and GEP models performed in this part of the study depends strictly on the quality of the input data regarding the physical properties of the material. To build the ANN and GEP models of the ZE20 alloy, the data on true stress versus temperature, true strain, and strain rate have to be introduced into the models. To obtain these data for the performed study, uniaxial compression tests were performed at temperatures of 200 °C, 375 °C and 425 °C and strain rates of 0.01 s<sup>-1</sup>, 5 s<sup>-1</sup> and 15 s<sup>-1</sup>. The experiments for the hot workability analysis were conducted on a Gleeble 3500 using the specimens with a diameter of 8 mm and a height of 12 mm.

### 1.2 Development of ANN Model

ANN is a computational structure made up of a number of simple, highly interconnected processing

elements that can learn from observing data sets. ANNs can capture many types of relationships that otherwise may have been very challenging to explain. Therefore, researchers attempted to apply ANN to some complicated engineering problems. ANNs have three layers that are interconnected. The first layer is made up of a set of input nodes that contain an activation function. Those nodes transfer data to the second layer which in turn sends the outputs to the third layer. Neurons in each layer behave as independent processing elements. After training the network using a special learning function, a set of data that has not been trained is used for the testing and validation of the networks. This process is repeated until a minimal error in the entire procedure is obtained [21]. Different learning rules can be used in order to improve the ANNs' performance. Back propagation is a common algorithm for training the ANNs since it has the advantages of being very simple and accurate. After the network is initialized with random weights, the method updates the weights to match the required output. Weight updating repeats until the loss function is minimized.

This study takes into consideration three input parameters: two of them, temperature and strain rate, represent the compression test conditions and one of them, true strain ( $\epsilon$ ), represents the result of the true stress for each temperature ( $T$ ) and strain rate ( $\dot{\epsilon}$ ). The output layer consists of one neuron, which represents the true stress of the ZE20 alloy. A transfer function is required to translate the input signals to output signals. In this study, a TanhAxon transfer function was used to introduce nonlinearity into the network. An ANN structure with feed-forward neural networks was used for estimating the true stress of the ZE20 alloy in compression tests. The total experimental data (657 samples) was randomized and divided into two categories, named training subsets (80 %) and testing subsets (20 %). The ideal transfer function and the number of neurons and hidden layers should be found through a trial-and-error method. In the selection of best network structure, measurements ( $R^2$ , RMSE, MAE) were used as the performance criteria between the ANN predicted and the experimental true stress of ZE20. After several trials of the ANN structure, the optimal neural network structure was determined with the Levenberg-Marquardt back-propagation algorithm, TanhAxon transfer function, and 6 neurons in one hidden layer. Fig. 2 shows the structure of the feed-forward ANN model used.

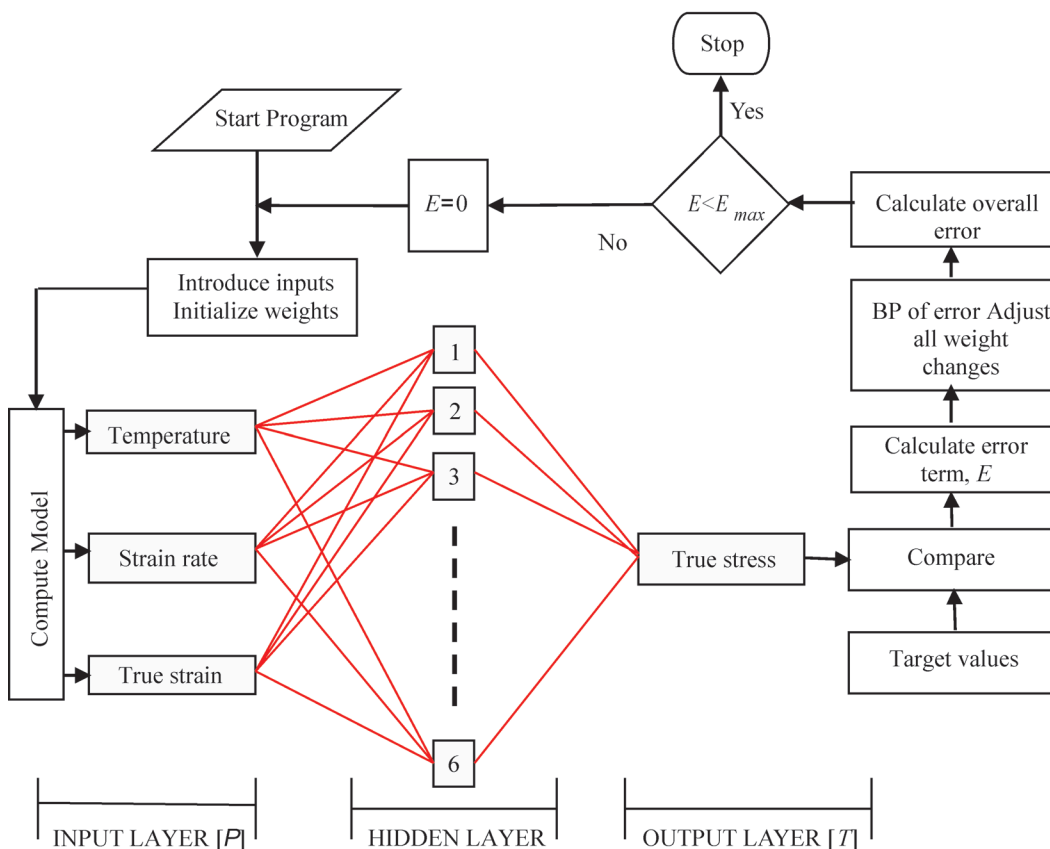


Fig. 2. Framework of this study

1.2 Development of GEP Model

Another AI technique, GEP, which is also used in this study, is an evolutionary algorithm that is capable of discovering functions from large data sets by evolving computer programs. These programs act much like a living organism. They can learn and adapt by changing their sizes and shapes. Evolution of the population takes place after selecting a population of individual by means of the genetic operators. Once a satisfactory fitness level is achieved, the algorithm terminates. The predicted values are compared with the actual ones until a minimal error is obtained. This process is repeated until an acceptable solution is achieved. There are two major elements of GEP: expression trees (ETs) and chromosomes. The chromosome symbolizes a mathematical expression and contains one or more genes. These genes consist of two components, the tail, and the head. After converting each chromosome into an ET, a mathematical equation is derived.

Table 1. Parameters of the optimized GEP model

Parameter	Description of parameter	Setting of parameter
P <sub>1</sub>	Chromosomes	30
P <sub>2</sub>	Fitness function error type	RRSE
P <sub>3</sub>	Number of the genes	3
P <sub>4</sub>	Head size	7
P <sub>5</sub>	Linking function	+
P <sub>6</sub>	Function set	+, -, ×, /, √, x <sup>2</sup> , x <sup>3</sup> , x <sup>1/3</sup> , ln, 1/x
P <sub>7</sub>	Mutation rate	0.044
P <sub>8</sub>	One-point recombination rate	0.3
P <sub>9</sub>	Two-point recombination rate	0.3
P <sub>10</sub>	Inversion rate	0.1
P <sub>11</sub>	Transposition rate	0.1

The aim of GEP models performed in this study was to develop a mathematical formulation that predicts the true stress of ZE20 alloy. The input parameters and the total data used for the developed GEP models were the same as the ones used in the

ANN models. Different numbers of chromosomes, genes, and head sizes affect the performance of the GEP model. Therefore, their number was varied to obtain the ideal GEP model. The number of chromosomes was varied between 10 and 40, the number of genes between 2 and 7 and the head sizes between 5 and 9. Parameters of the ideal GEP model can be seen in Table 1.

Furthermore, true stress prediction equations for the best GEP model were obtained.

Fig. 3 shows the ET of the formulation of the true stress, which is:

$$\begin{aligned}
 \text{dblTemp} &= (((d[0] \times d[2]) - \text{pow}(G1c0,3)) - \\
 &\quad - (G1c1 / d[0])) \times d[2]); \\
 \text{dblTemp} &+= (G2c0 - ((\text{pow}(G2c1,3) + \\
 &\quad + (d[1] + G2c0)) \times d[2])); \\
 \text{dblTemp} &+= (G3c1 \times ((\log(d[0]) + \\
 &\quad + (d[0] + G3c0)) - (d[2] \times d[1])));
 \end{aligned}
 \tag{2}$$

The real parameters in the derived GEP formulation are  $d[0] = \dot{\varepsilon}$ ,  $d[1] = T$  and  $d[2] = \varepsilon$ . Constants and coefficients in the Eq. (1) are  $G1c0 = -9.568298$ ,  $G1c1 = 2.070037$ ,  $G2c0 = 9.993287$ ,  $G2c1 = 8.020996$ ,  $G3c0 = 9.602448$  and  $G3c1 = 1.652527$ . After placing the real values, the equation becomes:

$$\begin{aligned}
 \sigma &= \left( \dot{\varepsilon} \varepsilon + 9.57^3 - \frac{2.07}{\dot{\varepsilon}} \right) \varepsilon + 9.99 - \\
 &\quad - (-8.02^3 + T + 9.99) \varepsilon + 1.65 (\ln \dot{\varepsilon} + \dot{\varepsilon} + 9.6 - \varepsilon T).
 \end{aligned}
 \tag{3}$$

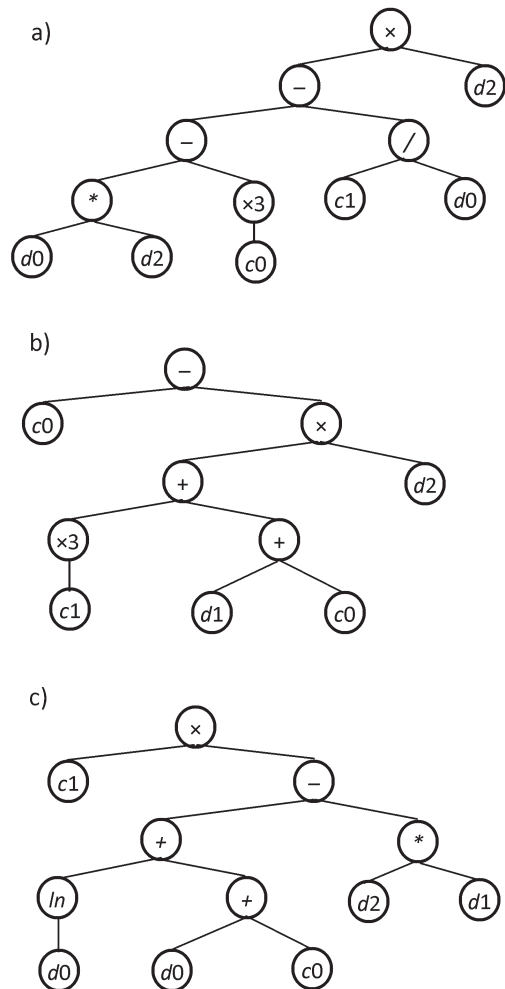


Fig. 3. Expression tree (ET) with three genes of the best GEP model (Model 9); a) sub-ET 1, b) sub-ET 2, and c) sub-ET 3

Table 2. Performed GEP (with different mathematical and linking functions) and ANN models for the prediction of true stress of ZE20 alloy

GEP Models	Linking Function	Mathematical functions	RMSE	MAE	R <sup>2</sup>	
M1	Addition	+, -, x, /, √, x <sup>2</sup> , x <sup>3</sup> , x <sup>1/3</sup> , ln	22.52	19.14	0.98	
M2	Addition	+, -, x, /, √, x <sup>2</sup> , x <sup>3</sup> , x <sup>1/3</sup> , 1/x	17.43	14.68	0.99	
M3	Addition	+, -, x, /, √, x <sup>2</sup> , x <sup>3</sup> , x <sup>1/3</sup> , ln, 1/x, (-x)	21.71	17.18	0.98	
M4	Addition	+, -, x, /, √, x <sup>2</sup> , x <sup>3</sup> , x <sup>1/3</sup> , ln, 1/x, abs	34.04	25.52	0.96	
M5	Addition	+, -, x, /, √, x <sup>2</sup> , x <sup>3</sup> , x <sup>4</sup> , x <sup>1/4</sup> , x <sup>1/3</sup> , ln, 1/x	12.68	10.08	0.99	
M6	Addition	+, -, x, /, √, x <sup>2</sup> , x <sup>3</sup> , x <sup>1/3</sup> , ln, exp	15.42	11.14	0.99	
M8	Addition	+, -, x, /, √, x <sup>2</sup> , x <sup>3</sup> , x <sup>1/3</sup> , ln, exp, 1/x, log	47.25	32.99	0.93	
M9	Addition	+, -, x, /, √, x <sup>2</sup> , x <sup>3</sup> , x <sup>1/3</sup> , ln, 1/x	8.48	6.81	0.99	
M10	Multiplication	+, -, x, /, √, x <sup>2</sup> , x <sup>3</sup> , x <sup>1/3</sup> , ln, 1/x	17.3	12.13	0.99	
ANN Models	Algorithm	Transfer function	Structure	RMSE	MAE	R <sup>2</sup>
M1	LM	TanhAxon	1-6	3.12	2.17	0.99
M2	Momentum	TanhAxon	1-12	26.24	20.73	0.95
M3	LM	Sigmoid	1-6	18.09	6.17	0.97
M4	Momentum	Sigmoid	1-6	100.31	77.84	0.68
M5	LM	TanhAxon	2-12	14.91	3.25	0.98

2 RESULTS AND DISCUSSION

Fig. 4 shows the true stress vs the true strain curves for the ZE20 alloy. The temperatures were selected as 200 °C, 375 °C, and 425 °C, and the strain rates

were selected as 0.01 s<sup>-1</sup>, 5 s<sup>-1</sup>, and 15 s<sup>-1</sup>. It is well known that while the strain rate is increasing during forming, higher stress is required to deform material to the same strain. The integral of the flow stress diagram represents input energy and the term energy

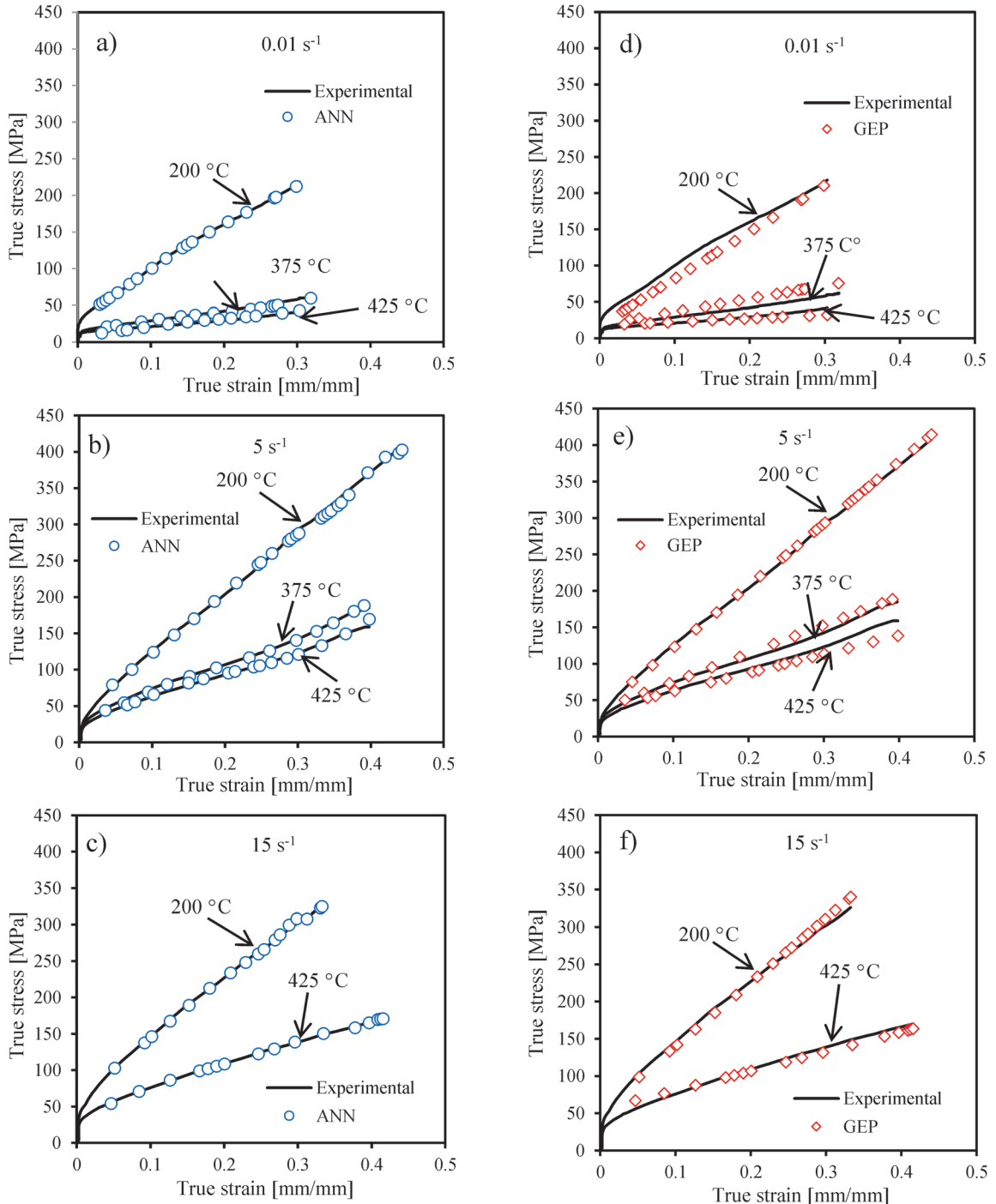


**Fig. 4.** Comparison between predicted (with ANN and GEP) and experimental true stress; a, b and c) experimental vs ANN at 0.01 s<sup>-1</sup>, 5 s<sup>-1</sup> and 15 s<sup>-1</sup>, respectively, d, e and f) experimental vs GEP at 0.01 s<sup>-1</sup>, 5 s<sup>-1</sup> and 15 s<sup>-1</sup>, respectively

is inversely dependent on time. More energy is needed to complete the same amount of deformation for a shorter time. It can be seen from Fig. 4 that the true stress increases with increasing strain rate at a true strain value. However, it must be noted that higher maximum true strain values occurred at lower strain rates. This demonstrates the dependence of material ductility on strain rate. Contrary to strain rate, the necessary deformation stress decreases with increasing temperature.

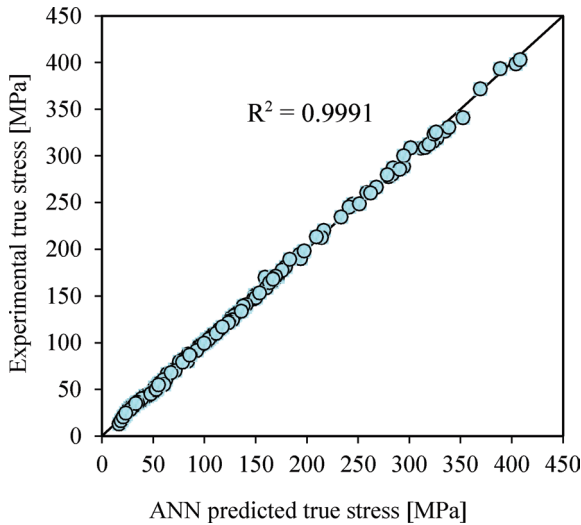


Fig. 5. Comparison between ANN predicted and experimental true stress of ZE20

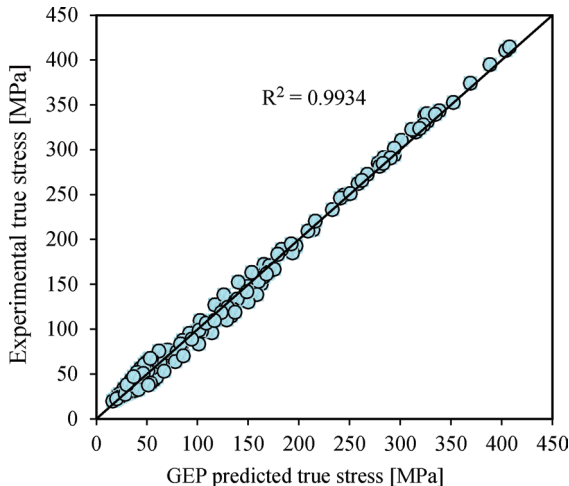


Fig. 6. Comparison between GEP predicted and experimental true stress of ZE20

The accuracy of the developed ANN and GEP models to predict the results of the compressions tests was evaluated using statistical measurement criteria ( $R^2$ , MSE, MAE), which can be seen in Table 2. Both models' predictions do match well with the

experimental results. It is accepted that an obtained result of  $R > 0.8$  with the prediction model indicates that the estimated results agree well with the measured values [22]. In this study, higher values of  $R^2$  were obtained by a number of developed GEP and ANN models. Among them, the best GEP model is Model 9, while the best ANN model is Model 1 (See Table 2). A very high  $R^2$  value (approximately 0.99) was obtained by these two models. Taking the other performance criteria into consideration, RMSE of 3.12 MPa and 8.48 MPa, and MAE of 2.17 MPa and 6.81 MPa were obtained for the developed ANN (Model 1) and GEP (Model 9) models, respectively. These reasonable results show that the developed models are efficient to be used to predict the true stress of the ZE20 alloy. Fig. 4 also graphically compares the experimental true stress with the best ANN and GEP predicted true stresses. As previously mentioned, the higher  $R^2$  and lower MAE and RMSE give better agreement between the actual and the predicted results. In this respect, it can be seen from Table 2 that the developed ANN model is slightly better than the developed GEP model at predicting the true stress of the ZE20 alloy. Figs. 5 and 6 also support the results seen in Table 2 that the deviations around the regression lines are smaller for the ANN models.

### 3 CONCLUSIONS

Compression tests of ZE20 magnesium alloy were performed under different deformation conditions using a Gleeble thermo-mechanical simulator. The results of the experimental tests were used to develop the best ANN and the GEP model. The conclusions were summarized as follows:

- Good agreement between predicted and experimental true stress results were obtained for a ZE20 alloy using both ANN and GEP models in terms of higher  $R^2$  and lower RMSE and MAE values.  $R^2$  of 0.99 and 0.99, RMSE of 3.12 MPa and 8.48 MPa, and MAE of 2.17 MPa and 6.81 MPa were obtained for the developed best ANN and GEP models, respectively
- The derived equation by the developed GEP model in this study is simple and can easily be used for further true stress predictions of the ZE20 alloy.
- The GEP model was capable of estimating the true stress of ZE20 magnesium alloy with high accuracy. However, the developed ANN model was slightly more successful than the GEP model.

## 4 ACKNOWLEDGEMENTS

The authors would like to acknowledge the partial financial support for this study from the United States Automotive Materials Partnership (cooperative agreement 07-1864). The authors would also like to thank The Scientific and Technological Research Council of Turkey for supporting the visit to Lehigh University and appreciate the financial support of the Loewy Family Foundation through the Loewy Professorship at Lehigh University.

This material is based in part upon work supported by the Department of Energy National Energy Technology Laboratory under Award Number DE-EE0003583. This report was prepared as an account of work sponsored by an agency of the United States Government.

## 5 REFERENCES

- [1] Zhang, H., Yan, Q., Li, L. (2008). Microstructures and tensile properties of AZ31 magnesium alloy by continuous extrusion forming process. *Materials Science and Engineering: A*, vol. 486, no. 1-2, p.295-299, DOI:10.1016/j.msea.2007.09.001.
- [2] Li, L., Zhou, J., Duszczek, J. (2006). Determination of a constitutive relationship for AZ31B magnesium alloy and validation through comparison between simulated and real extrusion. *Journal of Materials Processing Technology*, vol. 172, no. 3, p. 372-380, DOI:10.1016/j.msea.2007.09.001.
- [3] Mishra, R.K., Gupta, A.K., Rao, P.R., Sachdev, A.K., Kumar, A.M., Luo, A.A. (2008). Influence of cerium on the texture and ductility of magnesium extrusions. *Scripta Materialia*, vol. 59, no. 5, p. 562-565, DOI:10.1016/j.scriptamat.2008.05.019.
- [4] Luo, A.A., Mishra, R.K., Sachdev, A.K. (2011). High-ductility magnesium-zinc-cerium extrusion alloys. *Scripta Materialia*, vol. 64, no. 5, p. 410-413, DOI:10.1016/j.scriptamat.2010.10.045.
- [5] Luo, A.A., Wu, W., Mishra, R.K., Jin, L., Sachdev, A.K., Ding, W. (2010). Microstructure and mechanical properties of extruded magnesium-aluminum-cerium alloy tubes. *Metallurgical and Materials Transactions A*, vol. 41, no. 10, p. 2662-2674, DOI:10.1007/s11661-010-0278-3.
- [6] Chino, Y., Kado, M., Mabuchi, M. (2008). Compressive deformation behaviour at room temperature - 773 K in Mg - 0.2 mass % (0.035 at. %) Ce alloy. *Acta Materialia*, vol. 56, no. 3, p. 387-394, DOI:10.1016/j.actamat.2007.09.036.
- [7] El-Morsy, A., Ismail, A., Waly, M. (2008). Microstructural and mechanical properties evolution of magnesium AZ61 alloy processed through a combination of extrusion and thermomechanical processes. *Materials Science and Engineering: A*, vol. 486, no. 1-2, p. 528-533, DOI:10.1016/j.actamat.2007.09.036.
- [8] Hagan, M.T., Demuth, H.B., Beale, M.H. (1996). *Neural Network Design*. PWS Publishing, Boston.
- [9] Patterson, D.W. (1995). *Artificial Neural Network Theory and Application*. Prentice Hall, New York.
- [10] Li, L., Zhang, H., Zhou, J., Duszczek, J., Li, G.Y., Zhong, Z.H. (2008). Numerical and experimental study on the extrusion through a porthole dies to produce a hollow magnesium profile with longitudinal weld seams. *Materials & Design*, vol. 29, no. 6, p. 1190-1198, DOI:10.1007/s00521-013-1532-6.
- [11] Zhou, J., Li, L., Mo, J., Zhou, J., Duszczek, J. (2010). Prediction of the extrusion load and exit temperature using artificial neural networks based on FEM simulation. *Key Engineering Materials*, vol. 424, p. 241-248, DOI:10.4028/www.scientific.net/KEM.424.241.
- [12] Bingol, S., Ayer, O., Altinbalik, T. (2015). Extrusion load prediction of gear-like profile for different die geometries using ANN and FEM with experimental verification. *The International Journal of Advanced Manufacturing Technology*, vol. 76, no. 5, p. 983-992, DOI:10.1007/s00170-014-6328-z.
- [13] Ayer, O., Bingol, S., Altinbalik, T. (2015). Artificial neural network modelling of injection upsetting load. *Applied Mechanics and Materials*, vol. 729, p. 155-160, DOI:10.4028/www.scientific.net/AMM.729.155.
- [14] Toros, S., Ozturk, F. (2011). Flow curve prediction of Al-Mg alloys under warm forming conditions at various strain rates by ANN. *Applied Soft Computing*, vol. 11, no. 2, p. 1891-1898, DOI:10.1016/j.asoc.2010.06.004.
- [15] Sabokpa, O., Zarei-Hanzaki, A., Abedi, H.R., Haghdadi, N. (2012). Artificial neural network modelling to predict the high temperature flow behaviour of an AZ81 magnesium alloy. *Materials and Design*, vol. 39, p. 390-396, DOI:10.1016/j.matdes.2012.03.002.
- [16] Qin, Y.J., Pan, Q.L., He, Y.B., Li, W.B., Liu, X.Y., Fan, X. (2010). Artificial neural network modelling to evaluate and predict the deformation behaviour of ZK60 magnesium alloy during hot compression. *Materials and Manufacturing Processes*, vol. 25, no. 7, p. 539-545, DOI:10.1080/10426910903124894.
- [17] Djavanroodi, F., Omranpour, B., Sedighi, M. (2013). Artificial Neural Network Modeling of ECAP Process. *Materials and Manufacturing Processes*, vol. 28, no. 3, p. 276-281, DOI:10.1080/10426914.2012.667889.
- [18] Ferreira, C. (2011). Gene expression programming: A new adaptive algorithm for solving problems. *Complex Systems*, vol. 13, no. 2, p. 87-129.
- [19] Dikmen, E. (2014). Gene expression programming strategy for estimation performance of LiBr-H<sub>2</sub>O absorption cooling system. *Neural Computing and Applications*, vol. 26, no. 2, p. 409-415, DOI:10.1007/s00521-014-1723-9.
- [20] Thome, A.J., Misiolek, W.Z., Luo, A.A. (2012). Workability evaluation of new Mg-Zn-Ce alloys. *9th International Conference on Magnesium Alloys and Their Applications*, Poole, W.J., Kainer, K.U. (eds.), p. 703-708.
- [21] Patterson, J.M. (1997). *Introduction to Artificial Neural Systems*, 2<sup>nd</sup> ed. Jaico Publishing House, New Delhi.
- [22] Smith, G.N. (1986). *Probability and Statistics in Civil Engineering*, Collins, London.



# Vsebina

## Strojniški vestnik - Journal of Mechanical Engineering

letnik 61, (2015), številka 10

Ljubljana, oktober 2015

ISSN 0039-2480

Izhaja mesečno

### Razširjeni povzetki

- Peter Šteblaj, Mirko Čudina, Primož Lipar, Jurij Prezelj: Glušnik z adaptivnimi akustičnimi lastnostmi SI 103
- Om Prakash Singh, Rohit Raut, Mrinmoy Biswas, Ramji Singh: Vpliv dinamičnih zračnikov na toplotno ugodje v avtomobilu SI 104
- Livia Dana Beju, Paul Dan Brindasu, Silvia Vulc: Brušenje volframovega karbida pri izdelavi topovskih svedrov SI 105
- Paolo Casoli, Nicola Pompini, Luca Riccò: Simulacija hidravličnega sistema bagra z nelinearnimi matematičnimi modeli SI 106
- Mohammadreza Saffarian, Moona Mohammadi, Mohammadreza Mohammadi: Potenčni model pretoka nenevtonske tekočine s strižno odvisnim upadanjem viskoznosti skozi kanal z oviro SI 107
- Iskender Ozsoy, Askin Demirkol, Abdullah Mimaroglu, Huseyin Unal, Zafer Demir: Vpliv vsebnosti mikro- in nanoplnil na mehanske lastnosti epoksi kompozitov SI 108
- Sedat Bingöl, Wojciech Misiolek: Napovedovanje dejanskih napetosti v magnezijevi zlitini ZE20 po metodah ANN in GEP z eksperimentalno verifikacijo SI 109
- Osebnosti** SI 110



# Glušnik z adaptivnimi akustičnimi lastnostmi

Peter Šteblaj\* – Mirko Čudina – Primož Lipar – Jurij Prezelj

Univerza v Ljubljani, Fakulteta za strojništvo, Slovenija

V članku so predstavljeni rezultati raziskav, ki se nanašajo na zmanjševanje hrupa izpušnih sistemov motorjev z notranjim zgorevanjem in prezračevalnih sistemov. Raziskave so rezultat reševanja realnega problema pojava akustičnih resonanc v izpušnih sistemih. Akustične resonance se najpogosteje duši z vgradnjo konvencionalnih reaktivnih glušnikov, ki delujejo dobro pri danih obratovalnih razmerah in pri izbrani resonančni frekvenci, vendar ko se obratovalni pogoji spremenijo se spremeni tudi resonančna frekvenca in delovanje reaktivnega glušnika ni več učinkovito. Praksa uglaševanja konvencionalnih reaktivnih glušnikov na resonančno frekvenco se je doslej izvajala s krmiljenjem posameznega parametra glušnika, npr. volumna, dolžine ali togosti aktivnega elementa. Vse dosedanje rešitve adaptivnih reaktivnih glušnikov so prostorsko potratne, elektromehansko zahtevne in so povezane s povečanjem mase glušnika. Da bi odpravili vse te pomanjkljivosti smo razvili nov sistem z več različnih reaktivnih glušnikov z znanimi karakteristikami (Helmholtzov resonator, ekspanzijska komora in resonator četrtine valovne dolžine), ki se aktivirajo s pomočjo aktivno krmiljenih ventilov. Nov način aktivnega krmiljenja temelji na uporabi večjega števila ventilov, ki so krmiljeni na osnovi vsakokratnega spektra hrupa in algoritmov aktivnega dušenja hrupa. Ventili, z različnimi kombinacijami odpiranja in zapiranja, omogočajo vključevanje v funkcijo najprimernejšega posameznega ali skupine reaktivnih glušnikov in njihovo adaptivno prilagajanje tudi resonančnim oz. poudarjenim diskretnim frekvencam v danih obratovalnih razmerah sistema v katerega so vgrajeni.

Princip delovanja predlaganega sistema smo preverili z analitičnimi izračuni, numeričnimi simulacijami in eksperimentom. S primerjavo numeričnih simulacij in rezultatov meritev smo validirali rezultate numeričnih simulacij. Pri meritvah se je pojavil problem dinamičnega območja merilnih mikrofonov, saj reaktivni glušniki dosegajo prenosne izgube, ki so višje od 65 dB. Rezultati validacije omogočajo napovedovanje prenosnih izgub, ki so višje od dinamičnega območja uporabljenih mikrofonov. Z validacijo je prav tako potrjena hipoteza, da lahko z aktivnim krmiljenjem ventilov spreminjamo reaktivnim glušnikom ne samo lastnosti, temveč tudi fizikalno ozadje njihovega delovanja. Posebnost in dodatna primerjalna prednost nove zasnove glušnika je tudi ta, da lahko z ustreznim krmiljenjem spremenimo ekspanzijsko posodo v Helmholtzov resonator in obratno. In še, da vrat Helmholtzevega resonatorja lahko uporabimo kot resonator četrtine valovne dolžine.

V članku je predstavljena tudi simulacija časovnega odziva predstavljenega adaptivnega sistema. Analiza je pokazala, da je sistem dovolj hiter, da lahko sledi premikom resonančne frekvence v realnem času oz. v realnem izpušnem sistemu. Predlagana zasnova glušnika odpravi potrebo po uporabi dodatnih reaktivnih glušnikov za doseganje različnih obratovalnih razmer sistema, kot je to primer v konvencionalnih izpušnih sistemih. Tako z uporabo predlaganega sistema v primerjavi s konvencionalnimi glušniki dosežemo enake ali boljše učinke dušenja, vendar z zmanjšano velikostjo in maso glušnika.

**Ključne besede: reaktivni glušnik, adaptivni glušnik, zmanjševanje hrupa, izpušni sistem**

# Vpliv dinamičnih zračnikov na toplotno ugodje v avtomobilu

Om Prakash Singh<sup>1,\*</sup> – Rohit Raut<sup>1</sup> – Mrinmoy Biswas<sup>1</sup> – Ramji Singh<sup>2</sup>

<sup>1</sup>Indijski inštitut za tehnologijo Mandi, Tehniška šola, Indija

<sup>2</sup>Aryabhata Univerza, Indija

Ko je vozilo parkirano na soncu, skozi streho vstopa v kabino velik toplotni tok in vzpostavijo se veliki temperaturni gradienti. Dinamični zračniki hladijo kabino, ko je vključena klimatska naprava, proizvajalci vozil pa žal ne dajejo voznikom in sopotnikom nobenih smernic za uporabo dinamičnih zračnikov v avtomobilih. Predstavljena študija preučuje vpliv dinamičnih zračnikov na temperaturo zraka v kabini v začetnem obdobju po vklopu klimatske naprave.

Ko toplogredni plini, ujeti v kabini vozila, absorbirajo toplotno sevanje sonca in ga nato izsevajo v vse smeri, v avtomobilu pride do pojava tople grede in posledično zraste temperatura zraka v kabini. Pojav je najbolj izražen, ko je avtomobil z zaprtimi okni več ur parkiran na neposredni sončni svetlobi in se vzpostavi občutna razlika med temperaturo zraka okolice in temperaturo zraka v kabini. Da bi se zoperstavili tej težavi, je treba v vozilo vdlati sistem za vnaprejšnje ohlajanje notranjosti, npr. prezračevalni sistem na sončno energijo ali klimatsko napravo z daljinskim upravljanjem, ki ohladi avtomobilsko kabino še pred vstopom potnikov v vozilo. Slabost takšne rešitve je visoka nabavna cena, kupca pa bremenijo tudi visoki stroški vgradnje takšnega sistema. V vozilo je treba vgraditi tudi popolnoma nov dodaten sistem in ker so dandanes avtomobili vse bolj optimizirani, vgradnja nove tehnologije ohlajanja ne more biti učinkovita. Obenem se poveča tudi masa celotnega vozila. Zato je bil preučen alternativni mehanizem za izboljšanje učinkovitosti hlajenja vozila, ki ne zahteva večjih posegov v klimatsko napravo.

Opravljen je bil tristopenjska analiza po metodi računalniške dinamike tekočin (CFD). V prvi stopnji so bili eksperimentalno izmerjeni podatki o temperaturi na različnih mestih v vozilu in ob različnih urah. V drugi stopnji je bil na podlagi konstrukcijskih podatkov izdelan 3D CAD-model avtomobila. V tretji stopnji je bil razvit CFD-model avtomobila in validiran na podlagi eksperimentalnih podatkov. Opravljene so bile tudi simulacije za preučitev vpliva dinamičnih zračnikov.

Rezultati kažejo, da se lahko hitrejši učinek ohlajanja v začetnem obdobju doseže z zveznim spreminjanjem kota dinamičnih zračnikov med končnima legama, s katerim dosežemo enakomerno porazdelitev temperature zraka po kabini. Avtorji na podlagi rezultatov predlagajo nastavitve velikega pretoka za prve tri do štiri minute delovanja klimatske naprave s prej opisano dinamiko uravnavanja nastavitve zračnikov. Klimatska naprava lahko nato deluje naprej v običajnem režimu in na ta način se zmanjša raba energije vozila.

Članek preučuje metodo za hitrejšo ohlajanje avtomobila, ki je bil parkiran na soncu. Z eksperimentalnimi in računskimi metodami je bil preučen vpliv dinamičnih zračnikov na enakomerno porazdelitev temperature v kabini. Računalniški podatki so bili najprej validirani z eksperimentalnimi rezultati. Avtorji predlagajo uporabo ekscentričnih vrtljivih gredi za predelavo statičnih zračnikov v dinamične zračnike, ki hitreje ohladijo vozilo in zmanjšajo rabo energije.

**Ključne besede:** toplotno ugodje, dinamični zračniki, računalniška dinamika fluidov, klimatizacija in prezračevanje, temperatura zraka v kabini

# Brušenje volframovega karbida pri izdelavi topovskih svetrov

Livia Dana Beju – Paul Dan Brindasu – Silvia Vulc  
Univerza “Lucian Blaga”, Tehniška fakulteta, Romunija

Predmet raziskave je analiza procesa brušenja karbidne trdine DK460UF (91 % WC in 9% Co), iz katere se izdelujejo rezalna orodja z neprekinjenimi rezalnimi robovi. Cilj je opredelitev izdelovalnih pogojev, ki privedejo do kakovostne površine.

Procese brušenja volframovega karbida za rezalna orodja je treba optimizirati zato, ker njihove aktivne površine zahtevajo določene kakovostne lastnosti za enostavnejše odstranjevanje odrezkov in daljšo življenjsko dobo orodja. Največja dovoljena hrapavost aktivne površine je  $Rz = 0,3 \mu\text{m}$ . Za ugotovitev optimalnih parametrov za izdelavo dobre površine je bila najprej opravljena teoretična študija, v kateri so bili opredeljeni glavni dejavniki, ki vplivajo na kakovost površin, na podlagi te študije pa je bil nato zasnovan še eksperiment.

Obdelovane površine (aktivne površine rezalnih orodij) so majhne in različnih geometrij, proizvodne serije so majhne, kinematično modeliranje pa je zato težavnejše. Zato smo izbrali eksperimentalno analizo, ki upošteva obrabo brusilnega koluta in hrapavost površin karbidne trdine.

V ta namen smo izpeljali:

- eksperimentalno analizo obrabe orodja (diamantnega brusilnega koluta),
- eksperimentalno študijo hrapavosti, pridobljene pri različnih delovnih pogojih z diamantnimi brusilnimi koluti različne zrnivosti in obrabe.
  - Gre za 24-faktorski eksperiment z neodvisnimi parametri zrnivost brusilnega koluta, hitrost, podajanje in globina reza (velja za nov kolut).
  - V režimu za optimalno hrapavost je bilo izdelanih več vzorcev z brusilnimi koluti s širokim razponom obrabe. Rezultat je opredelitev vpliva obrabe brusilnih kolutov na hrapavost.

Iz eksperimentalne analize obrabe brusilnih kolutov sta izšli krivulji obrabe kolutov za dva tipa zrnivosti brusilnih kolutov (46  $\mu\text{m}$  (tip D46) in 54  $\mu\text{m}$  (tip D54)). Analiza krivulj obrabe je pokazala, da se brusilni koluti z večjo zrnivostjo obrabljajo hitreje.

Zmogljivost procesa brušenja je opredeljena z brusnim faktorjem G, ki mora biti čim večji. Običajna vrednost faktorja G pri obdelavi železnih materialov je 20:1. Analiza obrabe pri brušenju orodij malega premera iz karbida DK460UF omogoča izračunavanje brusnega faktorja G. Ugotovili smo majhne vrednosti faktorja G med 2:1 in 5:1. Vrednost brusnega faktorja G je odvisna od zrnivosti brusilnega koluta in njegove obrabe. Pri manjši zrnivosti koluta (D46) je bil ugotovljen večji brusni faktor G, obraba brusilnega koluta pa povzroči zmanjšanje brusnega faktorja G.

Rezultat 24-faktorskega eksperimenta je eksperimentalni matematični model. Gre za linearno polinomske funkcijo, ki opisuje hrapavost v odvisnosti od globine reza, podajanja, hitrosti rezanja in zrnivosti brusilnega koluta. Najboljša hrapavost je bila ugotovljena pri naslednjih parametrih:  $v = 55 \text{ m/s}$ ,  $f = 0,005 \text{ mm/vrt.}$ ,  $ap = 0,01 \text{ mm}$  in zrnivost 46  $\mu\text{m}$ . Vrednost površinske hrapavosti  $Rz$  v teh pogojih je bila 0,228  $\mu\text{m}$ .

Študija odvisnosti hrapavosti od radialne obrabe brusilnega koluta je pokazala, da je hrapavost  $Rz = 0,3 \mu\text{m}$  dosegljiva samo pri brusilnih kolutih z zrnivostjo, manjšo od 46  $\mu\text{m}$ . Največja dovoljena radialna obraba  $\Delta r$  pri brusilnem kolutu D46 je 30  $\mu\text{m}$ .

Raziskava je bila osredotočena na ostrenje posebne vrste rezalnih orodij – topovskih svetrov malega premera (od 2,025 do 2,5 mm). Obdelava se je izvajala v prisotnosti emulzije vode in 5 % olja PETROFER SUPERFIN pri tlaku 1 MPa. Za druge vrste orodij in rezalnih tekočin bodo potrebne dodatne raziskave.

Članek preučuje posebno kategorijo brušenja, ki do sedaj še ni bila analizirana v literaturi. Gre za brušenje zelo zahtevnega materiala – karbidne trdine DK460UF (91 % WC in 9 % Co). Obdelovane površine so zelo majhne in imajo veliko robov, kakovost obdelane površine pa mora biti zelo velika. Proizvodne serije so majhne in globina reza zavzema različne vrednosti. Aplikacija je pomembna zato, ker je kakovost delovnih in prostih površin rezalnega orodja nujna za natančnost obdelovanih površin in življenjsko dobo rezalnega orodja. Študija je eksperimentalne narave in članek ima praktično vrednost.

**Ključne besede: volframov karbid, brušenje, brusilni kolut, hrapavost, zrnivost, obraba**

# Simulacija hidravličnega sistema bagra z nelinearnimi matematičnimi modeli

Paolo Casoli\* – Nicola Pompini – Luca Riccò

Univerza v Parmi, Oddelek za industrijski inženiring, Italija

Najnovejše raziskovalne dejavnosti na področju mobilne hidravlike so usmerjene predvsem v optimizacijo sistemov, opredeljevanje novih konfiguracij sistemov in hibridizacijo sistemov. Vsi omenjeni pristopi so namenjeni varčevanju mobilne hidravlike z energijo za zmanjšanje porabe goriva in emisij onesnaževalcev. Za optimalno izkoriščanje novih sistemskih konfiguracij je treba razviti tudi optimalne strategije krmiljenja. Zato se povečuje zanimanje za razvoj novih sistemskih rešitev in njihovih strategij krmiljenja. Matematična orodja za opredelitev ustreznih krmilnih strategij so ključnega pomena za zadovoljitev zahtev po zanesljivejših in učinkovitejših sistemih. Pristop k matematičnemu modeliranju in metodologija, ki sta opisana v tem članku, obravnavata problem primernega dinamičnega modela sistema in kratkega računskega časa. Predstavljena metodologija je bila uporabljena za hidravlični bager. Po opisanem pristopu so bile opredeljene in modelirane glavne komponente podsistema tega gradbenega stroja.

Glavna črpalka s spremenljivo gibno prostornino in zaznavanjem obremenitve je bila modelirana samo ob upoštevanju dinamike nagibanja opletne plošče, ki ima najpočasnejšo dinamiko in najbolj vpliva na hidravlični sistem. Pri modeliranju aksialne batne črpalke s spremenljivo gibno prostornino je običajno treba upoštevati več fizikalnih pojavov za opredelitev sil na opletno ploščo, od sprememb tlaka v vsakem batu do interakcij med bati in opletno ploščo. Pristop k modeliranju, ki bi v celoti popisal omenjeni pojav, bi zahteval velike računske zmogljivosti in s tem dolg računski čas. Problem modeliranja dinamičnega vedenja opletne plošče brez upoštevanja sil, povezanih z bati, je bil razrešen s pomočjo izvirne eksperimentalne korelacije za izračun sile batov ter s karakterizacijo parametrov, ki vplivajo na dinamično vedenje opletne plošče. Smerni krmilni ventil je naslednji ključni element pri preučevanju konfiguracije in krmiljenja novega sistema. Modeliranje takšne komponente vključuje tudi dinamični model lokalnega tlačnega kompenzatorja. Za validacijo matematičnega modela podsistema je bil opravljen poseben eksperiment, ki je predstavljen v članku.

Naslednja pomembna značilnost hidravličnih sistemov je njihova togost zaradi velikega elastičnega modula pri stiskanju hidravlične tekočine. Togost zahteva zmanjšanje časovnega koraka pri reševanju diferencialnih enačb za porast tlaka v majhnih prostorninah. Zato so bile uporabljene tehnike združevanja volumskih območij in povečevanja prostornine za povečanje najmanjšega časovnega koraka, ki še zagotavlja točnost in zanesljivost rezultatov.

Predstavljena metodologija matematičnega modeliranja po eni strani omogoča točno modeliranje dinamičnega vedenja kompleksnega hidravličnega sistema s hitro simulacijo, po drugi strani pa zaradi uvedenih poenostavitev ni primerna za optimizacijo zasnove podsistema.

**Ključne besede:** modeliranje hidravličnega bagra, nelinearno modeliranje hidravličnega sistema, črpalka s spremenljivo gibno prostornino, zaznavanje obremenitve, delitev toka

# Potenčni model pretoka nenewtonske tekočine s strižno odvisnim upadanjem viskoznosti skozi kanal z oviro

Mohammadreza Saffarian<sup>1</sup> – Moona Mohammadi<sup>1,\*</sup> – Mohammadreza Mohammadi<sup>2</sup>

<sup>1</sup> Univerza Shahid Chamran, Fakulteta za strojništvo, Iran

<sup>2</sup> Iransko nacionalno plinsko podjetje, Bushehr Gas Company, Iran

Raziskovalci so se do zdaj manj posvečali nenewtonskim tekočinam, ki pa se v industriji in v okolju pojavljajo pogosteje kot newtonske tekočine. Tok newtonske tekočine ob oviri je lahko povsem drugačen od toka nenewtonske tekočine. Za newtonske tekočine je značilna konstantna viskoznost, na podlagi katere se tudi izračunava porazdelitev hitrosti, medtem ko je viskoznost pri nenewtonskih tekočinah spremenljiva in odvisna od raznih hitrostnih gradientov v pretočnem polju.

Obstajata dva glavna pristopa k preučevanju nenewtonskih tekočin. Prvi pristop obravnava študije primerov iz industrije, drugi pa vključuje temeljne raziskave, ki so lahko uporabne za različne industrijske aplikacije. V tej raziskavi je bil uporabljen drugi pristop in obravnava temeljni problem.

Članek obravnava tok nenewtonske tekočine s strižno odvisnim upadom viskoznosti v specifičnih geometrijskih pogojih. Privzet je laminaren tok skozi pravokoten kanal z eno oviro, ki se nahaja na sredini kanala in je visoka polovico širine kanala.

Medtem ko se pri newtonskih tekočinah uporabljajo Navier-Stokesove enačbe, se pri nenewtonskih tekočinah uporabljajo Cauchyjeve enačbe. Če pri numeričnem reševanju privzamemo konstantno viskoznost v vsaki mreži in variabilno viskoznost v celotnem polju, pa je mogoče tudi pri slednjih uporabiti Navier-Stokesove enačbe.

Rezultat te raziskave je numerična rešitev, pridobljena v programu MATLAB z algoritmom SIMPLEC in potenčnim modelom. Da bi pokazali njihovo neodvisnost, so bile izbrane tri različne mreže. Pri mrežah  $21 \times 83$ ,  $25 \times 100$  in  $31 \times 125$  je bil ugotovljen zelo majhen vpliv hitrosti. V izračunih so bile zato zaradi krajšega računskega časa in enake natančnosti uporabljene mreže  $25 \times 100$ .

Koda je bila validirana s primerjavo rezultatov kode z analitičnimi rezultati za specifičen pogoj. Numerične rešitve je mogoče validirati s primerjavo rezultatov z eksperimentalnimi rešitvami, analitičnimi rešitvami ali predhodno validiranimi numeričnimi rešitvami. V raziskavi je bila uporabljena druga metoda in rezultati numerične rešitve so bili primerjani z analitično rešitvijo za newtonsko tekočino. Koda je bila validirana na primeru pretoka newtonske tekočine skozi kanal brez ovire na sredini.

Rezultati so pokazali, da povečanje vrednosti  $n$  pri konstantnih lastnostih tekočine privede do povečanja viskoznosti. Hitrost v kanalu je obratno sorazmerna z viskoznostjo in pri minimalni viskoznosti bi bila največja zaradi majhnega upora tekočine proti gibanju. Zaradi nenadne spremembe preseka kanala ob oviri se močno poveča v vozliščih blizu plošče.

V članku je opisana spremenljivost hitrosti in viskoznosti ter njuna odvisnost od lastnosti tekočine v specifični geometriji kanala z eno oviro na sredini.

Rezultati te raziskave, ki opisujejo spremenljivost hitrosti in viskoznosti v kanalu, so lahko izjemno uporabni za prihodnje raziskave in realne aplikacije ne le zaradi pogoste uporabe tekočin s strižno odvisnim upadom viskoznosti v industrijskih aplikacijah, temveč tudi zaradi razširjenosti takih kanalov v različnih procesih in v raznih industrijah.

**Ključne besede:** nenewtonska tekočina, SIMPLEC, notranji tok, pretok s strižno odvisnim upadom viskoznosti, numerična rešitev, geometrija kanala

# Vpliv vsebnosti mikro- in nanopolnil na mehanske lastnosti epoksi kompozitov

Iskender Ozsoy<sup>1</sup> – Askin Demirkol,<sup>1,\*</sup> – Abdullah Mimaroglu<sup>1</sup> – Huseyin Unal<sup>2</sup> – Zafer Demir<sup>3</sup>

<sup>1,\*</sup> Univerza v Sakaryi, Tehniška fakulteta, Turčija

<sup>2</sup> Univerza v Sakaryi, Tehniška fakulteta, Turčija

<sup>3</sup> Univerza Anadolu, Visoka šola Porsuk, Turčija

Želene lastnosti polimernih matriksov se zagotavljajo z različnimi polnili. Uporabljajo se mineralna polnila, kmetijski izdelki in pucolan. Raziskovalci na tem področju preučujejo vpliv oblike delcev, vrste polnila, velikosti, deleža ter adhezije med matriksom in polnilom na mehanske lastnosti polimernih kompozitov. Ta študija preučuje vpliv vsebnosti mikro- in nanopolnil na mehanske lastnosti epoksi kompozitov. V ta namen so bili izvedeni natezni preizkus, tritočkovni upogibni preizkus in preizkusi trdote. Pridobljeni in ovrednoteni so bili podatki o natezni trdnosti, elastičnem modulu, raztežku pri pretrganju, upogibni trdnosti, upogibnem modulu in trdoti epoksi kompozitov.

Polimerni matriks v tej študiji je bila epoksi smola. Matriksu so bila dodana mikropolnila kot so aluminijev oksid ( $\text{Al}_2\text{O}_3$ ), titanov dioksid ( $\text{TiO}_2$ ) in leteči pepel, in sicer 10 % do 30 % po masi. Dodana so bila nanopolnila kot so aluminijev oksid ( $\text{Al}_2\text{O}_3$ ), titanov dioksid ( $\text{TiO}_2$ ) in nanogлина, in sicer z masnim deležem 2,5 % do 10 %.

Opravljene so bili standardni natezni preizkus, tritočkovni upogibni preizkus in preizkus trdote po standardih ASTM D638-10, ASTM D790-10 in ASTM D2583-07.

Rezultati kažejo, da se natezna trdnost kompozitov z mikropolnili zmanjšuje s povečevanjem deleža polnila. To je mogoče pojasniti tako, da povečan delež polnila povzroči šibko adhezijo med matriksom in polnilom ter posledično zmanjšanje trdnosti epoksi kompozita. Pri nanopolnilih je zmanjšanje trdnosti posledica nehomogene porazdelitve pri velikih deležih polnila, ki povzroči aglomeracijo in območja koncentracije napetosti. Zmanjšanje raztežka pri pretrganju za kompozite s polnilom je mogoče pojasniti z elastičnimi lastnostmi kompozita. Te so odvisne od polimernega matriksa, ki v prisotnosti polnil postane krhek. Zmanjšanje upogibne trdnosti kompozitov je mogoče pojasniti z aglomeracijo nanopolnil pri večjih deležih ter s šibko adhezijo med polnilom in matriksom pri visokih vsebnostih mikropolnila. Povečevanje upogibnega modula z naraščanjem vsebnosti polnila je posledica tega, da polnila povečajo togost polimernega kompozita.

Polnilo v večini primerov poveča trdoto kompozita. Pri letečem pepelu in nanoglini v visokem deležu je bil opažen manjši padec vrednosti trdote. To je mogoče pojasniti s šibko adhezijo med epoksi matriksom in polnilom.

Rezultati so končno pokazali, da se natezna trdnost, upogibna trdnost in raztezek pri pretrganju pri kompozitih zmanjšajo, medtem ko se elastični modul in upogibni modul povečata s povečevanjem deleža mikro- in nanopolnila. Epoksi kompoziti izkazujejo ob dodatku polnila krhko vedenje, pri visokih deležih nanopolnila pa se pojavlja problem aglomeracije polnila. Nadaljnje raziskave bodo lahko preučile in ovrednotile tribološke, električne, toplotnoizolacijske in toplotne lastnosti teh kompozitov.

**Gljučne besede: mikro- in nanopolnila, mehanske lastnosti, epoksi, kompozit**

# Napovedovanje dejanskih napetosti v magnezijevi zlitini ZE20 po metodah ANN in GEP z eksperimentalno verifikacijo

Sedat Bingöl<sup>1,\*</sup> – Wojciech Misiolek<sup>2</sup>

<sup>1</sup>Univerza Dicle, Oddelek za strojništvo, Turčija

<sup>2</sup>Univerza Lehigh, Inštitut za preoblikovanje kovin, ZDA

Večina magnezijevih izdelkov v avtomobilski industriji se izdeluje z visokotlačnim litjem (HPDC), med njimi pa so bloki in glave motorjev, ohišja menjalnikov in druge manjše komponente. Konstruktorji iščejo nove načine za gradnjo avtomobilov, ki bi manj obremenjevali okolje. Zmanjšanje mase avtomobilov je pomembna priložnost za zmanjšanje porabe goriva. Delež kovanih magnezijevih zlitin bi se moral še povečati zaradi visokega razmerja med trdnostjo in maso. Trenutni projekti raziskav in razvoja magnezijevih zlitin in njihove uporabe v avtomobilski industriji so osredotočeni predvsem na kovane magnezijeve zlitine.

Predstavljena študija preučuje preoblikovalnost magnezijeve zlitine ZE20, ki jo je razvilo podjetje General Motors. Študije so bile opravljene v dveh fazah: najprej so bili narejeni termomehanski preizkusi za pridobivanje krivulj napetosti pri preoblikovanju magnezijeve zlitine ZE20 pri različnih hitrostih deformacij in temperaturah, v drugi fazi pa so bili razviti modeli APP in GEP za napovedovanje dejanskih krivulj napetosti pri zlitini ZE20. Uspešnost razvitih modelov je bila ovrednotena s statističnimi merili ( $R^2$ , MSE, MAE). Prvi del študije je osredotočen na vpliv temperature in hitrosti deformacij na mehanske lastnosti magnezijeve zlitine ZE20. Nova magnezijeva zlitina ZE20 (2 utež. % Mg, 0,2 utež. % Zn, Ce) je bila podvržena deformacijam za ugotavljanje dejanskega vedenja pod obremenitvijo. Pri postavitvi modelov ANN in GEP za zlitino ZE20 so bili uporabljeni podatki o dejanskih napetostih v odvisnosti od temperature, dejanskih deformacijah in hitrosti deformacij. Za pridobivanje teh podatkov za to študijo so bili opravljeni enoosni tlačni preizkusi pri temperaturah 200 °C, 375 °C in 425 °C ter pri hitrostih deformacij 0,01 s<sup>-1</sup>, 5 s<sup>-1</sup> in 15 s<sup>-1</sup>. Eksperimenti za analizo preoblikovalnosti v vročem so bili opravljeni na stroju Gleeble 3500 s preizkušanci premera 8 mm in višine 12 mm. Pri razvoju modelov so bili upoštevani trije vhodni parametri: dva od njih - temperatura in hitrost deformacij - predstavljata pogoje tlačnega preizkusa, en - dejanski raztezek ( $\epsilon$ ) - pa predstavlja rezultat dejanske napetosti pri vsaki temperaturi ( $T$ ) in hitrosti deformacij ( $\dot{\epsilon}$ ).

Za ocenjevanje dejanskih napetosti v zlitini ZE20 pri tlačnih preizkusih je bila uporabljena struktura usmerjene nevronske mreže. Eksperimentalni podatki (za 657 vzorcev) so bili randomizirani in razdeljeni v dve kategoriji: podmnožice za učenje (80 %) in podmnožice za preizkušanje (20 %). Idealna prenosna funkcija ter število nevronov in skritih plasti sta bila ugotovljena po metodi poizkusov in napak. Kot kriteriji uspešnosti pri napovedovanju eksperimentalno določenih dejanskih napetosti v zlitini ZE20 za izbiro najboljše strukture omrežja so bila uporabljena merila  $R^2$ , RMSE in MAE. Po preizkusu več struktur ANN je bila določena optimalna struktura nevronske mreže z Levenberg-Marquardtovim algoritmom vzvratnega postopka učenja, prenosno funkcijo TanhAxon in šestimi nevroni v eni skriti plasti.

Vhodni parametri in vsi podatki, uporabljeni za razvite modele GEP, so bili enaki kot pri modelih ANN. Različna števila kromosomov, genov in velikosti glav vplivajo na zmogljivost modela GEP. Idealni model GEP je bil zato določen s spreminjanjem njihovega števila. Število kromosomov se je gibalo od 10 do 40, število genov od 2 do 7 in velikost glav od 5 do 9. Pridobljene so bile tudi enačbe za napovedovanje dejanskih napetosti za najboljši model GEP. Točnost razvitih modelov ANN in GEP pri napovedovanju rezultatov kompresijskih preizkusov je bila ocenjena s statističnimi merili. Modela ANN in GEP izkazujeta dobro ujemanje med napovedanimi in eksperimentalno določenimi dejanskimi napetostmi pri zlitini ZE20 (večji  $R^2$  ter manjša RMSE in MAE). Enačba, ki je bila v tej študiji izpeljana po modelu GEP, je preprosta in zato uporabna za dodatno napovedovanje dejanskih napetosti v zlitini ZE20.

**Ključne besede:** magnezij, ZE20, tlak, dejanske napetosti, GEP ANN, napovedovanje

## Doktorski disertaciji, znanstveno magistrsko delo

### DOKTORSKE DISERTACIJE

Na Fakulteti za strojništvo Univerze v Ljubljani sta obranila svojo doktorsko disertacijo:

- dne 4. septembra 2015 **Primož POREDOŠ** z naslovom: »Laserski triangulacijski sistemi za merjenje deformacij in pooperativnih stanj v ortopedski kirurgiji« (mentor: prof. dr. Janez Možina, somentor: prof. dr. Vane Antolič);

Delo obravnava razvoj dveh ločenih merilnih sistemov za analizo gibanja kolenskega sklepa in analize krivin hrbtenice. Za ta namen smo uporabili metodo laserske triangulacije, pri kateri je interesno območje osvetljeno z lasersko svetlobo. Prvi merilni sistem temelji na komercialno dostopni napravi Microsoft Kinect in ima ocenjeno natančnost 1,4 mm, medtem ko drugi merilni sistem temelji na laserskem 3D profilometru, ki ima natančnost 0,1 mm. Programska oprema za analizo gibanja kolenskega sklepa omogoča zajem oblike stegna in goleni ter detekcijo označevalcev pri periodičnemu gibu dviga in spusta goleni. Končni rezultat analize je določitev histereze gibanja kolenskega sklepa s primerjavo ovojnice dviga in spusta goleni. Programska oprema za analizo krivin hrbtenice v prvi fazi omogoča določitev referenčne in samodejne prostorske krivulje hrbtenice, ki temeljita na določitvi ročno označenega poteka hrbtenice in analizi ukrivljenosti 3D oblike hrbta. V drugi fazi pa omogoča analizo krivin hrbtenice v kranio-kavdalnem pogledu, kar dosežemo z vzporednim premikom in zasukom krivulje hrbtenice v prostoru, tako da začetna in končna točka hrbtenice sovpadata v koordinatnem izhodišču transverzalne ravnine. Rezultati kliničnih meritev v primeru analize gibanja kolenskega sklepa kažejo na okoli 60 % uspešnost razvitih algoritmov pri zaznavi kolen z osteoartrazo ali TEP kolenskega sklepa v primerjavi z zdravimi. Rezultati kliničnih meritev v primeru merjenja krivin hrbtenice v prvi fazi kažejo, da sta tipični odstopanja med referenčno in samodejno krivuljo hrbtenice 5,0 mm v frontalni in 1,0 mm v sagitalni ravnini, ker je precej manj od napake pri ročnem določanju referenčne krivulje (9,8 mm). V drugi fazi kliničnih meritev smo z razvito metodo dokazali statistično signifikantno razlikovanje med skoliotično in kontrolno skupino preiskovancev;

- dne 18. septembra 2015 **Jovan TRAJKOVSKI** z naslovom: »Odziv centralno in ekscentrično obremenjenih oklepkih pločevin »V« in »U« oblik pod vplivom eksplozijskega vala razstreliva« (mentor: prof. dr. Ivan Prebil, somentor: prof. dr. Franc Kosel);

Lahka oklepna vozila (LOV) so zelo pogosto izpostavljena eksplozivnemu delovanju min, čeprav niso snovana za takšne obremenitve. Dno LOV je v večini primerov narejeno iz le nekaj milimetrov debele oklepne pločevine in je zaradi tega v primeru eksplozijske obremenitve šibka točka vozila, kar je posledično lahko usodno za posadko. Zaradi tega je v doktorskem delu podrobneje raziskan vpliv geometrijske oblike pločevin na njihov mehanski odziv na eksplozijsko obremenitev razstreliva. Trije numerični modeli: empirični ConWep-model, MMALE-model in SPH-model so podrobneje raziskani s posebnim poudarkom na njihovi natančnosti in učinkovitosti. Najprimernejši (SPH) model je uporabljen za nadaljnje raziskave vpliva velikosti radija za U-pločevine in kota za V-pločevine za centralno in ekscentrično obremenitev z eksplozijskim valom razstreliva. Poleg tega je bila za namen numerične raziskave izvedena tudi karakterizacija mehanskih lastnosti oklepnega jekla PROTAC 500 in na podlagi eksperimentalnih podatkov so bili vrednoteni materialni parametri trdnostnega in poškodbenega Johnson-Cookevega modela. Za izbrano obliko pločevine je bila s pomočjo parametriziranega MKE-modela izvedena optimizacija geometrijskih lastnosti za določen primer obremenjevanja. Rezultati raziskave so bili uporabljeni na realnem primeru tako, da je bila izvedena primerjalna MKE-analiza za obstoječe konstrukcije LOV z ravnim dnom, VALUK 6×6, in njeno modificirano različico z 90-stopinjskim Vdnom. Rezultati so pokazali, da ima kot značilen vpliv na lokalni odziv vozila, kar je bistvenega pomena pri snovanju za posadko varnih LOV, ki izpolnjujejo predpisane standarde varnosti;

- dne 25. septembra 2015 **Klemen POVŠIČ** z naslovom: »Laserski triangulacijski sistem za merjenje premikov prsnega koša pri dihanju med telesno obremenitvijo« (mentor:izr. prof. dr. Matija Jezeršek, somentor: prof. dr. Janez Možina);

Doktorsko delo obravnava razvoj laserske tridimenzionalne (3D) merilne metode za sprotni nadzor in korekcijo motenj dihanja med telesno obremenitvijo. Merjenje temelji na laserski triangulaciji s ploskovnim vzorcem, ki sočasno osvetljuje celotno merjeno površino. Namensko razviti algoritmi omogočajo, da ločimo neželene premike in deformacije telesa od tistih deformacij, ki so neposredno povezane z dihanjem. V okviru tega smo zasnovali tudi preprosto in intuitivno metodo vizualizacije deformacij, ki služi prikazu dihalnih

aktivnosti na zaslonu. Za merjenje dihalnih deformacij smo uporabili dva merilna sistema. Prvi temelji na dvostranskem merjenju, pri čemer prsno-trebušno in hrbtno površino sočasno osvetljujemo z večlinijskim laserskim vzorcem. Drugi merilni sistem pa temelji na enostranski postavitvi, kjer z zaznavo prostorskega položaja petih referenčnih točk na prsno-trebušni površini poleg togih premikov kompenziramo tudi torzijske in upogibne deformacije telesa. Verifikacijo natančnosti izmerjenih volumnov smo izvedli s standardnimi sistemi za merjenje volumetričnih karakteristik. Odstopanje med referenčnimi volumni in volumni laserskih meritev znaša 12 % (referenčna brizga) oziroma 5 % (spirometer). Rezultati kažejo izboljšano natančnost merjenja v primerih, ko so med obremenitvijo prisotni tudi premiki telesa, na primer med vožnjo sobnega kolesa ali pri hoji po vadbenem traku. Napaka izmerjenih volumnov se pri togih premikih telesa zmanjša iz  $\pm 1,93 \text{ dm}^3$  na  $\pm 0,08 \text{ dm}^3$ , pri torzijskih deformacijah iz  $\pm 0,09 \text{ dm}^3$  na  $\pm 0,02 \text{ dm}^3$  ter pri upogibnih deformacijah iz  $\pm 0,16 \text{ dm}^3$  na  $\pm 0,11 \text{ dm}^3$ .

Vizualizacija deformacij zaradi dihanja tako kaže velik potencial v kliničnih primerih, kjer sta trening in učenje pravilnega dihanja pomembna dejavnika uspešne rehabilitacije. Klinični testi so pokazali, da so pacienti z razvito metodo v povprečju za 10 % izboljšali aktivacijo trebušnega predela med treningom na sobnem kolesu, pri tem pa niso imeli nikakršnih težav pri razumevanju vizualne povratne zanke na zaslonu;

• dne 28. septembra 2015 **Vanja PAHOR KOS** z naslovom: »Karakterizacija pospešenih vibracijskih testov v frekvenčnem prostoru« (mentor: prof. dr. Miha Boltežar, somentor: prof. dr. Marko Nagode);

Vibracijska testiranja komponent v industriji pogosto zahtevajo dolgotrajna preizkušanja. Z namenom skrajšanja teh časov se veliko pozornosti namenja pospešenim testiranjem. S ciljem pospešitve vibracijskih testiranj brez izgube zanesljivosti učinka testiranja je razvit pristop k obravnavi poškodbe v frekvenčni domeni, z upoštevanjem vzbujalnih parametrov testiranj. S poudarkom na sinusnem in naključnem vzbujanju strukture je vpliv obravnavan s stališča poškodbe strukture. Fenomen vibracijskega utrujanja je obravnavan s stališča frekvenčne domene skozi povezavo med časovno in frekvenčno domeno. Za izračun utrujanja materiala je uporabljeno Palmgren-Miner pravilo akumulacije poškodbe. Uporaba metode je prikazana na dveh eksperimentalnih primerih. Rezultati kažejo, da so tovrstne napovedi uporabne za primerjavo različnih vibracijskih vzbujanj, vendar niso tako natančne pri napovedovanju dejanskih časov do odpovedi;

• dne 29. septembra 2015 **Eneja OSTERMAN** z naslovom: »Sistem z latentnim hranilnikom toplote za ogrevanje in hlajenje prostorov« (mentor: prof. dr. Vincenc Butala, somentor: doc. dr. Uroš Stritih);

V doktorskem delu raziskujemo časovno neustaljen prenos toplote v latentnem hranilniku toplote (LHT), primernemu za aktivno naravno ogrevanje in hlajenje prostorov v stavbah. Zasnovo in izdelali smo prototipni latentni hranilnik toplote s ploščami napolnjenimi s fazno spremenljivo snovjo (FSS) in sicer je bil to parafin RT22HC, kot medij za prenos toplote/hladu pa je bil uporabljen zrak. Z eksperimentalnimi rezultati smo validirali numerični model, s katerim smo nato izvedli parametrično analizo polovičnih ciklov in določili vplivne parametre. Kot najbolj pomembni so se izkazali: volumski pretok, temperatura tališča in geometrijske značilnice, za katere smo s prirejenim numeričnim modelom izvedli analizo delovanja LHT na letnem nivoju. Ugotovili smo, da je za 0,6 m širok hranilnik najprimernejša temperatura tališča za zimo ter poletje enaka (t.j.  $20,5^\circ\text{C}$ ), najprimernejši volumski pretok zraka  $125 \text{ m}^3/\text{h}$  in najboljše geometrija z debelino plošče 12,5 mm in zračnim kanalom 25 mm (40 plošč). Na letnem nivoju lahko s takšno izbiro parametrov in zmanjšamo rabo energije v prostoru za 187 kWh;

• dne 30. septembra 2015 **Peter ŠTEBLAJ** z naslovom: »Aktivno krmiljenje reaktivnih glušnikov« (mentor: doc. dr. Jurij Prezelj, somentor: prof. dr. Mirko Čudina);

V disertaciji je predstavljen nov aktivni način krmiljenja reaktivnih glušnikov z uporabo krmiljenih ventilov. Nov način aktivnega krmiljenja temelji na uporabi večjega števila ventilov, ki so krmiljeni na osnovi algoritmov aktivnega dušenja hrupa. Predlagani sistem vsebuje tri osnovne tipe reaktivnih glušnikov, Helmholtzev resonator, ekspanzijsko komoro in resonator četrtine valovne dolžine. Z različnimi kombinacijami krmiljenih ventilov adaptivni glušnik sledi različnim obratovalnim razmeram delovnega sistema, v katerega je vgrajen. Predlagani sistem se lahko prilagodi in z uporabo aktivnega nadzora sledi trenutnim spremembam vhodnega signala oz. obratovalni točki delovnega sistema. Sistem je uporabljen pri motorjih z notranjim zgorevanjem in pri zmanjševanju hrupa v prezračevalnih ter dimniških sistemih.

Predlagana zasnova glušnika odpravi potrebo po uporabi dodatnih reaktivnih glušnikov za doseganje različnih obratovalnih točk delovnega sistema, kot je to primer v konvencionalnih izpušnih sistemih. Tako z uporabo predlaganega sistema v primerjavi s konvencionalnimi glušniki dosežemo enake ali boljše učinke dušenja, vendar z zmanjšano velikostjo glušnik.



# Information for Authors

All manuscripts must be in English. Pages should be numbered sequentially. The manuscript should be composed in accordance with the Article Template given above. The maximum length of contributions is 10 pages. Longer contributions will only be accepted if authors provide justification in a cover letter. For full instructions see the Information for Authors section on the journal's website: <http://en.sv-jme.eu>.

## SUBMISSION:

Submission to SV-JME is made with the implicit understanding that neither the manuscript nor the essence of its content has been published previously either in whole or in part and that it is not being considered for publication elsewhere. All the listed authors should have agreed on the content and the corresponding (submitting) author is responsible for having ensured that this agreement has been reached. The acceptance of an article is based entirely on its scientific merit, as judged by peer review. Scientific articles comprising simulations only will not be accepted for publication; simulations must be accompanied by experimental results carried out to confirm or deny the accuracy of the simulation. Every manuscript submitted to the SV-JME undergoes a peer-review process.

The authors are kindly invited to submit the paper through our web site: <http://ojs.sv-jme.eu>. The Author is able to track the submission through the editorial process - as well as participate in the copyediting and proofreading of submissions accepted for publication - by logging in, and using the username and password provided.

## SUBMISSION CONTENT:

The typical submission material consists of:

- A **manuscript** (A PDF file, with title, all authors with affiliations, abstract, keywords, highlights, inserted figures and tables and references),
  - Supplementary files:
    - a **manuscript** in a WORD file format
    - a **cover letter** (please see instructions for composing the cover letter)
    - a ZIP file containing **figures** in high resolution in one of the graphical formats (please see instructions for preparing the figure files)
    - possible **appendices** (optional), cover materials, video materials, etc.
- Incomplete or improperly prepared submissions will be rejected with explanatory comments provided. In this case we will kindly ask the authors to carefully read the Information for Authors and to resubmit their manuscripts taking into consideration our comments.

## COVER LETTER INSTRUCTIONS:

Please add a **cover letter** stating the following information about the submitted paper:

1. Paper **title**, list of **authors** and their **affiliations**.
2. **Type of paper**: original scientific paper (1.01), review scientific paper (1.02) or short scientific paper (1.03).
3. A **declaration** that neither the manuscript nor the essence of its content has been published in whole or in part previously and that it is not being considered for publication elsewhere.
4. State the **value of the paper** or its practical, theoretical and scientific implications. What is new in the paper with respect to the state-of-the-art in the published papers? Do not repeat the content of your abstract for this purpose.
5. We kindly ask you to suggest at least two **reviewers** for your paper and give us their names, their full affiliation and contact information, and their scientific research interest. The suggested reviewers should have at least two relevant references (with an impact factor) to the scientific field concerned; they should not be from the same country as the authors and should have no close connection with the authors.

## FORMAT OF THE MANUSCRIPT:

The manuscript should be composed in accordance with the Article Template. The manuscript should be written in the following format:

- A **Title** that adequately describes the content of the manuscript.
- A list of **Authors** and their **affiliations**.
- An **Abstract** that should not exceed 250 words. The Abstract should state the principal objectives and the scope of the investigation, as well as the methodology employed. It should summarize the results and state the principal conclusions.
- 4 to 6 significant **key words** should follow the abstract to aid indexing.
- 4 to 6 **highlights**; a short collection of bullet points that convey the core findings and provide readers with a quick textual overview of the article. These four to six bullet points should describe the essence of the research (e.g. results or conclusions) and highlight what is distinctive about it.
- An **Introduction** that should provide a review of recent literature and sufficient background information to allow the results of the article to be understood and evaluated.
- A **Methods** section detailing the theoretical or experimental methods used.
- An **Experimental section** that should provide details of the experimental set-up and the methods used to obtain the results.
- A **Results** section that should clearly and concisely present the data, using figures and tables where appropriate.
- A **Discussion** section that should describe the relationships and generalizations shown by the results and discuss the significance of the results, making comparisons with previously published work. (It may be appropriate to combine the Results and Discussion sections into a single section to improve clarity.)
- A **Conclusions** section that should present one or more conclusions drawn from the results and subsequent discussion and should not duplicate the Abstract.
- **Acknowledgement** (optional) of collaboration or preparation assistance may be included. Please note the source of funding for the research.
- **Nomenclature** (optional). Papers with many symbols should have a nomenclature that defines all symbols with units, inserted above the references. If one is used, it must contain all the symbols used in the manuscript and the definitions should not be repeated in the text. In all cases, identify the symbols used if they are not widely recognized in the profession. Define acronyms in the text, not in the nomenclature.
- **References** must be cited consecutively in the text using square brackets [1] and collected together in a reference list at the end of the manuscript.
- **Appendix(-ices)** if any.

## SPECIAL NOTES

**Units:** The SI system of units for nomenclature, symbols and abbreviations should be followed closely. Symbols for physical quantities in the text should be written in italics (e.g.  $v$ ,  $T$ ,  $n$ , etc.). Symbols for units that consist of letters should be in plain text (e.g. ms<sup>-1</sup>, K, min, mm, etc.). Please also see: <http://physics.nist.gov/cuu/pdf/sp811.pdf>.

**Abbreviations** should be spelt out in full on first appearance followed by the abbreviation in parentheses, e.g. variable time geometry (VTG). The meaning of symbols and units belonging to symbols should be explained in each case or cited in a **nomenclature** section at the end of the manuscript before the References.

**Figures** (figures, graphs, illustrations digital images, photographs) must be cited in consecutive numerical order in the text and referred to in both the text and the captions as Fig. 1, Fig. 2, etc. Figures should be prepared without borders and on white grounding and should be sent separately in their original formats. If a figure is composed of several parts, please mark each part with a), b), c), etc. and provide an explanation for each part in Figure caption. The caption should be self-explanatory. Letters and numbers should be readable (Arial or Times New Roman, min 6 pt with equal sizes and fonts in all figures). Graphics (submitted as supplementary files) may be exported in resolution good enough for printing (min. 300 dpi) in any common format, e.g. TIFF, BMP or JPG, PDF and should be named Fig1.jpg, Fig2.tif, etc. However, graphs and line drawings should be prepared as vector images, e.g. CDR, AI. Multi-curve graphs should have individual curves marked with a symbol or otherwise provide distinguishing differences using, for example, different thicknesses or dashing.

**Tables** should carry separate titles and must be numbered in consecutive numerical order in the text and referred to in both the text and the captions as Table 1, Table 2, etc. In addition to the physical quantities, such as  $t$  (in italics), the units [s] (normal text) should be added in square brackets. Tables should not duplicate data found elsewhere in the manuscript. Tables should be prepared using a table editor and not inserted as a graphic.

## REFERENCES:

A reference list must be included using the following information as a guide. Only cited text references are to be included. Each reference is to be referred to in the text by a number enclosed in a square bracket (i.e. [3] or [2] to [4] for more references; do not combine more than 3 references, explain each). No reference to the author is necessary.

References must be numbered and ordered according to where they are first mentioned in the paper, not alphabetically. All references must be complete and accurate. Please add DOI code when available. Examples follow.

## Journal Papers:

Surname 1, Initials, Surname 2, Initials (year). Title. Journal, volume, number, pages, DOI code.

- [1] Hackenschmidt, R., Alber-Laukant, B., Rieg, F. (2010). Simulating nonlinear materials under centrifugal forces by using intelligent cross-linked simulations. *Strojniški vestnik - Journal of Mechanical Engineering*, vol. 57, no. 7-8, p. 531-538, DOI:10.5545/sv-jme.2011.013.

Journal titles should not be abbreviated. Note that journal title is set in italics.

## Books:

Surname 1, Initials, Surname 2, Initials (year). Title. Publisher, place of publication.

- [2] Groover, M.P. (2007). *Fundamentals of Modern Manufacturing*. John Wiley & Sons, Hoboken.

Note that the title of the book is italicized.

## Chapters in Books:

Surname 1, Initials, Surname 2, Initials (year). Chapter title. Editor(s) of book, book title. Publisher, place of publication, pages.

- [3] Carbone, G., Ceccarelli, M. (2005). Legged robotic systems. Kordić, V., Lazinica, A., Merdan, M. (Eds.), *Cutting Edge Robotics*. Pro literatur Verlag, Mammendorf, p. 553-576.

## Proceedings Papers:

Surname 1, Initials, Surname 2, Initials (year). Paper title. Proceedings title, pages.

- [4] Štefanič, N., Martinčević-Mikić, S., Tošanović, N. (2009). Applied lean system in process industry. *MOTSP Conference Proceedings*, p. 422-427.

## Standards:

Standard-Code (year). Title. Organisation. Place.

- [5] ISO/DIS 16000-6.2:2002. *Indoor Air – Part 6: Determination of Volatile Organic Compounds in Indoor and Chamber Air by Active Sampling on TENAX TA Sorbent, Thermal Desorption and Gas Chromatography using MSD/FID*. International Organization for Standardization. Geneva.

## WWW pages:

Surname, Initials or Company name. Title, from <http://address>, date of access.

- [6] Rockwell Automation. Arena, from <http://www.arenasimulation.com>, accessed on 2009-09-07.

## EXTENDED ABSTRACT:

When the paper is accepted for publishing, the authors will be requested to send an **extended abstract** (approx. one A4 page or 3500 to 4000 characters). The instruction for composing the extended abstract are published on-line: <http://www.sv-jme.eu/information-for-authors/>.

## COPYRIGHT:

Authors submitting a manuscript do so on the understanding that the work has not been published before, is not being considered for publication elsewhere and has been read and approved by all authors. The submission of the manuscript by the authors means that the authors automatically agree to transfer copyright to SV-JME when the manuscript is accepted for publication. All accepted manuscripts must be accompanied by a Copyright Transfer Agreement, which should be sent to the editor. The work should be original work by the authors and not be published elsewhere in any language without the written consent of the publisher. The proof will be sent to the author showing the final layout of the article. Proof correction must be minimal and executed quickly. Thus it is essential that manuscripts are accurate when submitted. Authors can track the status of their accepted articles on <http://en.sv-jme.eu>.

## PUBLICATION FEE:

Authors will be asked to pay a publication fee for each article prior to the article appearing in the journal. However, this fee only needs to be paid after the article has been accepted for publishing. The fee is 240.00 EUR (for articles with maximum of 6 pages), 300.00 EUR (for articles with maximum of 10 pages), plus 30.00 EUR for each additional page. The additional cost for a color page is 90.00 EUR. These fees do not include tax.

Strojniški vestnik - Journal of Mechanical Engineering  
Aškerčeva 6, 1000 Ljubljana, Slovenia,  
e-mail: [info@sv-jme.eu](mailto:info@sv-jme.eu)



<http://www.sv-jme.eu>

# Contents

## Papers

- 553 Peter Šteblaj, Mirko Čudina, Primož Lipar, Jurij Prezelj:  
**A Muffler with Adaptive Acoustic Properties**
- 561 Om Prakash Singh, Rohit Raut, Mrinmoy Biswas, Ramji Singh:  
**Effect of Dynamic Vents on the Thermal Comfort of a Passenger Car**
- 571 Livia Dana Beju, Paul Dan Brindasu, Silvia Vulc:  
**Grinding Tungsten Carbide Used for Manufacturing Gun Drills**
- 583 Paolo Casoli, Nicola Pompini, Luca Riccò:  
**Simulation of an Excavator Hydraulic System Using Nonlinear Mathematical Models**
- 594 Mohammadreza Saffarian, Moona Mohammadi, Mohammadreza Mohammadi:  
**Non-Newtonian Shear-Thinning Fluid Passing Through a Duct with an Obstacle, Using a Power Law Model**
- 601 Iskender Ozsoy, Askin Demirkol, Abdullah Mimaroglu, Huseyin Unal, Zafer Demir:  
**The Influence of Micro- and Nano-Filler Content on the Mechanical Properties of Epoxy Composites**
- 610 Sedat Bingöl, Wojciech Misiólek:  
**Prediction of the True Stress of ZE20 Magnesium Alloy at Different Temperatures and Strain Rates**